

https://dspace.org/

Diamond thin films:synthesis,caharacterisation and application in quantum information processing

Mazhandu, Farai

2019
https://hdl.handle.net/10539/28757

Downloaded from a DSpace repository. https://dspace.org/



DIAMOND THIN FILMS: SYNTHESIS, CHARACTERISATION AND APPLICATION IN QUANTUM INFORMATION PROCESSING

Farai Mazhandu

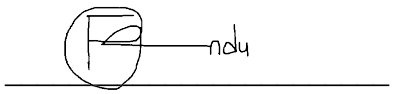
A dissertation submitted to the Faculty of Science, University of the Witwatersrand, Johannesburg, in fulfilment of the requirements for the degree of Master of Science.

Supervisor: Prof S. Bhattacharyya

Johannesburg, May, 2019

Declaration

I declare that this thesis is my own, unaided work. It is being submitted for the Degree of Master of Science in the University of the Witwatersrand, Johannesburg. It has not been submitted elsewhere before towards qualification for any degree or examination in any other University.



(Signature of candidate)

29th Day of May 2019

Abstract

A new era of quantum based technologies is currently unfolding and the most challenging amongst these is the quantum computer. A scalable and universal quantum computer stands on fast, reproducible and controllable high-coherence quantum bits (qubits). Quantum physics aspects such as superposition and entanglement are harnessed to provide the much needed improvement in capabilities to do information processing and simulation. Our work focuses on quantum technology based on quantum matter in diamond and the applications of quantum computers in the simulation of condensed matter physics phenomena.

Superconducting qubits and spin qubits have different merits which can be combined to build a hybrid quantum processor. A four junction flux qubit is proposed for computation because of its fast and coherent control. Nitrogen doping of diamond gives rise to nitrogen-vacancy centers (NV), an aspect which is manipulate in this work as a quantum bus and register.

The IBM Q cloud quantum computer is used to simulate effective coupling in a hybrid quantum system consisting of two spin qubits and a superconducting flux qubit. The NV^- center in a diamond crystal is effectively coupled to a flux qubit through an external magnetic flux. This work shows that the coupling strengths between a flux qubit, electron spin, and nuclear spin evolve from weak to strong. Coupling between spin and superconducting flux qubit is a subject of ongoing research while direct coupling is the preferred mechanism. Effective coupling is achieved through tuning the excitation frequencies of the individual spins via external magnetic fields.

A qubit is as good as the material it is built upon. Crucial to the successful operation of superconducting qubits is also the aspect of tunability and here we investigate quantum phase transitions in heavily boron doped diamond (HBDD) thin films using a cryogenic high field measurement system (CFMS).

Our results confirm tunable behavior in HBDD thin films as shown by switching from superconducting to insulating regime below the critical temperatures. We were also able to show digital quantum implementation of entanglement, decoherence, and fidelity which are critical properties when it comes to building a scalable universal quantum computer. This work clearly demonstrates the importance of a quantum simulator to researchers. We are able to observe and study profound physical phenomena as well as test ideas towards development of a hybrid quantum computer based on boron doped nanodiamond.

Acknowledgements

I am very grateful to my supervisor and examiner, Prof. Somnath Bhattacharyya. He always had time to answer my questions and also helped a lot in the lab to get familiar with all the instruments. I also want to extend my gratitude to my laboratory colleagues Dr. Siphepile Ncube, Dr. Chris Coleman, Phumzile Madonsela, Sav Mosse and Prof. Yorick Hardy with whom we had enlightening conversations on synthesis, characterization and quantum information processing.

This work would have been impossible without the availability of the quantum processor from IBM through the cloud. For that I am indebted to the IBM team and the IBM Quantum Experience project. However, the discussions and opinions developed in this thesis are entirely mine and do not reflect the opinions of IBM or the IBM QE team.

Lastly, my profound gratitude goes to my wonderful family. Their patience and support is forever cherished.

Contents

Declaration i

Abstract iii

Acknowledgements v

Contents vi

Chapter 1 1

Introduction 1

1.1 General Introduction 2

1.2 Research background 3

1.3 Problem statement 4

1.4 Research aims 5

1.5 Outline of the dissertation 6

Superconductivity in heavily boron doped diamond (HBDD) thin films 7

Chapter 2 7

2.1 Introduction 7

2.2 Electronic transport in superconductors 8

2.3 History and issues of 2D superconductors 10

2.4 Nature of the transition in BDD thin films 11

2.5 Mechanisms of superconductivity in thin films 13

Chapter 3 28

Experimental Methods 28

3.1 BDD Sample properties 28

3.2 Instruments and Measurement procedures 30

Chapter 4 41

Results and Analysis 41

4.1 Temperature dependent resistance and the Superconductor to Insulator transition: 41

4.2 Magnetoresistance 45

4.3 DC *I* - *V* measurements 48

Analysis 56

Quantum Information Processing 58

Chapter 5 58

Literature Review 58

5.1 Quantum Information Theory 58

5.2 Quantum Information Processing 72

5.3 Superconducting Qubits 78

5.4 The Flux qubit 89
5.5 NV^- center in Diamond 93
5.5 Hybrid Quantum System 106
Chapter 6 110
Experimental Methods 110
6.1 Quantum Simulation 110
6.2 IBM Quantum Experience (IBM Q) 111
6.3 Fundamental gate operations 118
6.4 Hybrid qubits implementation on IBMQX4 120
6.5 Mapping physical system on physical chip 121
Chapter 7 123
Results and Analysis 123
7.1 Simulation set-up 123
7.2 Entanglement 127
7.3 Decoherence 129
7.4 Gate fidelity 132
Analysis 134
Chapter 8 136
Conclusions 136
References 138

List of Figures

Figure 2.1: The first experiment demonstrating the phenomenon of superconductivity 9
Figure 2.2: At the boundary between a normal metal and a superconductor 10
Figure 2.3: Experimental findings of transport properties due to boron concentration 11
Figure 2.4: Generic description of quantum phase transition phase diagram 13
Figure 2.5: Modelling disorder driven effects using the Josephson junction array 15
Figure 2.6: The Josephson coupled weak links 16
Figure 2.7: Phase diagram for the superinsulator-superconductor transition in 2D 17
Figure 2.8: Charge distribution for a charge anti-charge pair in a JJ-array 18
Figure 2.9: Disorder driven reduction in Tc in amorphous Mo79Ge21 films 23
Figure 2.10: The re-entrant bosonic anomaly reported by Zhang et al 24
Figure 2.11: 2D dirty superconductor as a function of T and B 26
Figure 3.1: SEM images of the surface of one of the boron doped samples 29
Figure 3.2: Cryogenic High Field Measurement System 31
Figure 3.3: Parasitic 3He Insert Probe 33
Figure 3.4: Resistivity probe sample platform overview 35
Figure 3.5: Electrical contact configurations for Van der Pauw measurements 37
Figure 3.6: The SEM used for the characterization of BDD in the NSTPL at Wits 39
Figure 3.7: An X-ray diagram of a Scanning electron microscope (SEM) 40
Figure 4.1: The SIT in thin films of the superconductor TiN 42
Figure 4.2: The boron doped diamond bosonic peak 42
Figure 4.3: B4 resistance-temperature graph at different fields 43
Figure 4.4: T2 dependence for a Kondo effect 44
Figure 4.5: The magnetoresistance of the boron doped diamond 46
Figure 4.6: The activation energy of flux/vortex states for B4 48
Figure 4.7: An illustration of Andreev reflection 49
Figure 4.8: A comparison of differential parameters for HBDD vs TiN 52
Figure 4.9: IV characteristics for HBDD 53
Figure 4.10: High field characterisation of HBDD 53
Figure 4.11: Super linear IV characteristics as an indication of a BKT effect 54

Figure 5.1: Classical bit vs quantum bit ‘qubit’ 63
Figure 5.2: Classical bit space and elements in computation space 64
Figure 5.3: Bloch sphere representation of the qubit state control vectors 65
Figure 5.4: Common quantum gates names, symbols and matrices 68
Figure 5.5: Classification of computational problems 69
Figure 5.6: A comparison of resistance and temperature for superconductors and normal metals 79
Figure 5.7: Illustration of a Josephson junction 81
Figure 5.8: A demonstration of how the Josephson junction brings about anharmonicity 85
Figure 5.9: A SQUID and a superconductor-insulator-superconductor (SIS) Josephson junction 87
Figure 5.10: The basic Cooper pair box 88
Figure 5.11: Optical micrograph and the circuit scheme of the aluminum flux-qubit 90
Figure 5.12: Typical flux qubit parameters at a glance 91
Figure 5.13: Nitrogen-vacancy (NV) defect in diamond lattice 96
Figure 5.14: The molecular orbits for the NV centre showing ground and excited states 99
Figure 5.15: Zeeman splitting of ground state 101
Figure 5.16: Spin state fluorescence represented on a Bloch sphere 103
Figure 5.17: Rabi oscillation for a single NV centre 104
Figure 5.18: Energy relaxation and dephasing as decoherence sources 105
Figure 5.19: The different mechanism of coupling in hybrid quantum systems 108
Figure 6.1: A look inside the 50-qubit quantum computer at IBM 112
Figure 6.2: Qubit architecture 113
Figure 6.3: An inside look into the IBM Quantum Computer 114
Figure 6.4: Process flow diagram for a quantum algorithm through the IBM Q 116
Figure 6.5: A quantum algorithm implementation 117
Figure 6.6: The gates that rotate the vector around the z-axis, namely Z, S, and T-gate 118
Figure 6.7: Gate operation of the CNOT-gate 119
Figure 6.8: Typical 3 qubit gate sequence on an IBM composer 119
Figure 6.9: Schematic view of IBMqx4 chip 121
Figure 6.10: Entanglement with bit flip (SWAP) 122

Figure 7.1: Gap tunable superconducting flux qubit and its energy levels 124
Figure 7.2: NV center and flux qubit model 124
Figure 7.3: Unitary gates for 3 qubit system 125
Figure 7.4: Entanglement analysis 128
Figure 7.5: Three-qubit entangled system relaxation profile 130
Figure 7.6: Entangled electron spin decoherence 130
Figure 7.7: State coherence of the flux qubit 131
Figure 7.8: Ground state gate fidelity of central spin 132
Figure 7.9: Process fidelities for different schemes on applying dynamic decoupling 133

Abbreviations and Symbols

2D	two dimensional
3D	three dimensional
ABS	Andreev Bound State
AFM	Atomic Force Microscope
BCS	Bardeen-Cooper-Schrieffer
BKT	Berezinski-Kosterlitz-Thouless
DOS	Density of States
CVD	Chemical vapour deposition
CFMS	Cryogenic high field measuring system
FWHM	Full Width at Half Maximum
GB	Grain boundaries
HBDD	Heavily boron doped diamond
JJ	Josephson's Junction
MCD	Microcrystalline diamond
MIT	Metal-Insulator Transition
MR	Magnetoresistance
MWCVD	Microwave chemical vapour deposition
MW	Microwave
NV-centre	Nitrogen Vacancy-centre
QIS	Quantum information science
QIT	Quantum information theory
QPT	Quantum Phase Transition
R	Resistance
RB	Randomized benchmarking
SEM	Scanning Electron microscope
STM	Scanning Tunneling Microscopy
SQUID	Superconducting Quantum Interference Device
TEM	Transmission Electron microscope
WL	Weak localization

H	Planks constant
G	Conductance.
$\hbar$	Reduced Planks' constant.
T	Temperature.
e	Elementary electron charge.
B	Magnetic field.
k_B	Boltzmann constant.
σ	Conductivity
ρ	Resistivity
Δ	Superconducting gap
T_C or T_M	Critical temperature (mean field critical temperature)
μ_0	Permeability of vacuum
μ_B	Bohr magneton
λ	London penetration depth or AL dimensional critical exponent
E_C	Charging energy of individual grain
E_J	Josephson coupling energy between grains
Γ	Tunneling energy
I	Current
V	Voltage
I_C	Critical current
dI/dV	Differential conductance
dV/dI	Differential resistance

Chapter 1

Introduction

Quantum computers are a radically different kind of computer based on the laws of quantum mechanics. They have the potential to solve problems that scale up very fast and thus are intractable to classical computers. It is now possible to access real quantum computers through the cloud to conduct research and explore new problems. Today's quantum computers include thousands of parts that work together to harness qubits to perform quantum computations. Qubits themselves are incredibly powerful, yet delicate. They quickly lose their special quantum properties, typically within 100 microseconds (for state-of-the-art superconducting qubits), due in part to electromagnetic environment, vibrations, and temperature fluctuations. To make quantum computers more reliable and stable there is need to harmoniously combine different technologies that complement each other.

Diamond offers great promise as a quantum material in two fundamental ways i.e. nitrogen vacancy (NV) centers and heavily boron doped diamond (HBDD) thin films **[1-6]**. Heavily boron doped diamond (HBDD) thin films show superconductivity properties with tuneable behaviour important in fast information processing whereas nitrogen-doped diamond gives rise to nitrogen-vacancy centres (NV) which can function as spin qubits or storage in quantum information processing **[4]**.

Here we use the IBM quantum computer as the universal quantum simulator and simulate entanglement between a superconducting flux qubit and NV-center in diamond. We use the IBMqx4 5-qubit quantum processor from IBM that is available on the cloud. We investigate hybrid flux qubit-nitrogen-vacancy (NV) entanglement in the system consisting of a flux qubit and an NV-center (NVC). The influence of the initial entanglement degree of the flux qubit, the coupling strength between the flux qubit and the electron spin, the coupling strength between the flux qubit and the nitrogen nucleus and the tripartite entanglement is discussed. The maximally tripartite entangled state can be obtained under certain conditions.

In addition, it is shown that the time of disentanglement of the hybrid quantum system can be controlled by adjusting the coupling strength between the flux qubit and the electron spin and between the flux qubit and the nitrogen nucleus.

Further, we show that quantum phase transitions that occur in HBDD thin films are due to disorder and high field effects. We thus prove that it is possible to manipulate the phase transitions for quantum information processing hardware fabrication.

1.1 General Introduction

Superconducting flux qubits are attractive candidates for quantum information processing because of their flexibility and rapid single- and two-qubit gates, but compared to microscopic systems they suffer from short coherence times **[1, 2]**. Whilst the typical flux qubit is composed of a superconducting loop interrupted by three Josephson junctions, the four-junction circuit with two identical smaller junctions can be used as a better qubit than the three-junction circuit as it more robust. It is natural to suggest the combination of a spin and superconducting qubit in a hybrid quantum device given their complementary merits. The spin qubit with a long coherence time acts as a quantum memory whilst the superconducting flux qubit becomes a small-scale quantum processor.

In this work we focus on the negative Nitrogen Vacancy (NV^-) color centers in diamond as the microscopic entity. NV centers have coherence times that can reach seconds and can be actively reset in the spin ground state through photons. In our proposed hybrid quantum system, the interaction between the qubits evolves from weak to strong. The NV^- centre is taken as two qubits and directly coupled through magnetic flux to a four junction superconducting flux qubit. The goal of this work is to digitally simulate a hybrid quantum system on an IBM Q online quantum processor and investigate the viability of diamond as a quantum technology material through Cryogenic high field measurements.

1.2 Research background

Moore's Law held steady for decades, but it is beginning to falter as miniaturization of processor circuitry gets harder and harder. This challenge makes quantum computing more important as a possible way to continue progress in the industry. As transistors get smaller approaching the nanoscale range quantum mechanical effects start impacting the reliability of circuits. The good thing is that quantum excitations in condensed matter can be harnessed to address computation and storage demands at atomic level.

The birth of quantum theory, especially the discovery of quantum entanglement sparked the development of the field of quantum information processing to a level where it's now well-established. Notable success has not only been made on understanding the peculiarities of quantum theory, the deep connection between information processing capabilities and physical support at a theoretical level; it also brought technology to a new and broader physical framework, providing fundamentally new capabilities like cloud quantum processors. These quantum technologies offer researchers a testing ground for ideas in architecture, applications and quantum physics.

Quantum materials provide the environment where qubits, the elemental unit of quantum information processing, are defined and exist. Therefore, quantum materials are the basis of a quantum computer. To have a working quantum computer you need to couple together many qubits, while maintaining their long coherence time. These demands are often in conflict. The precision of the qubit materials is of major importance in order to solve these two challenging requirements. In this case precision refers to materials uniformity in- chemical composition, and electronic transport properties. Superconducting qubits offer great computational capabilities whilst spin-based qubits offer long coherence times that are critical for storage.

In the end, to make the phenomenally large number of qubits necessary to build a quantum computer, we would like to rely on the proven manufacturing techniques of the microelectronics industry like chemical vapour deposition (CVD). Diamond thin films can be produced in the laboratory and its boron doped thin films have interesting electron transport properties **[60-61]**.

Nitrogen doping of diamond also gives rise to nitrogen-vacancy centers (NV) which are useful as spin qubits or quantum registers for quantum information processing. Coupling between spin and superconducting flux qubit is a subject of ongoing research **[1, 28-30]** and as such is also an area of focus in this work. Further, ever since the first quantum algorithm was developed by Peter Shor **[3]** a couple of decades ago there has been a lot of progress in the field of quantum information processing and emerging online platforms now offer an opportunity to digitally experiment and gain valuable insights in quantum technology and condensed matter physics.

1.3 Problem statement

Developments in quantum computing and information processing are being hampered by very limited hardware: high error rates and challenges in achieving adequate coherence times required for computation. Today's quantum computers can solve a selective niche of problems but a general-purpose, widely-usable, practical quantum computer will require advances in error correction, coupling a large number of qubits and possess long coherence times. Different technologies have different advantages and only a hybrid system is able to harness the best of each platform.

The identification of NV^- centers has been a welcome development in the research of diamond based quantum systems. Possible applications are in various fields including hybrid quantum systems and quantum simulation **[4-6]**. NV^- centers are preferred in hybrid quantum systems due to their easy initialization and readout, fast and high-performance spin manipulation, long coherent times, and the ability to access and manipulate nearby nuclear spins. Additionally, NV^- centers can be readily coupled to superconducting flux qubits via a magnetic field. Several schemes have been developed to demonstrate multi-particle entanglement and NV^- center material samples of high enough quality can now be produced in the laboratory **[4]**.

The NV center is an intrinsically hybrid quantum system: its electron spin is always coupled to the nuclear spin of its own nitrogen atom. The long coherence time of the NV spin center combined with the convenience in sample fabrication and fast manipulation of superconducting qubits like the flux qubit establishes a promising future for a scalable quantum computer based

on diamond. Research on direct coupling between a flux qubit and NV centre is extensive but the digital demonstration of entanglement between superconducting and spin qubits is undeveloped. The availability of online quantum computing platforms has given new impetus to quantum simulation. The IBM Q cloud quantum processor now makes it possible to simulate intricate quantum physics phenomena like decoherence, entanglement and superposition.

Heavily boron doped thin films show unique quantum phase transitions that can be harnessed in quantum technology based on diamond. In order to move to device fabrication on diamond as a quantum material there is need to fully understand its electron transport characteristics. Further, diamond can also be considered for resonators that connect qubits with the control systems.

1.4 Research aims

The aim of this dissertation is to present experimental research that adds to the general body of knowledge on hybrid quantum systems based superconducting and spin qubits and to the process of realizing a scalable universal quantum computer. More specifically we will address the aspect of effective coupling between the NV center and flux qubit and demonstrate decoherence, entanglement and superposition. These three quantum physics phenomena are critical to the successful realization of a quantum computer. In general we seek to demonstrate the versatility of diamond as a technological material.
In summary the aims can be summarized as:

1. Demonstrate the viability of a hybrid quantum computer between superconducting flux qubit and NV centre in diamond on the IBM Q platform.
2. Characterise heavily boron doped (HBDD) thin films in order to investigate tunability through quantum phase transitions using a cryogenic high field measuring system (CFMS).

The results obtained here are very important as they will help to add to available knowledge on the research of diamond as a suitable material for hybrid quantum systems. Moreover, lessons learnt here will be used to support the current work on device fabrication in our lab.

1.5 Outline of the dissertation

This dissertation is split into parts which are quantum information processing and superconductivity in heavily boron doped thin films. The overall focus is to present a case for a hybrid quantum computer based on diamond as the quantum material. **Part 1** deals with boron doped thin films as possible material for superconducting devices whilst **Part 2** focuses on NV centers in diamond as crucial components for hybrid quantum systems.

Part 1: Superconductivity in heavily boron-doped diamond (HBDD) thin films

Chapter 1 covers the general introduction to all the work in this dissertation. Diamond is presented as a quantum material: NV- centers in quantum information processing and boron-doped diamond in circuit quantum electrodynamics to make resonators.

The theoretical study of 2D superconductivity and quantum phase transitions (QPT) in boron doped diamond thin films is presented in **Chapter 2.** Experimental methods, tools and the experimental setup we employ for characterisation in a cryostat high field measuring system (CFMS) are discussed in **Chapter 3**. **Chapter 4** presents the results of characterisation under the cryogenic high field measuring system (CFMS) and also the analyses.

Part 2: Quantum Information Processing

In **Chapter 5** we review all theoretical knowledge on quantum theory, quantum information processing and quantum technology giving special emphasis to superconducting flux qubit and the NV- centre in diamond. **Chapter 6** explains the digital simulation methods and gives practical details on the IBM Q platform and device IBMQx4. Results obtained and analyses thereof are presented in **Chapter 7.** Quantum algorithms are converted to unitary gates and run on the IBM cloud platform and results collected are used to plot graphs. Here we also make an interpretation of the results guided by theoretical knowledge given in **Chapter 6**.

We give an overall conclusion linking the two parts in Future directions and lessons learnt are shared. The main conclusion of this work is presented in **Chapter 8**. We reconcile quantum simulation of hybrid systems with superconductivity in diamond thin films as possible materials for quantum technology. Deductions are also made and future directions provided.

Superconductivity in heavily boron doped diamond (HBDD) thin films

Chapter 2

2.1 Introduction

Solid-state and atomic physics research and development are revealing underlying relationships between ordinary and exotic states of quantum matter. Superconductivity and localization in 2D materials affect each other in profound ways that warrant further study. Both are fundamental theories of superconductivity taking root on the BCS theory of superconductivity and the Anderson theory of localization **[7, 8, 9]**. They all breakdown in cases where disorder arises. Paired electrons called Cooper pairs are critical to superconductivity and thus the breaking of paired electrons will result in a loss of superconductivity. Fermionic Hamiltonian models show that there exists attraction between electrons and disorder that arises from random potentials that the single-particle density of states continues to show a hard gap across the disorder-driven quantum phase transition and that pairs continue to survive into the insulating state.

As disorder increases the superconducting transition temperature Tc does decrease until it vanishes at a critical disorder making way for a superconductor-insulator transition (SIT) **[10]**. The picture of the transition that emerges is a bosonic one, where phase fluctuations between localized Cooper-pairs in superconducting regions are responsible for the loss of superconductivity. While the role of the structural disorder is examined in the context of localization of electrons, other aspects emanating from structural disorder effects in the superconductor-insulator transition are subject to future studies.

Heavily boron doped diamond is a disordered, covalent superconductor with anomalous properties that can useful in quantum devices. Its behaviour makes it of fundamental interest in studying quantum phase transitions. Heavily boron doped diamond (HBDD) is a type II superconductor, with a Tc as high as 10 K depending on doping levels **[11, 12]**.

Diamond is intrinsically a high band-gap insulator with a band-gap of 5.5 eV. Boron can be substitutionally incorporated in diamond, creating a deep, narrow acceptor band 0.37 eV above the valence band. Our work in this section is to investigate specifically the phase fluctuations that drive what we suspect to be a disorder driven SIT ('dirty transition') in heavily boron-doped diamond (HBDD) thin films and their imprint on dynamical quantities as the transition is tuned **[13]**. Tunability is a useful electronic property that can is useful in high-performance superconducting devices.

2.2 Electronic transport in superconductors

Discovered more than a century ago, superconductivity is still a popular area of physics research. Natural or synthetic diamond does not exhibit the property of superconductivity; however, boron doped diamond displays relativistic quantum mechanics with interesting consequences that are worthwhile to investigate. The robust properties of diamond are envisaged to be employable in transmission line resonators used for superconducting quantum devices. There remains a lot to learn and uncover in this unique field of quantum condensed matter physics especially given the recent emergence of the field of quantum information processing. It is also a subject area that continues to attract attention from theorists and experimentalists alike.

Figure 2.1 shows superconductivity—a condition of exactly zero electrical resistance and expulsion of magnetic flux fields which occur in certain materials when the right environment is provided especially at low temperature. Bardeen, Cooper, and Schrieffer (BCS) theory attributes superconductivity to the pairing of electrons (Cooper pairs), thus creating a many-body coherent macroscopic wave-function. The electron pairing gives rise to a global order parameter Δ, which is defined by amplitude and phase. An increase in temperature suppresses the order parameter as similarly does exposure to a magnetic field.

Following the emergence of BCS theory, Anderson showed that weak disorder could not lead to the destruction of pair correlations. Later, Lee and Ma presented an argument that supported the role of disorder in destroying the superconducting state. Strong disorder gives rise to spatial fluctuations of the order parameter Δ along with its suppression in comparison with its value for the clean system, leading eventually to the destruction of the superconducting state.

This is called a superconductor-insulator transition (SIT) and has been observed in disordered thin superconducting films. Similarly, a magnetic-field-driven SIT has also been observed. This transition has stoked great interest, and a variety of theories, valid near the transition, have been put forward.

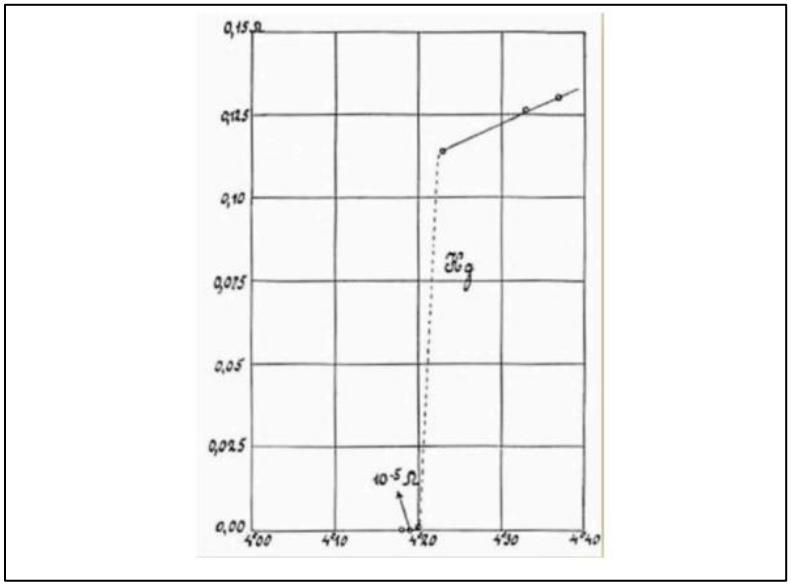


Figure 2.1: The first experiment demonstrating the phenomenon of superconductivity, discovered by Kammerlingh Onnes in 1911. When cooled below a critical temperature T_c = 4.2K, mercury displayed a complete lack of electrical resistance. ***[7]***

Anderson showed that superconductivity is quite robust against localization in three dimensions and exists in a variety of systems, it is more subtle in two dimensions where both superconductivity and localization are marginal. While it has been shown that superconductivity does exist in two dimensions, it can be lost by tuning many parameters, including temperature, disorder, gate voltage, and magnetic field. The system can enter a metallic state under these tunings, but more often than not, a superconductor-insulator phase transition occurs. This is an example of a quantum phase transition. The first experiments studying the disorder-tuned SIT in 2D were dc transport measurements on disordered superconducting films, where the disorder is enhanced by reducing the thickness of the films.

2.3 History and issues of 2D superconductors

Superconductivity in thin films on Pb and Sn was first reported in1938, by Shal'nikovs **[9]**. The thin films considered were in amorphous or granular forms. The random orientation of crystallites on the thin films were employed to study geometrical properties. As an example, orientation was overlooked but on investigating the angular dependence of the upper critical field, a cusp-like peak structure at the magnetic field direction parallel to the film plane was observed. This feature was adequately explained by the Ginzburg-Landau (GL) model as shown in **Figure 2.2**. Tinkham also pointed out in 1963 that the cusp-like peak is one of the clear characteristics of geometrical effect in 2D superconductors **[12]**.

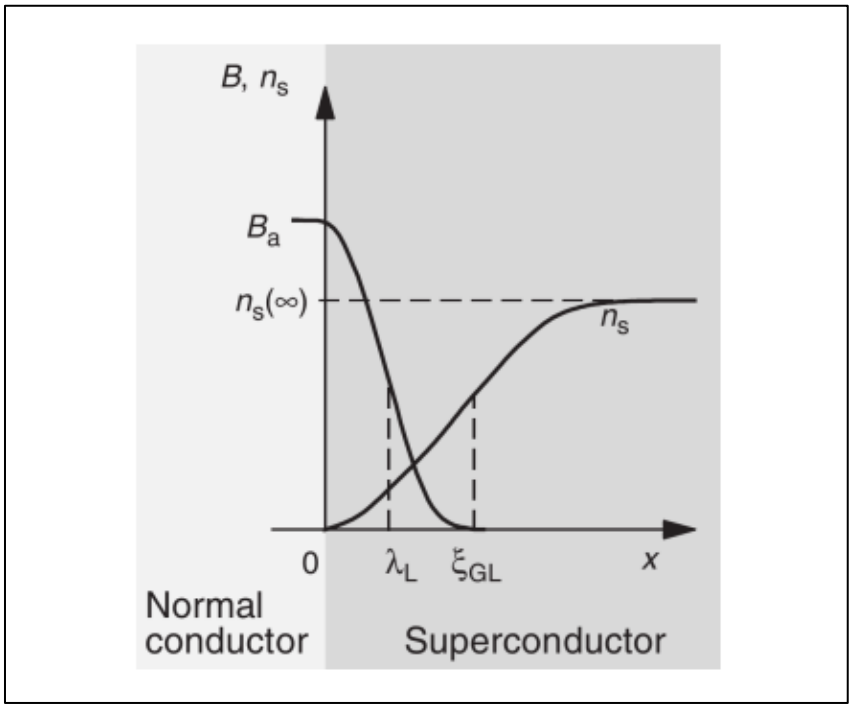


*Figure 2.2: At the boundary between a normal metal and a superconductor the magnetic field B and the superconducting wave function spatially varies according to the Ginzburg-Landau theory **[7]***

A superconductor is termed 2D when its thickness is thinner than the in-plane GL coherence length. Additionally, 2D superconductors show many other interesting properties such as localization, transition temperature oscillation by quantum size effects, excess conductivity originating from fluctuation, Berezinskii-Kosterlitz-Thouless (BKT) transition **[10]** and quantum phase transitions (QPTs) **[11]** at zero temperature.

The BKT transition is observed when we get a jump in the power-law exponent when the applied current is at zero current limits while investigating current-voltage characteristic. The disappearance of ohmic resistance obeying the Halperin-Nelson scaling law is treated as the evidence of 2D superconducting transition through the binding of vortex-antivortex pairs.

Quantum phase transitions in 2D superconductors are critical in quantum devices. The superconductor-insulator transition (SIT) in metallic thin films was believed to occur only at zero temperature limit as a function of external tuning parameters, such as disorder (or film thickness), out-of-plane magnetic fields and carrier density (or electric fields), which determine the ground state of the system. The SIT in disordered systems can be divided into two groups: one is originating from the amplitude fluctuation of the order parameter, and the other includes the phase fluctuation. Fisher and others proposed a “dirty-boson” model, considering that the SIT is caused by the quantum fluctuation of the phase and long-range Coulomb repulsions (interacting Cooper pairs).

In the case of magnetic field induced SIT, this model can be understood from self-duality of Cooper pairs and vortices: the superconducting phase is described by a condensate of Cooper pairs with the localized vortices (vortex glass), while the insulating phase is a condensate of the vortices with localized Cooper pairs (Bose glass).

2.4 Nature of the transition in BDD thin films

Because the superconductor-insulator transition involves both the physics of paired electrons (BCS theory) and disorder-induced localization (Anderson localization), a natural question to ask is how these two mechanisms conspire to induce the quantum phase transition. Is the mechanism primarily fermionic, resulting from the disorder-induced breaking of Cooper-pairs? Alternatively, is it primarily bosonic, resulting from the localization of paired states?

What can be seen even in the earliest work is emergent inhomogeneity; the regions of superconducting order occur over a length scale given by the correlation length, while the disorder is determined by homogeneous randomness.

The picture that emerges is that phase fluctuations between regions of localized superconducting pairs induce the phase transition as shown in **Figure 2.3**.

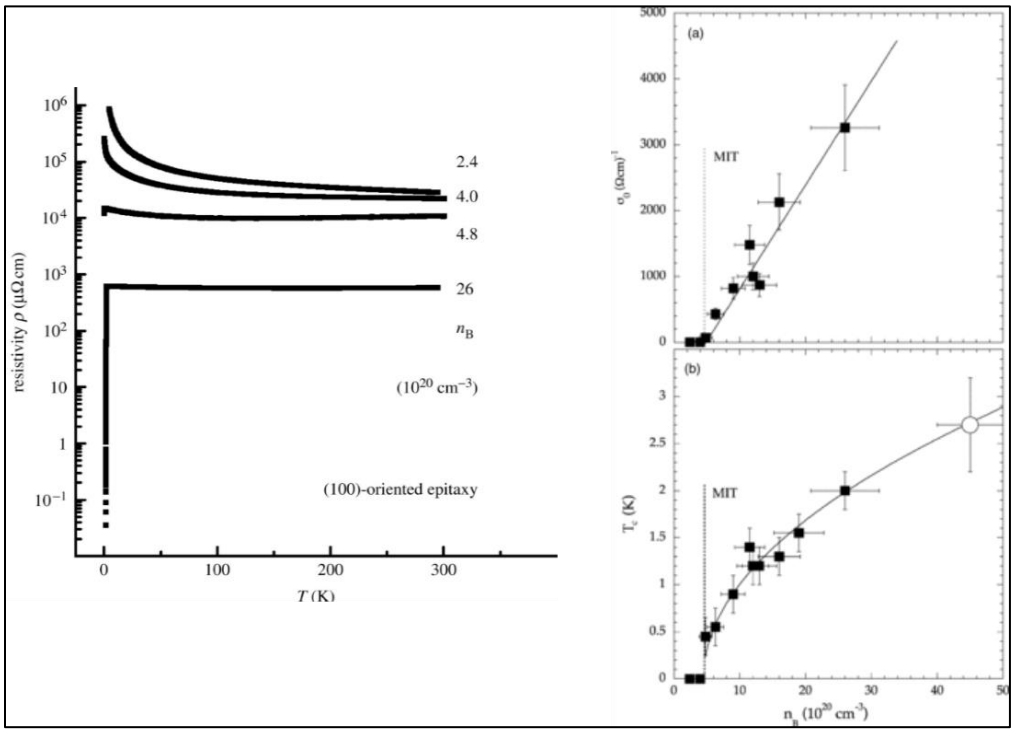


Figure 2.3: Various experimental findings regarding the transport properties correlated to boron concentration (a) the temperature dependent resistance showing the insulator-metal transition with increasing doping concentration. (b) The conductivity as a function of boron concentration (c) The critical temperature as a function of boron concentration

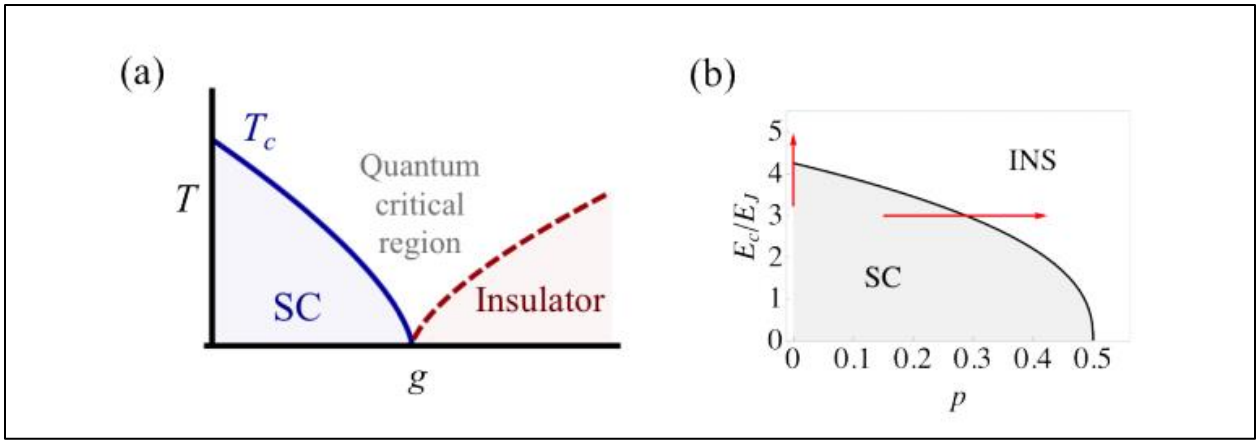


Figure 2.4: (a) Generic description of quantum phase transition phase diagram for the SIT. The insulating and superconducting phases each have characteristic energy scales that vanish at the quantum critical point. Between these regions, a quantum critical region is present near the critical point. (b) Schematic phase diagram for the disordered Josephson junction model. A transition in the disorder-free ("clean") model can be tuned by changing the ratio of charging energy to Josephson energy (E_c/E_J). Alternatively, at any intermediate E_c/E_J, a disordered transition can be tuned by removing a fraction of Josephson sites (p).

The emergent inhomogeneity of local superconducting quantities and the persistence of a hard gap in the insulating state have been seen in thin films across the SIT in STM experiments, in excellent agreement with the numerical work as illustrated in **Figure 2.4**. Magnetoresistance oscillations have provided other experimental evidence that the SIT is bosonic in nano-honeycomb patterned films **[13]**.

2.5 Mechanisms of superconductivity in thin films

Superconductor-insulator (SIT) transitions are described using a variety of models since there is none that seems to cater for all experimental observations. The challenges encountered are similar what the BCS model faces in accounting for superconductivity. It therefore, helps to approach the analysis from different angles in order to build an integral picture of the SIT phenomenon. We summarize some of the suggested mechanisms below.

Bosonic model of SIT

Bose-Einstein statistics tell us that below a certain threshold temperature an ensemble of particles settle in an equilibrium state forming what we call Bose condensate. This is the lowest quantum state preferred by the system. In the Bose ground state there are no exclusive rules hence all particles can occupy the state at once. We find there are macroscopic cases where applying the Bose model is helpful. A Bose condensate is readily applicable to a gaseous system of interacting charged Bose particles **[13]**. However, Bose particles physics also suffices for a system of non-interacting Bose gas particles spread apart by short-range fields of impurities. Considering a gas of weakly interacting Bose particles which repel each other and also interacts with the impurities.

Bose condensation means the existence of superconductivity with a London penetration depth $\lambda_0^2 = mc^2/4\pi n$ where m and n are the effective mass and the density of bosons with the conductivity $\sigma(\omega)$ as $\omega \to 0$: $\sigma(\omega) = i\frac{c^2}{4\pi}\frac{1}{\lambda^2}\frac{1}{\omega}$, $\lambda = \lambda_0 \frac{1}{\sqrt{1-A}}$ where A is a dimensionless parameter related directly to disorder. It has been observed that transport properties of the system suddenly change at A=1. For A < 1, the system possesses infinite conductivity and shows superfludity at $\omega = 0$. At A=1, a quantum phase transition from the superfluid state to the state of localized bosons (Bose glass) occurs. The occurrence of a transition follows from the divergence of λ as $A \to 1$. This behavior is characteristic of the gas of charged bosons in the field of charged impurities.

Now, the condition A=1 connects the concentrations of the scattering impurities (N) and the bosons (n). At the critical concentration of impurities N_c namely $N_c \propto n^{\frac{5}{4}}$ a transition from the state of an ideal conductor to an insulating state occurs. All the bosons condense into the localized state if there is no interaction giving rise to an insulator. The interaction between bosons stabilizes superconductivity whilst instability in a system of non-interacting bosons supports the insulation phase. As would be expected a decrease in the boson concentration weakens interaction and, therefore, the critical concentration of impurities decreases, as well.

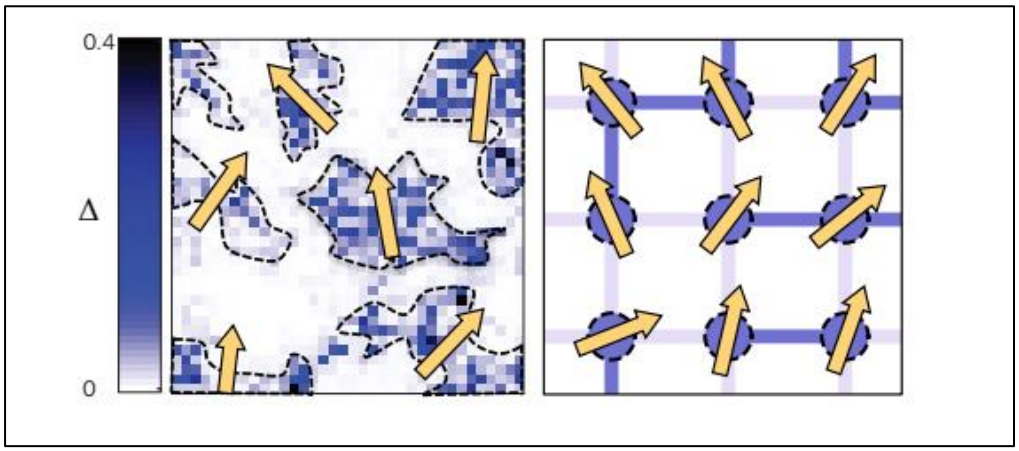


Figure 2.5: Modelling disorder driven effects using the Josephson junction array approach.

The quantum XY model is equivalent to a Josephson-junction array shown in **Figure 2.5**, with the Hamiltonian

$$\hat{H}_J = \frac{E_c}{2}\sum_i \hat{n}_i^2 - \sum_{\langle ij\rangle} J_{ij}\cos(\hat{\theta}_i - \hat{\theta}_j) \qquad \textbf{(1)}$$

Where the number operator $\hat{n}_i$ at site i is canonically conjugate to the phase operator $\hat{\theta}_i$. In this case E_c is the charging energy. The Josephson couplings are shown in **Figure 2.6** $J_{ij} = E_J$ with probability (1-p) and $J_{ij} = 0$ with probability p. The clean system (p=0) is a coherent superconductor when E_J dominates over E_c, with phases aligned across all the junctions. However, large E_c/E_J favours a well-defined number eigenstate, leads to strong phase fluctuations, and drives the insulating state.

Thus E_c/E_J can be used to tune across the SIT in the clean system. A quantum phase transition can also be induced by increasing disorder p (bond dilution) for fixed $E_c=E_J$. Disorder is introduced into the quantum model by breaking bonds ("Josephson couplings") on a 2D square lattice with a probability p.

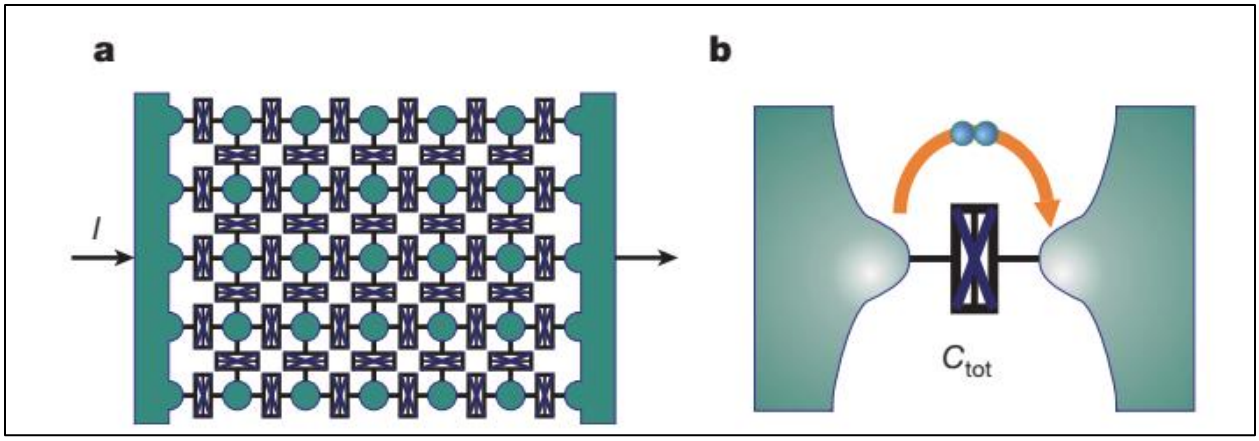


Figure 2.6: (a) The Josephson coupled weak links between the islands as crossed rectangles. The green circles are superconducting islands. (b) Phase synchronization allows us to view the 2D Josephson junction array as a single effective junction with the effective capacitance C_{tot} = C/lnN

The Berezinskii-Kosterlitz-Thouless (BKT) transition

An outstanding property of 2D superconducting systems is that it is sometimes convenient to view the system as possibly made up of a chaotic gas of magnetic vortices that are at temperatures lower than T_{c0} of the macroscopic SIT. A magnetic flux quantum $\phi_0 = \frac{2\pi\hbar c}{2e}$ passes through each vortex. The factor of 2 in the denominator of the relationship is conserved in order to highlight that Cooper pairs determine the quantization. The magnetic flux penetrate through each vortex and generate opposing fields on the axis and after a certain time disappear due to dissipation because of collisions. In the absence of a magnetic field there is equilibrium in the vortex concentration, $N_- = N_+$; this is due to a balanced spontaneous generation and annihilation process. A decrease in temperature to $T_C \equiv T_{BKT} < T_{c0}$ leads to a Berezinskii–Kosterlitz–Thouless (BKT) transition.

The generation of vortex pairs ceases, and the concentration of vortices decreases sharply and becomes exponentially small. Thus, in a certain temperature range $T_c < T < T_{c0}$ in two-dimensional superconductors, the vortices coexist with Cooper pairs.

The magnitude of the binding energy Δ of a Cooper pair in between the vortices falls to zero on the axis of the vortex. Deterioration of the order parameter leads to the vanishing of superconductivity and restoration of normal electron behavior in the vicinity of the vortex axis. Since the vortices are in continuous motion, it causes the phase of the order parameter in the space to fluctuate. The vortices being quasiparticles are considered to behave as normal bosons. This situation of free vortices gives rise to resistance albeit the system having 2e-bosons (Cooper pairs). In 2D superconducting films ($d \ll \xi$) even at in the absence of a magnetic field, vortices can be spontaneously created below the mean-field critical temperature T_{c0} as shown in **Figure 2.7**.

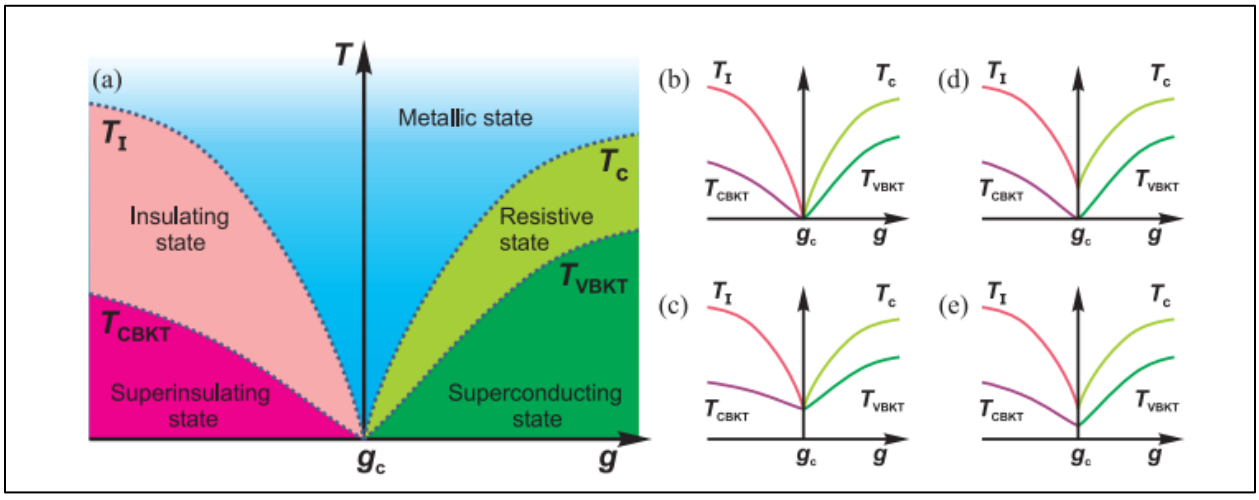


Figure 2.7:(a) Phase diagram for the superinsulator-superconductor transition in two dimensions; (b) The case where at the critical point all the transition temperatures turn zero;(c) First order transition between the superconductor and superinsulator; (d) $T_{CBKT}(g_c) = T(g_c) = 0$, but $T_I\ g_c) = T_c(g_c) \neq 0$; (e) $T_{CBKT}(g_c) = T_{VBKT}(g_c) \neq 0$ and $T_I\ (g_c) = T_c(g_c) \neq 0$;

The energy budget for the spontaneous creation of just one vortex in a field axis perpendicular to the film-plane of volume $\sim \pi\xi 2d$ is

$$E_v = \left(\frac{\emptyset_0^2}{4\pi\lambda_\perp \mu_0}\right) \ln\left(\frac{\lambda_\perp}{\xi}\right) \qquad \textbf{(2)}$$

For a sample of size R in a simplified model, and R << λ, the logarithmic term is replaced by ln(R=ξ). In the case of Berezinskii-Kosterlitz-Thouless (BKT) phase vortex-antivortex pairs with counteracting circulation are generated by thermal activation.

It is the intervortex separation ~ R_{12} other than R that sets the total energy of the vortex-pair creation as:

$$E_{v-pair} = 2 \cdot \left(\frac{\emptyset_0^2}{4\pi\lambda_{\perp}\mu_0}\right) \ln\left(\frac{R_{12}}{\xi}\right) \qquad \textbf{(3)}$$

Our theory so far has accounted for vortex driven BKT, but there is another approach which is specifically introduced to address Josephson junction arrays (JJAs) and is based on Coulomb interaction called charge BKT.

This mechanism leads to phase changes of bound charge anti-charge pairs as well as free charges shown in **Figure 2.8**. The array consists of superconducting islands coupled to each other via tunnel junctions. The distance d separates two superconducting islands that contain a net charge of opposite spin. This pair polarize the neighboring islands but do not contain any net charge. According to the BKT-mechanism the transition temperature equation $k_B T_{BKT} = \frac{E_C}{4\pi\epsilon_c}$ with ϵ_c slightly larger than one. In the superconducting state the charge is 2e and transition temperature $k_B T_{BKT} = \frac{E_C}{4\pi\epsilon_c}$.

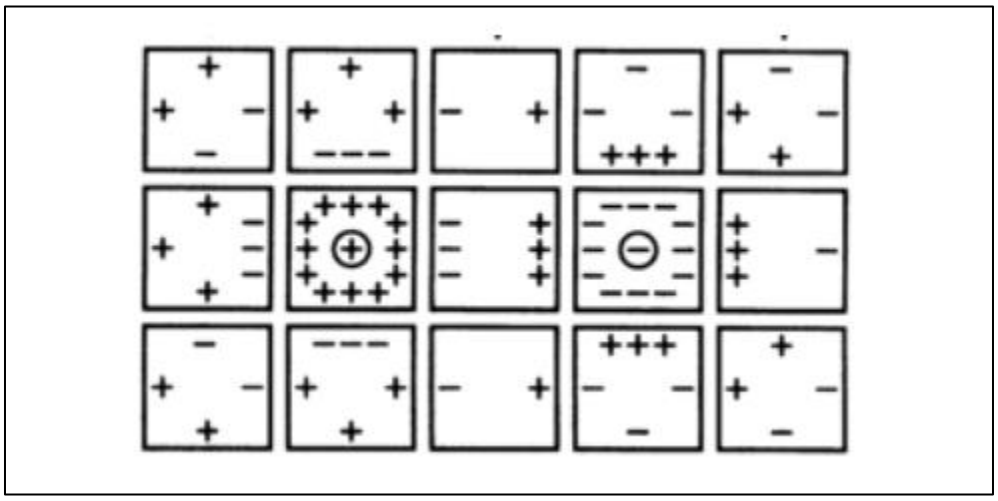


Figure 2.8: Charge distribution for a charge anti-charge pair in a Josephson junction array ***[14].***

Above T_{BKT} we have free charges given by $n_c = \exp(-\frac{2b}{\left(\frac{T}{T_{BKT}}-1\right)^{\frac{1}{2}}})$ which is a similar expression to the one on free vortices in the vortex BKT transition. It follows that for a system below T_{BKT} the charges are stationary and the array is insulating.

Superconducting fluctuations

According to the BCS model, the order parameter amplitude at the mean-field critical temperature Tc0 has a finite value while on the contrary thin films still exhibit resistance until the temperature is below the vortex BKT transition temperature T_v-BKT. In the situation where temperatures exceed T_c (B) with B > B_{c2} (T), fluctuations in superconductivity play an active role to influence the conductivity of 2D films. Further, above Tc aspects like weak localization and disorder enhanced interelectron interference due to the Aronov-Altshuler effect should be taken into consideration in thin film analyses **[14].**

Weak localization effects are due to the diffusive motion of single electrons in 2D superconductors. Let us consider an electron that is at initially at rest (time t = 0, r = 0). Suppose it takes part in diffusion motion with Fermi velocity v_F and its mean free path l = $v_F\tau$, where 1=τ is the frequency assigned to the elastic scattering events due to collisions. Therefore, the probability for the electron to be found at a position r after a time t=τ is given by the expression;

$$p(r,t) = (4\pi Dt)^{-d/2} e^{\frac{-r^2}{4Dt}}, r^2 = \sum_1^d x_i^2, \int p(r,t)dr = 1 \qquad \textbf{(4)}$$

where d is the dimension of the system and D = lv_F=d is the diffusion coefficient. Without getting stuck in mathematical trivia, the electron goes and returns to the same place thereby traveling the same path twice. It, therefore, valid to say if the time through which back and forth motion occurs is small enough then the electron interferes with itself. Interference is a quantum mechanics aspect, so the probability density of locating the electron in its path is double the classical case. The implication of the interference is to lower conductivity. In a situation of increasing disorder then conductivity is further suppressed.

There is another case that we can consider where two different electrons traverse the same path and interfere. This is an interelectron interaction and the laws of superposition applies. In order to interfere constructively the two electrons need to have the same phase of wavefunctions at the starting time (t=0). This effect is called the Aronov-Altshuler effect **[14]**. This diffusion motion only happens for electrons that have energies around the Fermi level E_F.

Vortex-based resistive mechanisms

When a magnetic field is applied perpendicular to the plane of a 2D disordered superconducting film with $\kappa < 1=p_2$ it allows vortices to penetrate to a depth of $a_0 = (\varphi_0=B)$. If a current is applied through the superconducting film, then we have a Lorentz force that moves vortices perpendicular to the current direction and the edges of the film. Aggregation of these vortices on the edges of the film induces an electric field which is parallel to the applied current and acts as a resistive voltage. If the vortices are fixed to specific local sites in the superconducting film in a process called pinning then their migration to the edges would be impeded. In the case of strong pinning, then no vortex movement can occur, and there is a threshold value of current that has to be exceeded so that the Lorentz force overcomes the pinning forces.
Bardeen and Stephen approximates the flux-flow resistance by assuming a viscous drag coefficient η. The viscous force on a vortex with velocity $\mathbf{v}L$ is then $\eta\mathbf{v}L$. They found that η is related to the upper critical field $Hc2$ and the normal state resistivity ρn in the following way:

$$\eta \approx \frac{\emptyset_0 H_{c2}}{\rho_n c^2} \qquad \textbf{(5)}$$

where c is the velocity of light in vacuum. For the flux-flow resistance ρ_f they found

$$\frac{\rho_f}{\rho_n} \approx \frac{B}{H_{c2}} \qquad \textbf{(6)}$$

Inui, Littlewood, and Coppersmith **[15]** used a model of single vortex depinning to account for the thermally activated motion of vortices.
The barrier height for low temperatures activated motion of vortices for two different types of field dependence:

$$V_{barrier} \approx \begin{cases} V_0 + \sigma \ln\left(\frac{H_0}{H}\right), & H \ll H_1 \\ V_0 - \frac{\pi^2\gamma}{K^2}, & H \gg H_1 \end{cases} \qquad \textbf{(7)}$$

There is an alternative explanation which uses the approach of the collective creep model. It applied in the case where the activation energy comes from an applied magnetic field.

The temperature and field dependence of the resistance of the 2D flux line lattice pinned vortices determines the motion of dislocations. **[16]**.

Phase slip centers and heating in superconducting thin films

Scocpol, Beasley, and Tinkham (1974) were successful with an explanation of the low-bias as well as the high-bias behavior of current-voltage (IV) characteristics of superconducting thin film microbridges. From their analysis increasing the bias current to levels above the critical current Ic causes the voltage to increase in a series of steps rather than continuously as would be expected. This approach based on phase-slip centers is referred to as the SBT model after the authors of Ref. **[17]**.

Phase-slip centers (PSC) are the resistance centers created for every step change in voltage when the current is varied. Given that a superconducting microbridge is typically not uniform there an uneven variation in the magnitude of the current that flows through it. This inhomogeneity causes a variation in Ic. Exceeding the critical current Ic diminishes the order parameter and brings about resistivity. The resistivity works against the applied current until it falls below Ic in which case superconductivity returns.

The **IV** relationship for this situation is shown in **Equation 8**:

$$V = \frac{2\Lambda_Q \cdot \rho}{A}(\mathrm{I}\text{-}\beta I_c) \qquad \textbf{(8)}$$

Due to reduced dimensionality, 2D films have phase slip lines instead of phase slip centers. Vortices flow in so-called vortex rivers traversing the microbridge vertical to the applied current. The IV characteristics of 2D films behave like for PSCs in that as the flow of current is continuously increased heat is generated in the material thereby thermalizing it. This increase in temperature results in the vanishing of the order parameter and onset of resistivity. Thermal healing **[18]** due to heat dissipation mechanisms within the film leads to a characteristic thermal healing length $\eta_{N,S}$, for the normal conducting/superconducting regions respectively, given by

$$\eta_{N,S} = (K_{N,S}d)^{1/2}$$

Fermionic mechanism for the superconductivity suppression

In some cases, quantum phase transitions are driven by fermionic scenarios where the modulus of the order parameter vanishes with increased impurities in the system. To adequately address behavior using this approach we have to go beyond the limits of the validity of the Anderson theorem. This suggests that we should consider both Coulomb interaction between the electrons and disorder. Our first assumption shall be that of a granular system where the impurity concentration increases. The Coulomb interelectron interaction due to the Aronov–Altshuler effect **[19]** dominates and suppresses the density of states at the Fermi level for the granules.

The effect of this is to increase the spacing between the energy levels and decrease the temperature Tc of the superconducting transition. As the level of impurities rises the Coulomb interelectron interaction itself is renormalized **[20]**, and the processes of repulsion of electrons with opposite momenta and spins, which lead to a low transfer of the momentum, become stronger.

The result of Ref. **[20]** resembles the suppression of the density of states g_0 at the Fermi level in a normal dirty metal by the Coulomb interaction, with the difference that in the superconductor it is the temperature Tc that decreases with increasing disorder, rather than the density of states g_0 at the Fermi level.

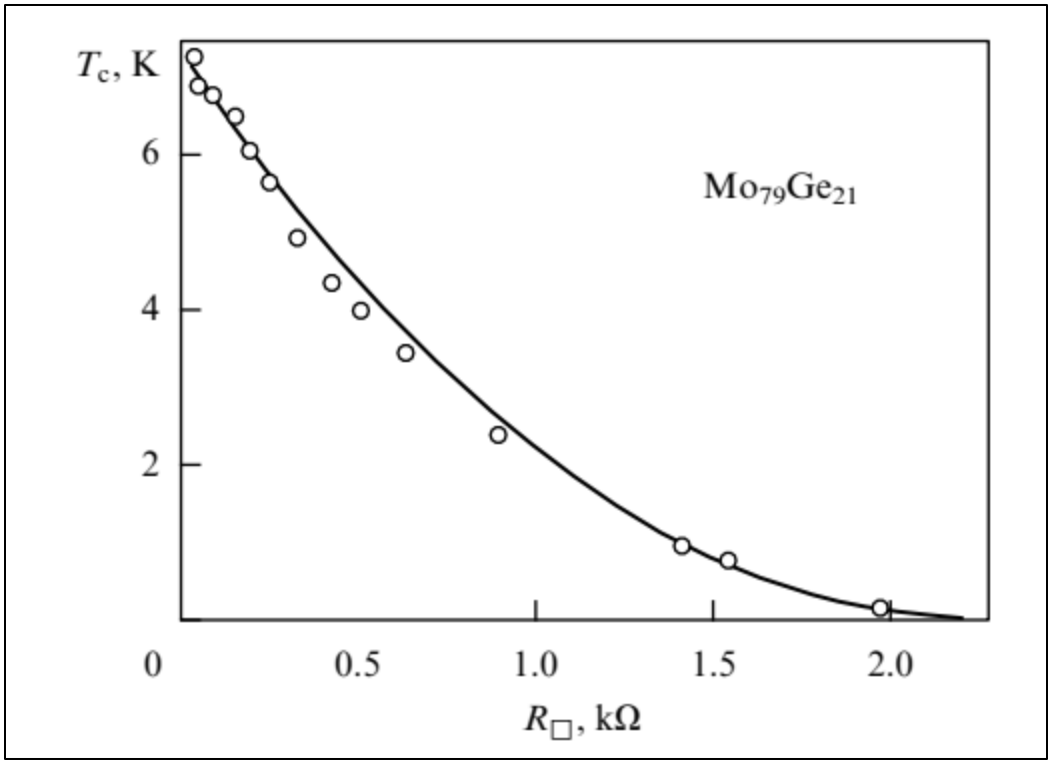


Figure 2.9: Disorder driven reduction in Tc in amorphous $Mo_{79}Ge_{21}$ films [22].

In the 2D case as we see in **Figure 2.9** we typically have

$$T_c = T_{c0}\left[1 - \frac{1}{12\pi^2 y} ln^3\left(\frac{\hbar}{T_c \tau}\right)\right], \qquad \textbf{(9)}$$

where y is the dimensionless conductance: $y = \frac{\hbar}{e^2 R_\square}$ where $R_\square$ is the resistance per square (resistivity of a 2D system, or resistivity per square), and t is the relaxation time of the momentum in the normal state. The expression in **(9)** shows the possibility of reducing Tc as disorder increases. As expected from theory, the critical temperature reduces with increase in disorder under the superconducting transition.

Unconventional transport features

The first studies on superconducting boron-doped diamond claimed a regular BCS features where vortices form an Abrikosov triangular lattice **[23]**. Accordingly Later more precise measurements indicated that the superconductivity follows the granular structure with mostly well connected, transparent grain boundaries and fewer more weakly coupled (opaque) boundaries.

The strong coupling between grains gives rise to proximity effects that occur in weakly superconducting grains and inverse proximity effect in strongly superconducting grains. Additionally, quasiparticle excitations below the superconducting energy gap were observed within the vortex core. This is significant when taking into account some of the theoretical investigations regarding the relationship between odd frequency superconductivity and vortex bound states.

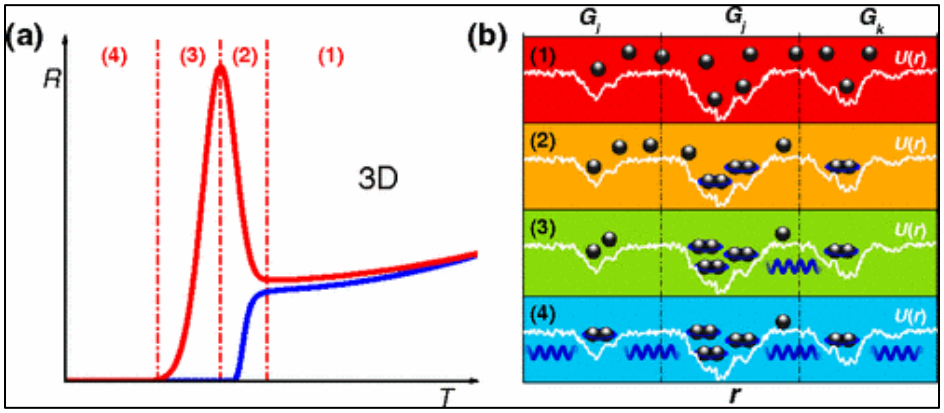


Figure 2.10: One of the first transport features signifying unconventional superconductivity was the re-entrant bosonic anomaly reported by Zhang et al. This feature was explained with in a resistive network model composed of bosonic islands within the diamond grains that eventually reach global coherence and hence the superconducting phase. Figure taken from ref. ***[23]***

More recently however additional unconventional features have been observed in the transport of nanocrystalline samples. Re-entrant peak structures in **Figure 2.10** the T_c that are strongly field dependent were demonstrated by several group **[24]**. The re-entrant peaks where initially explained to exist due to the formation of a bosonic insulator phase. As the system is conventionally assumed to be 3D the peak was called anomalous as such Bosonic insulator excitations are typical for low dimensional (i.e. 1D and 2D) systems only. The formation of this so-called anomalous bosonic insulator was ascribed to be due to confinement effects thanks to the granular nature of the system. The resistance upturn was phenomenologically explained as a result of normal state electrons being removed from the conduction channels as they pair, forming phase-locked bosonic droplets within the grains, as the temperature is decreased the bosonic islands grow and eventually couple between grains, resulting in the global phase coherence and a fully superconducting state.

This explanation is dependent on a two-step process involving normal electron conduction separated in temperature from the global phase coherence and coupling (intergrain) tunneling. This concept however lacks any theoretical backing and analysis was based purely on the authors own empirical model and thus does not yield any additional information especially regarding the nature and properties of such a bosonic insulator phase. To date the boron doped superconducting system has been analyzed in terms of 3D quantum transport. Our aim is to investigate the possibility of a 2D phase.

Superconductivity in reduced dimensions are well known to exhibit interesting physics **[25]**, in particular superconductivity in 2D has been investigated with regard to non-trivial topological ordering due to spontaneous time reversal symmetry breaking. Such non-trivial topological superconductors are generally described in terms of odd-parity and spinless wavefunction and have been observed experimentally only in a handful of materials. Since topologically protected states are expected to be useful for decoherence robust qubits **[26-29]**, much research is directed at identifying potential materials offering such exotic low dimensional phases.

Low dimensional effects of superconductivity have generated a large amount of interest. This is due to the interesting physics that accompany the condensation of Cooper-pairs in two dimensions (2D). The field experienced rapid development with both the theoretical backing and experimental investigation into the quantum critical phase transition that occur due to the increased interaction of fermions. One of the first realizations of 2D superconducting planes was within the high temperature cuprate superconductors. This was thanks to the crystalline structure of such materials, where conduction typically occurs within crystal planes with weak coupling between planes. Superconductivity in 2D is predicted to allow for the formation of rare and interesting quasiparticle excitations.

High Field Effects

According to the BCS model, Cooper pairs appear either through the fluctuation mechanism at temperatures exceeding T_c or, for $T < T_c$, in the magnetic field with $B > B_{c2}(T)$. The influence of Cooper pairs to conductivity is very high in superconductors.
However, there is also interest in knowing if ever there are cases when accepted knowledge breaks down and anomalous behavior has been observed primarily in granular superconductors. In the plane (T, B), the region of existence of fluctuations is that where $B>B_{c2}(T)$, including $T>T_c$ $(B=0)\equiv T_{c0}$ at B=0 as shown by **Figure 2.11**.

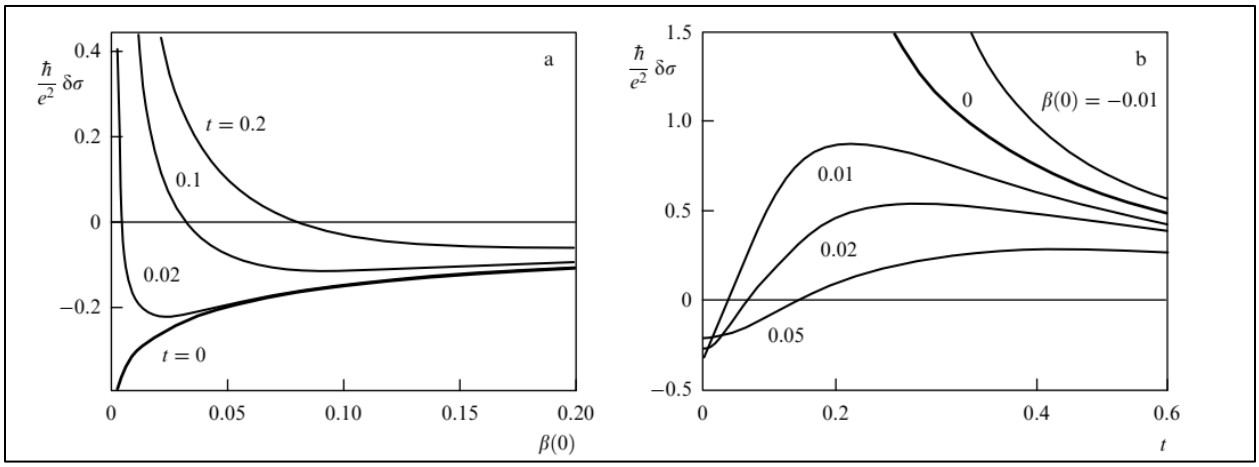


*Figure 2.11: 2D dirty superconductor as a function of (a) magnetic field at different T, and (b) temperature at different B-strengths **[4]**.*

Technological capabilities now allow for the characterization of 2D thin films at more demanding temperatures $T \ll T_{c0}$, $B>B_{c0}$. The relationship between the electric field and the drift velocity is initially linear until thermal velocity dominates and the relationship changes. When a system of electrons in 2D establishes thermal equilibrium, the carriers emit both and absorb phonons giving rise to a net zero energy scenario. At this point the energy distribution is Maxwellian. Any energy acquired from the electric field by the carriers is given lost to phonons. For diamond and other semiconductors at fields less than 103V/cm the current density J_x is proportional to the electric field as in **(42)**,

$$J_x = \sigma E_x, where\ \sigma \equiv \frac{nq^2\tau_c}{m_n} \qquad \textbf{(10)}$$

where n is the electron density, and m_n is the effective mass of an electron.
The most common scattering event when it comes to reasonably high fields is through the emission of optical phonons. In this case the carriers have acquired more energy than the lattice and thermal parameters rendering **Equation 10** invalid.

By increasing the electric field in a semiconductor, the carriers keep on acquiring energy until they have enough kinetic energy to excite electron-hole pairs by impact ionization. The rate at which the electron-hole pairs are generation G is given by

$$G = \alpha_n n v_n + \alpha_p p v_p \qquad \textbf{(11)}$$

Where α_n is the ionization rate defined as the number of electron-hole pairs generated by an electron per unit distance travelled. A physical expression for the ionization rate is given by

$$\alpha(E) = \left(\frac{qE}{E_I}\right)\left\{\exp -E_I/[E\left(1 + \frac{E}{E_p}\right) + E_{kt}]\right\} \qquad \textbf{(12)}$$

where E_I is the high field, effective ionization threshold energy, and E_{kt}, E_p, and E_I are thresholds fields for carriers to overcome the decelerating effects of thermal, optical-phonon and ionization scattering, respectively.
In conclusion, some of the phenomena we have encountered like an increase in resistance due to superconducting fluctuations and negative magnetoresistance apply not only to 2D thin films but also to dirty quasi-homogeneous superconductors.

Chapter 3

Experimental Methods

Our work here focuses on characterization of a disordered heavily boron-doped diamond thin film sample herein referred to as B4 at low temperatures (280mK) and high fields (12T). We investigate quantum phase transitions and account for their occurrence on the basis of resistance-temperature (RTs), current-voltage (IVs) and magnetoresistance (MRs).

3.1 BDD Sample properties

Sample	CH_4/H_2	Grain size	T_C	T_{BKT}	ξ
B5	5 %	30 nm	1.79 K	1.31 K	10.8 nm
B4	4 %	50 nm	1.21 K	0.59 K	-
B2.5	2.5 %	70 nm	0.98 K	-	27.5 nm

Table 3.1: Comparison of the properties of three films from which a sample as highlighted was taken for this study including synthesis conditions, grain size, critical temperatures and coherence lengths.

The device investigated in this thesis consists of a silicon wafer substrate coated with a BDD thin film. The HBDD sample highlighted in **Table 3.1** which is the subject of this dissertation was synthesized using microwave plasma enhanced chemical vapour deposition (MWCVD). This diamond sample was grown with 4% CH_4 in H_2 (henceforth named B4) with trimethylborane (TMB) as a dopant precursor on quartz substrates. The estimated concentration of boron is ~4000 ppm though it is not an indication of carrier concentration. Film thickness can be determined through spectroscopic ellipsometry (E) which is an optical measurement technique based on the change in polarization occurring at many wavelengths. Ellipsometry is often highly sensitive to the properties of 1 nm to 10 μ thick films. The spectral response provides information about the sample properties, such as film thickness, surface conditions such as surface roughness (or the presence of surface contaminants), film thickness uniformity,

anisotropy, and some important physical properties, such as refractive index. **Table 3.2** gives predicted characterisation values for sample B4.

Sample	T_c (K)	B_c (T)	I_c (μA)	Δ (meV)	D (nm)
B1	3.6	2.5	>800	0.56	100
B2.5	1.2	0.9	25	0.18	60
B4	1.8	1.0	40	0.27	70
B5	2.0	1.1	20	0.30	30

Table 3.2: The analysis presented in this work has been conducted on data generated from four boron-doped superconducting diamond films of differing grain size. In the table below the thermodynamic properties such as critical temperature, critical field, critical current, superconducting energy gap and grain size is listed.

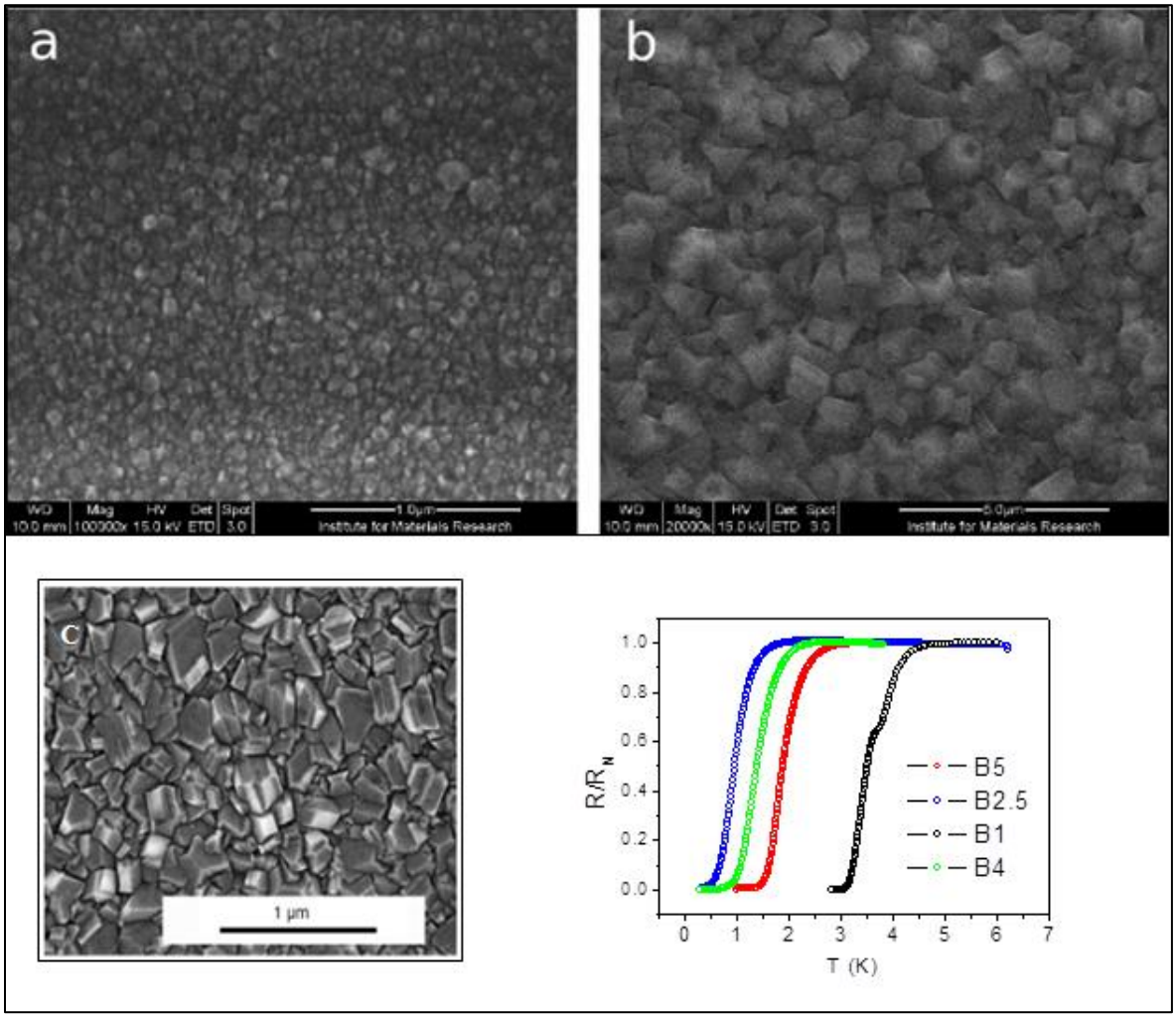


Figure 3.1: (a)-(c) SEM images of the surface of one of the boron doped samples.

The average grain size is determined from SEM imaging and is given in **Figure 3.1**.

The graph in **Figure 3.1** shows the temperature dependent resistance of the films. All films are of the same thickness. The samples investigated in this work were synthesized using microwave plasma enhanced chemical vapor deposition (MPCVD). The diamond samples were grown on quartz substrates (1cm x 1cm) with 1% and 5% CH4 in H2 with trimethylborane (TMB) as a dopant precursor. The ratio of TMB:CH4 during synthesis was ~4000 ppm. Scanning electron microscopy images show that boron doped samples have a granular surface morphology. The average grain size is determined by averaging the grain size over a specified surface area as viewed through the SEM imaging. The grain sizes for the respective samples are found to vary from 20-30 nm for sample B5 (5% CH2/H2) and 100 nm for sample B1 (1% CH2/H2).
The sample was prepared through the following steps after mounting on sample holder:

- Use lab detergent to sonicate and remove oils and fats on sample then rinse using deionized water.
- Clean with acetone and isopropanol respectively in ultrasonic vibrator, 5 mins each in order to remove contaminants.
- Use nitrogen gas to blow dry the sample.

3.2 Instruments and Measurement procedures

Cryogen-Free Measurement System (CFMS)

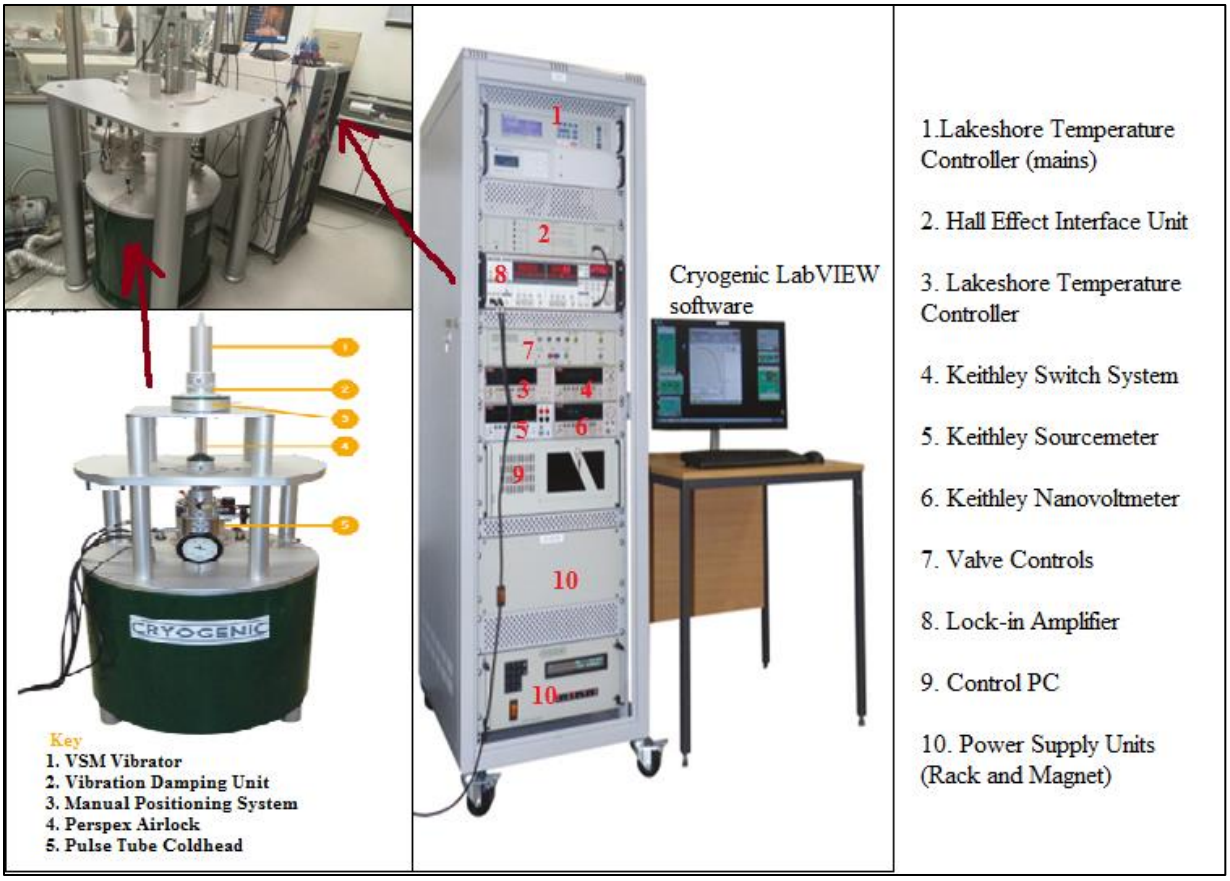


Figure 3.2: Cryogenic High Field Measurement System

The CFMS shown in **Figure 3.2** is made up the following components:

- Cryostat and magnet

  The cryostat is a vacuum insulated chamber whose main function is to support and thermally protect the superconducting magnet and variable temperature insert (VTI). The magnet is a solenoid wound from copper stabilized filamentary superconducting wire oriented vertically.

- Cryo-cooler system

  Cooling of the system is made possible by a standard two-stage cryo-cooler. The first stage is mainly used to cool the outer chamber that acts as a radiation shield. The magnet and VTI are cooled to 4K and below the second stage.

- Variable temperature insert (VTI)

  The ability to vary temperature of the sample between 1.6K and room temperature is made possible by the VTI.

- Electronic Units

  The electronics for the basic system consists of controllers for temperature, valve blocking, superconducting magnet and rotary pump; control computer, lock-in amplifier, measurement system interface unit.
- Measurement system software

  The CFMS is accessible via a LabVIEW software suite. It controls system operation and measurement protocols, and also provides the user with remote access and the flexibility to develop custom made measurement recipes.

A Cryogen Free Superconducting magnet with an Integrated Variable Temperature Insert (VTI) as well as an automatic needle valve allow for easy control of the CFMS. Highly stable and sensitive electronics allow for the performance of accurate magnetic, electrical, thermal property and ultra-low temperature measurements. The magnet configuration of this particular instrument is up to ±12 Tesla with active shielding and a standard temperature range of 1.6 K – 400 K. In order to extend the range of experimental temperatures in the CFMS beyond the standard operating range, a Helium-3 probe is employed. Liquefied Helium-3 is the working agent for the cryostat. A reduction in the vapor pressure results in a decrease in the temperature.

Figure 3.3 shows the Helium-3 insert which is operated between 300mK and 300K through control of the VTI and internal temperature-controlled sorption pumps. It comes as an additional extension to the standard CFMS aimed specifically for resistivity and Hall Effect measurements.

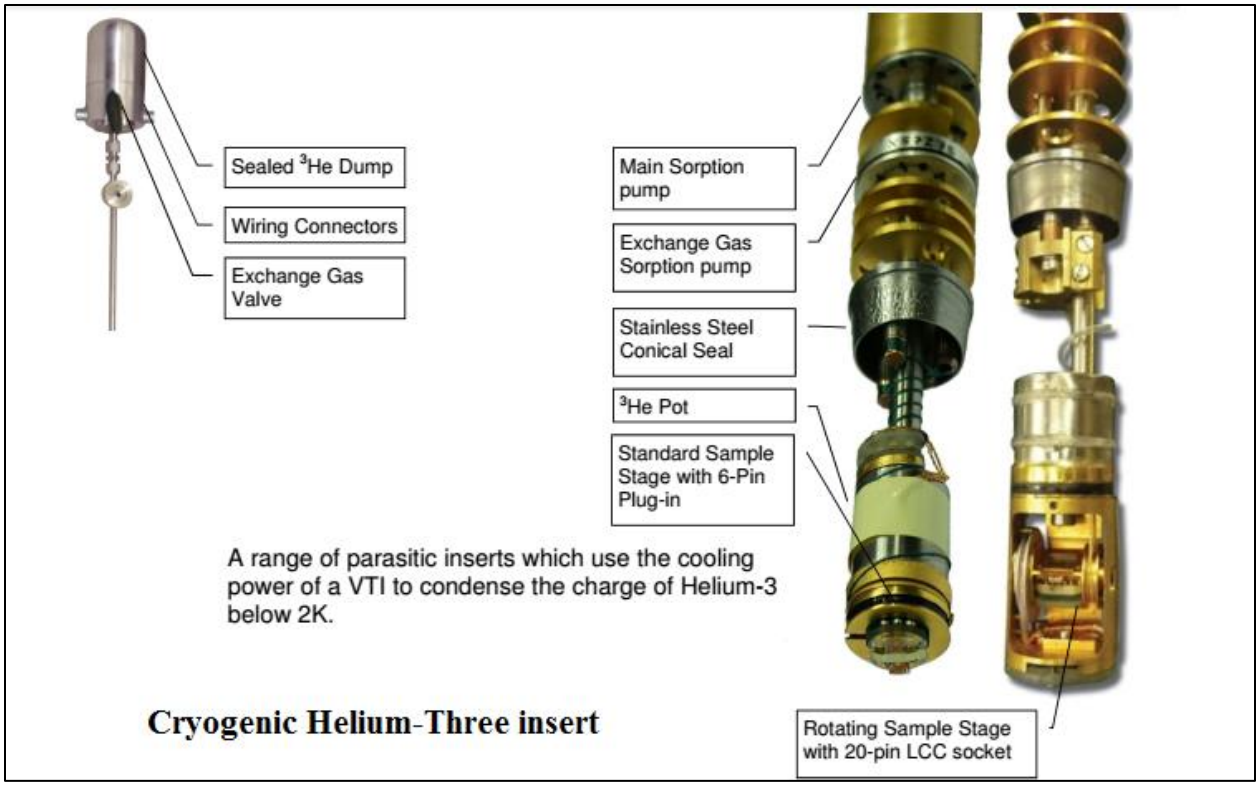


Figure 3.3: Parasitic 3He Insert Probe

The Helium-Three insert is top-loaded into the VTI. It uses a working volume of liquid 3He of 1.5cc and is able to maintain a temperature of 285mK for up to 24 hours. The standard insert features a gold-plated copper sample mounting surface of 16mm diameter. An adaptor is available to allow the use of standard resistivity sample mounts. Once the CFMS is set-up properly the stability and optimisation of the measurement depends on the operation of the Helium-3 probe.

Preparation, insertion and removal of the Helium-3 Probe

Prepare the Helium-3 probe for insertion into the VTI using the airlock and gate valve as follows:

- Attach sample platform on the horseshoe socket above the Helium-3 pot.
- Clean both surfaces of the conical seal and apply a light coating of vacuum grease to isolate the socket. Push surfaces together gently and leave the green valve on the pot open.

- Connect all three temperature control channels and ensure that all sensors read approximately room temperature.

Insert the probe as follows:

- Attach probe with sliding seal to the airlock on top of the cryostat using the large clamp and O-ring.
- Pump out the airlock.
- Set Lakeshore 335 channel B to 330K to ensure release of water vapour absorbed during sample change.
- Close airlock valve but leave upper valve (sliding seal) open and pumping.
- Open the gate valve and slide the unit gradually into the VTI for optimum performance.
- As soon as the green valve can be reached and the probe is still warm (>100K) and the VTI pressure is <15mbar, close the green valve. This is a very important step which determines whether the system achieves temperatures below 300mK or not.
- Once the probe is in position, the airlock sliding seal valve may be closed and the pump turned off and isolated.

Remove the probe as follows:

- Turn on airlock pump, keep open the green valve and the airlock valve closed.
- Lift the probe gradually as rapid condensation around the probe can impede probe movement.
- When the probe top is above the gate valve and inside the airlock then the gate valve can be closed. Leave the probe at this position until all thermometers read room temperature.

Resistivity Probe

The Resistivity probe shown in **Figure 3.4** is designed to measure Resistance and Hall Effect for solid samples. The measurement platform consists of four functional elements: two sample sockets (for vertical and horizontal sample mounting), a calibrated CERNOX thermometer and a 100Ω auxiliary heater. Each socket has 6 contacts designed to accommodate plug-in sample holders which can hold a 10x5mm sample size. The holders have six gold-plated contact fields which can be connected to through wire bonding(preferred), soldering, silver paint (used in this work) or a suitable contact adhesive. There is a 6-pin Fischer connector at the top of the probe to provide wiring for the heater and thermometers.

The measurement electronics and probe are linked via a breakout box.

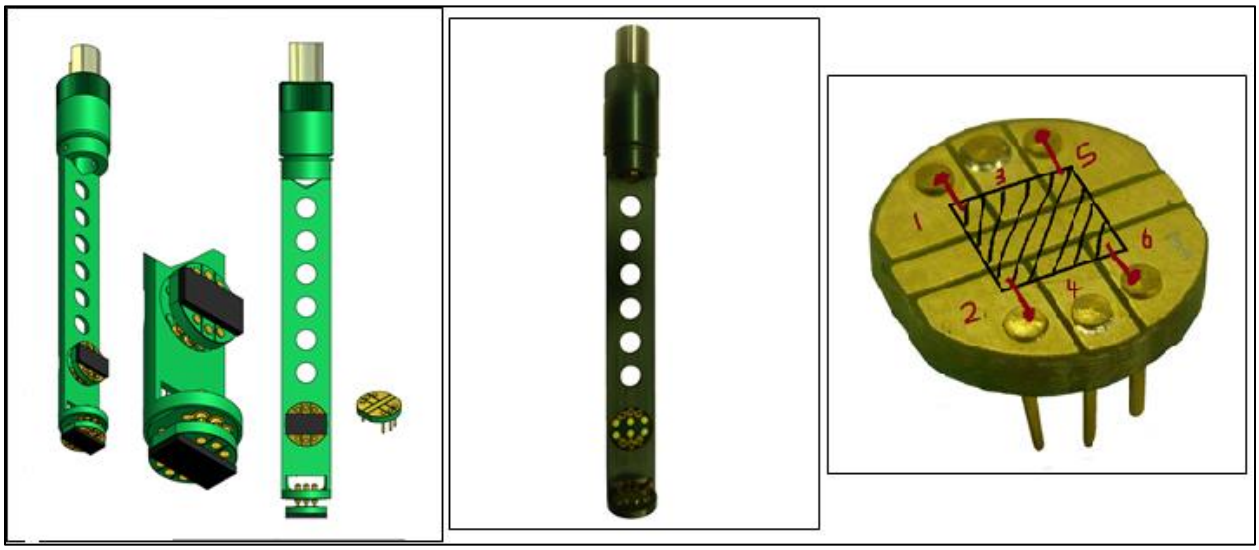


Figure 3.4: Resistivity probe sample platform overview

Once the sample has been mounted and pushed firmly onto the sample platform it's time to load the probe. It is recommended practice to follow the steps below to perform measurements:

- Measure resistance between pin numbers in order to make sure the circuit wiring is correct and the electrical contacts are effective.
- Plug sample platform into back of breakout box and use a digital multimeter to check resistance values between different pins.
- Connect the 6-pin and 12-pin Fischer cables as appropriate to enable electrical connection between sample and measurement electronic system.
- Fit the sliding seal to the top of the airlock and tighten O-ring clamp.
- Grease probe stick so that it passes easily through seal.
- Turn on airlock and open both valves to evacuate both wiper seal and main airlock chamber.
- After about 5 minutes close airlock valve, open gate valve and slowly lower the probe.
- Keep lowering probe until the plastic stopper rests on top of wiper seal. Turn off airlock.
- Decide which pins are used for current and voltage terminals and make connections on the breakout box.
- Finish setup on the measurement software system.

When the experiment is finished evacuate the airlock and close the gate valve so that the probe end can warm up (280K).

Low Resistance - Current Bias

Performing measurement for high fields and low-temperature takes meticulous attention. Measurements are easily susceptible to noise, and the right electrical connections have to be employed in order to obtain accurate results or sometimes even results at all. Carrying out measurements near the superconductor-insulator transition, i.e., the transition between a low resistive, even ”zero” resistance, state and a high resistive state one has to be sensitive to the setup choice. As a rule of thumb, we have to choose the setup where current is sourced and the voltage measured. Consider a superconducting sample being measured in the superconducting phase using a fixed voltage set-up. In this case, it is obvious to see that we may never observe superconductivity since we are likely to be working above the critical current all the time.
Let us summarize all the things to keep in mind when performing high field measurements in superconductivity.

1) Source current and measure voltage.
2) For measurements below 100mK, power should not exceed 1 pW.
3) Be aware of thermal noise (note the voltage variance, bandwidth, and current noise).
4) Accuracy of measuring instruments and filtering.
5) Use wire bonding for sample contacts if available. Silver paint also works but it needs extra care to make effective connections.

Van der Pauw method

A van der Pauw geometry is being used here to make measurements of resistivities in the ohmic range starting from room temperature down to 300mK. Electrical resistivity measurements were performed using a Cryogenic High Field Measurement System. A four terminal configuration for the contacts has been used. In the same setup, magnetoresistance measurements were performed with perpendicular fields up to 12 T. For the determination of sheet resistivity or ρ of a sample the four probe Van der Pauw method is commonly used due to its simplicity.

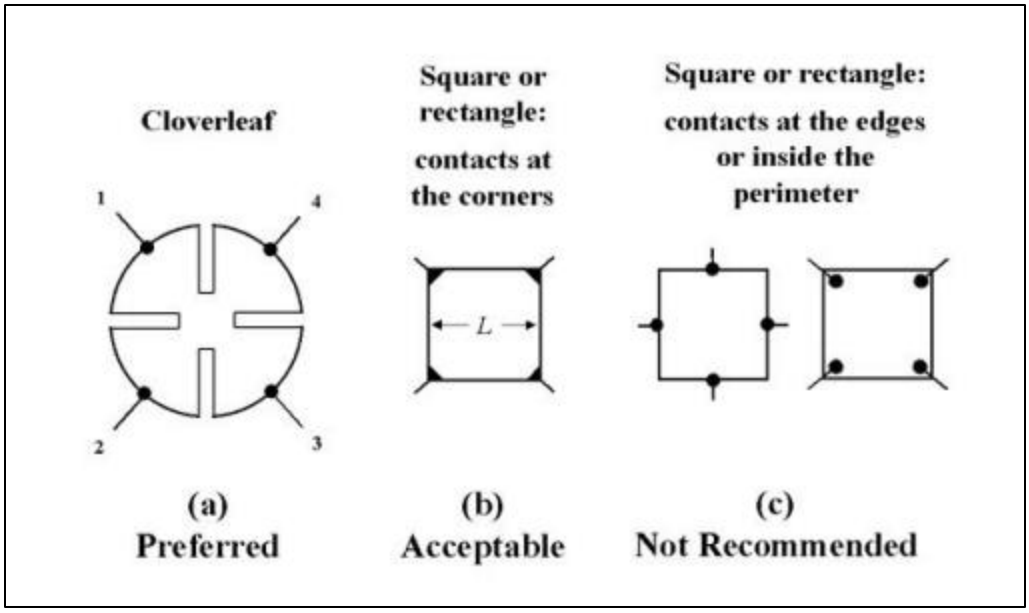


Figure 3.5: Electrical contact configurations for possible Van der Pauw measurements.

The Van der Pauw method is mainly employed when the sample dimensions exceed its thickness. A symmetrical configuration is naturally preferred in order to reduce errors. We make four ohmic contacts on the sample using wire bonding at best or silver paste and conducting glue. The contacts must be on the boundary of the sample and infinitely small as illustrated in **Figure 3.5**.

Measurement definitions:

- Number contacts counter-clockwise from 1 to 4, starting with the top-left corner.
- The current I_{12} is a forward biased DC current (A) that flows from contact 1 to contact 2.
- The voltage V_{34} is a DC voltage (V) across contacts 3 and 4 at zero applied B-field.
- The sheet resistance R_s is measured in ohms (Ω/sq).

In order to determine resistance, current is made to flow along one edge of the sample (for instance, I_{12}) and the voltage across the opposite edge (in this case, V_{34}) is measured. From these two values, a resistance (for this example, $R_{12,34}$) can be found using Ohm's law:

$$R_{12,34} = \frac{V_{34}}{I_{12}} \qquad \textbf{(13)}$$

Further improvements in the accuracy of this measurement can be implemented by measuring $R_{23,41}$, $R_{34,12}$, and $R_{41,23}$.

$$R_{vertical} = \frac{R_{21,34}+R_{34,12}+R_{21,43}+R_{43,21}}{4} \quad \textbf{(14)}$$

and

$$R_{horizontal} = \frac{R_{23,41}+R_{41,23}+R_{32,14}+R_{14,32}}{4} \quad \textbf{(15)}$$

Sheet resistivity (Ohm/sq) or ρ is given by (assuming R vertical = R Horizontal)

$$R_S = \frac{\pi R}{ln2} \quad \textbf{(16)}$$

Magnetoresistance

Applying a magnetic field affects the state of the quantum phase in superconducting materials and gives rise to field effects. Resistance changes drastically with the applied magnetic field. We measure the resistance of the sample as a function of the magnetic field in an a.c. setup. For the superconducting regime, a current excitation and voltage response set up is employed. At high temperatures, the voltage and current are exchanged as explained for current biasing.

Scanning electron microscopy

A scanning electron microscope (SEM) is a microscope that uses electron diffraction to produces images of a sample. The electrons are fired on the surface of the material and scatter. A reconciliation of the scattering results gives information about the sample.
An SEM shown in **Figure 3.6** provides data about the topographical features of a sample. The SEM can achieve high resolution images to the nanometer. When a beam of electrons impinges on a material surface a number of things happen: some electrons can pass through, others bounce off the surface while others trigger transitions in the sample resulting in emission of secondary electrons. Secondary electrons carry history about their background and it is this information that is used to generate images. The most common mode for SEM operation is through detection of secondary electrons.



Figure 3.6: The SEM used for the characterization of BDD in the NSTPL at Wits

In a typical SEM, there are two mechanisms of generating electrons; thermionically and through field emission. The most common method is through heating of a tungsten filament. The generated beam is focused and accelerated in order to give it energy that corresponds to short wavelength comparable to the spacing in atoms. The beam is controlled by an electromagnetic field to move about and scan the sample surface during imaging. A section through the SEM is shown in **Figure 3.7**.

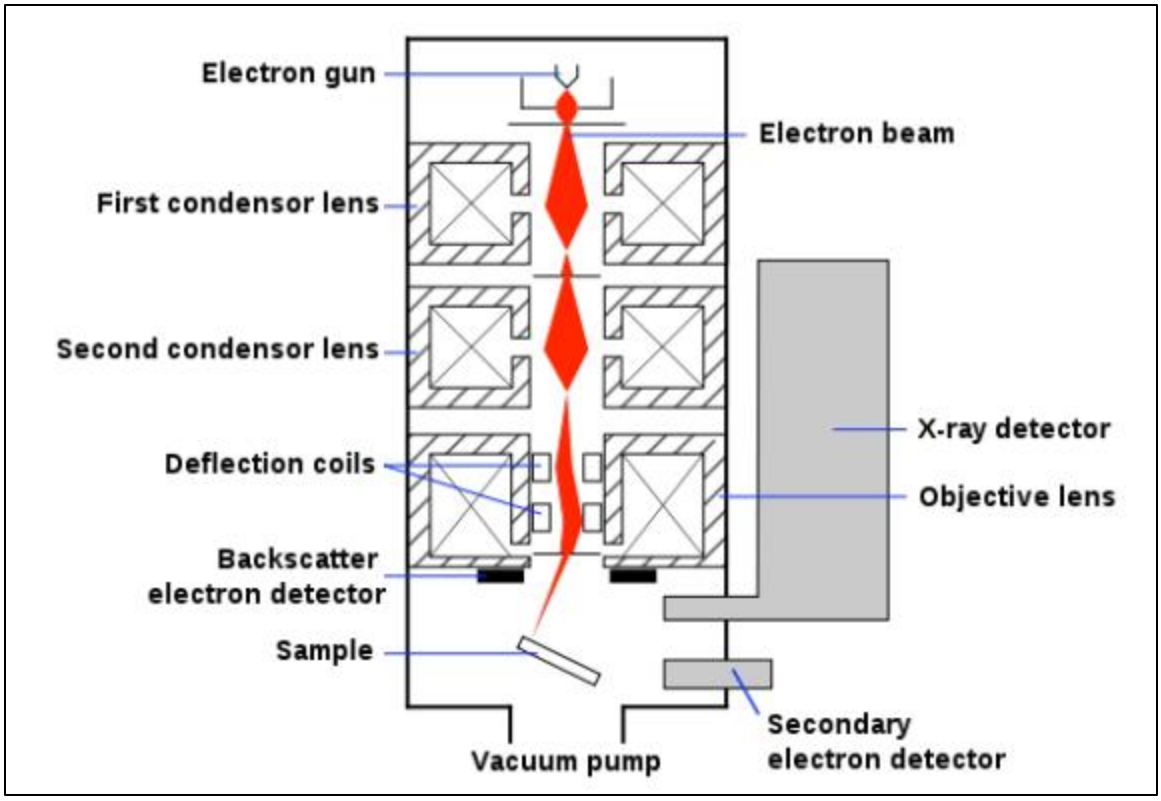


*Figure 3.7: An X-ray diagram of a Scanning electron microscope (SEM) (from **[30]**).*

Chapter 4

Results and Analysis

4.1 Temperature dependent resistance and the Superconductor to Insulator transition:

The superconductor-insulator transition (SIT) in homogeneously disordered films is considered to be a quantum phase transition which can be driven by disorder (D-SIT), magnetic field (B-SIT) and in some reports reduced dimensionality. The underlying mechanism is still under investigation. The essential ingredient regardless of the proposed mechanism generally includes the localization of the superfluid condensate (due to the applied field or some intrinsic disorder) which leads to an insulating state that is far larger in value than the normal state resistance. In the case of the B-SIT, the concept of duality has been invoked, where Cooper pairs are localized, and flux lines that penetrate through the film condense into a macroscopic quantum state. In this scenario, the cooper pairs themselves can contribute to topological charge defect points which can lead to the observation of a dual BKT effect called the charge-BKT effect. This is analogous to the usual 2D superconductor where Cooper pairs are condensed into a superfluid, and stray vortices contribute to finite resistance. When vortices move about they dissipate and creates resistance. This effect has been extensively studied in Josephson junction arrays where resistive insulating states can be observed when tuning the charging to Josephson energy ratio. In the resistive state, the charging energy exceeds the Josephson energy, and the array has a characteristic resistive behavior.

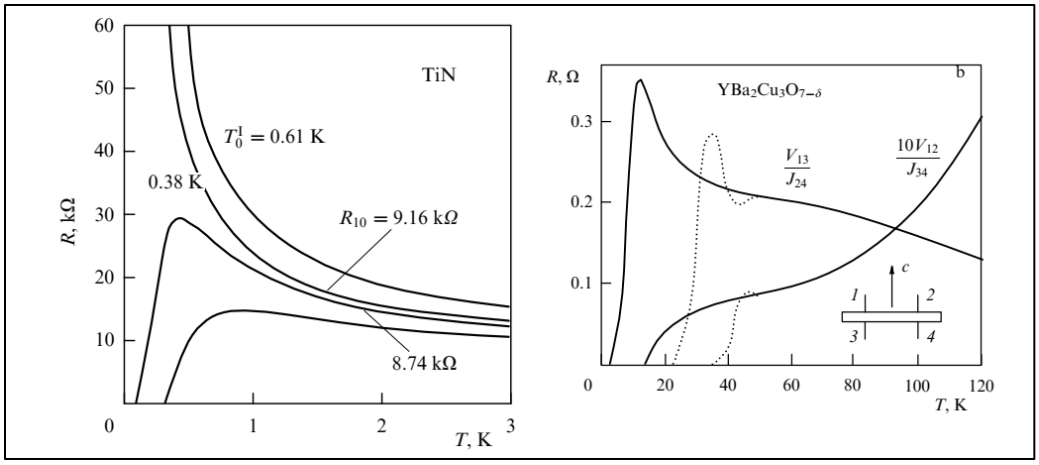


Figure 4.1: a) The SIT in thin films of the superconductor TiN showing the superconducting to insulating phase transition.

Our results exhibit a similar behaviour to TiN thin films shown in **Figure 4.1** at 1.2K indicating a switch from superconductivity to insulating state. This effect increases with reduction in current. Therefore there is a critical value for current beyond which insulation does not occur. High current values are suggested to generate heat which works against the insulating mechanism.

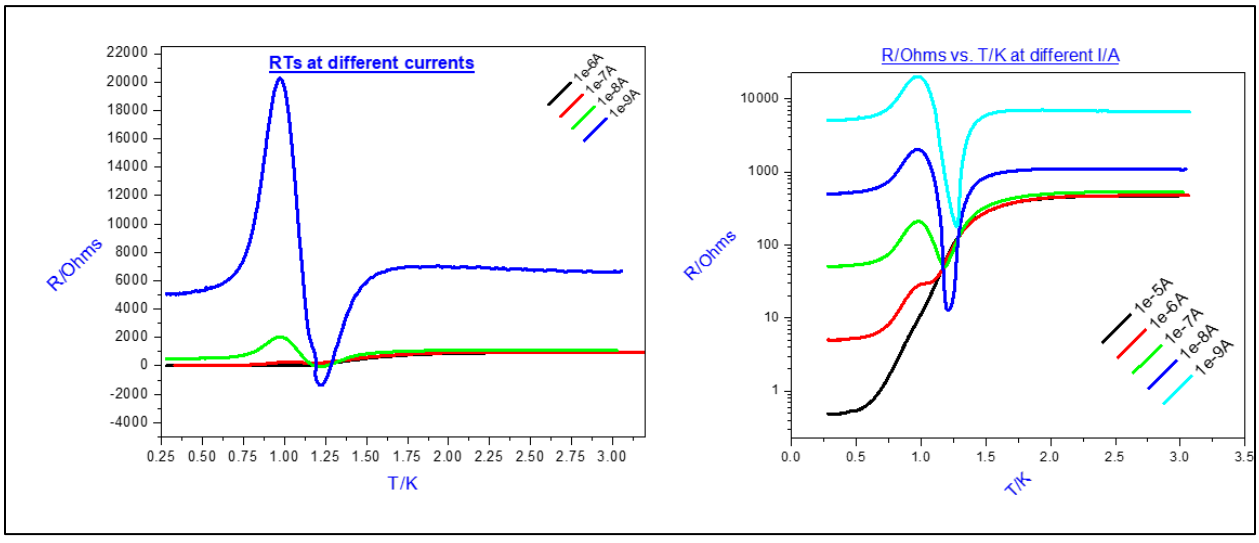


Figure 4.2: The boron doped diamond exhibits a pronounced resistive peak at temperatures below the superconductivity transition onset. This Bosonic peak can be greatly tuned by changing the measurement bias in a nonlinear way. Also observed are resistance saturations after passing through the resistive phase.

Similar to the analysis made for current, strong magnetic fields suppress the SIT. What this confirms is the fact that current or magnetic flux can be used to switch from superconducting state to insulating state. This ability to tune the system if well-developed can be harnessed in quantum hardware. There is a clear analogy between granular superconducting films and fabricated JJ arrays. In the latter case, superconducting grains are separated from each other through grain boundaries. This leads to an extensive network of junctions such as in the case of fabricated arrays. It is not surprising to observe similar physical phenomena in both systems. The superconductor to insulator transition in boron-doped diamond is unique in that transition to an insulating state occurs when a strong magnetic field is applied (i.e., above the critical field ~ 3 T).

A much more exciting transition occurs through varying the measurement bias through the film. As shown in **Figure 4.2**, the boron-doped diamond system exhibits a transition to an insulating phase at the base of the fluctuation regime of the critical transition. This effect is tunable, and the resistive peak can be significantly enhanced by lowering the measurement bias to the nano-ampere regime. This degree of tunability in the resistive phase is thus an essential requirement for device application such as transition edge bolometers and sensor used for space applications.

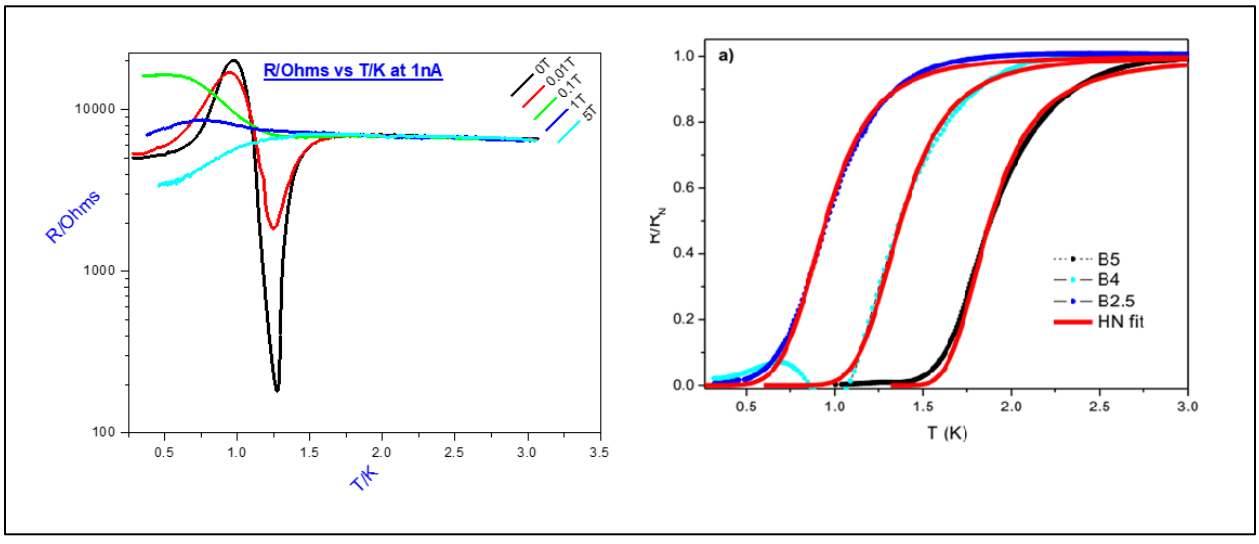


Figure 4.3: (a) B4 resistance-temperature graph at different fields (b) Resistance vs. inverse temperature characterizing the Arrhenius activated region followed by a temperature independent regime at lower temperatures. Another interesting observation is that the resistance peak can be suppressed by applying a magnetic field

Our film shows some unusual features which can be linked to the Bosonic Insulating phase as shown in **Figure 4.3**. This phenomenon is still under debate. Though the mechanism can explain the re-entrant resistive peak phenomenologically, it does not give a physical mechanism for the loss of phase between grains and lacks any theoretical backing. Advanced work done by other peers in our group at Wits University has reported on a possible Charge-Kondo effect as the possible origin to the resistive state. This was verified by a T^2 dependence of the resistive upturn (see **Figure 4.4**):

$$R - R_0 = R_{min}[1 - (\frac{T}{T_K})^2] \qquad \textbf{(17)}$$

Similar resistive peaks have been observed in superconducting Tl doped PbTe. In that system the (Tl) dopant impurity states, in either of the degenerate Tl^{3+} or Tl^{+} valence states, have also been discussed in terms of the Charge-Kondo effect. In addition to the resistive anomalies the Charge-Kondo PbTe(Tl) system shares several other similarities with the boron doped diamond; superconductivity is induced by dopant elements in an insulating host (of the same group on the periodic table), superconductivity onset occurs at comparable critical temperatures and at similar dopant concentrations (i.e. nc > 1020). Thus providing compelling evidence both systems exhibit a charge-Kondo effect.

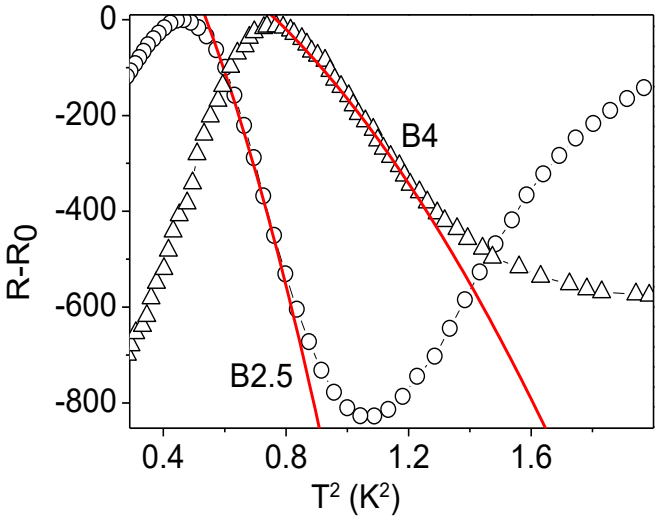


Figure 4.4: The temperature dependent resistance along the re-entrant bosonic insulating peak. This data follows a T^2 dependence as expected for a Kondo effect.

The graphs obtained suggest that HBDD thin films show superconducting fluctuations due to disordered. Vortex BKT physics can also play a role and broaden the temperature transition from normal to zero resistance. Moreover, it is possible that we are witnessing localization effects due to the Aronov-Altshuler effect since the SIT is happening at low temperature. Investigating superconducting properties like quantum phase transitions is an onerous task which takes a lot of experiments because of the variety of mechanisms that express individually or in combination.

4.2 Magnetoresistance

Nanocrystalline samples that exhibit insulating behavior follow an Efros-Shklovskii **[29]** type of temperature-conductivity dependence up to room temperature. Contrast this behaviour with Mott variable range hopping **[30]** which is the dominating mechanism for insulating single crystal diamond close to the metal-insulator transition. There are two factors that influence electronic transport in the metallic samples; the properties of the grains (highly boron doped single crystal diamond) and the inter-granular coupling between the grains. The Josephson coupling between the grains plays a vital role for the superconductivity in this system. It leads to a superconducting transition with global phase coherence at sufficiently low temperatures.

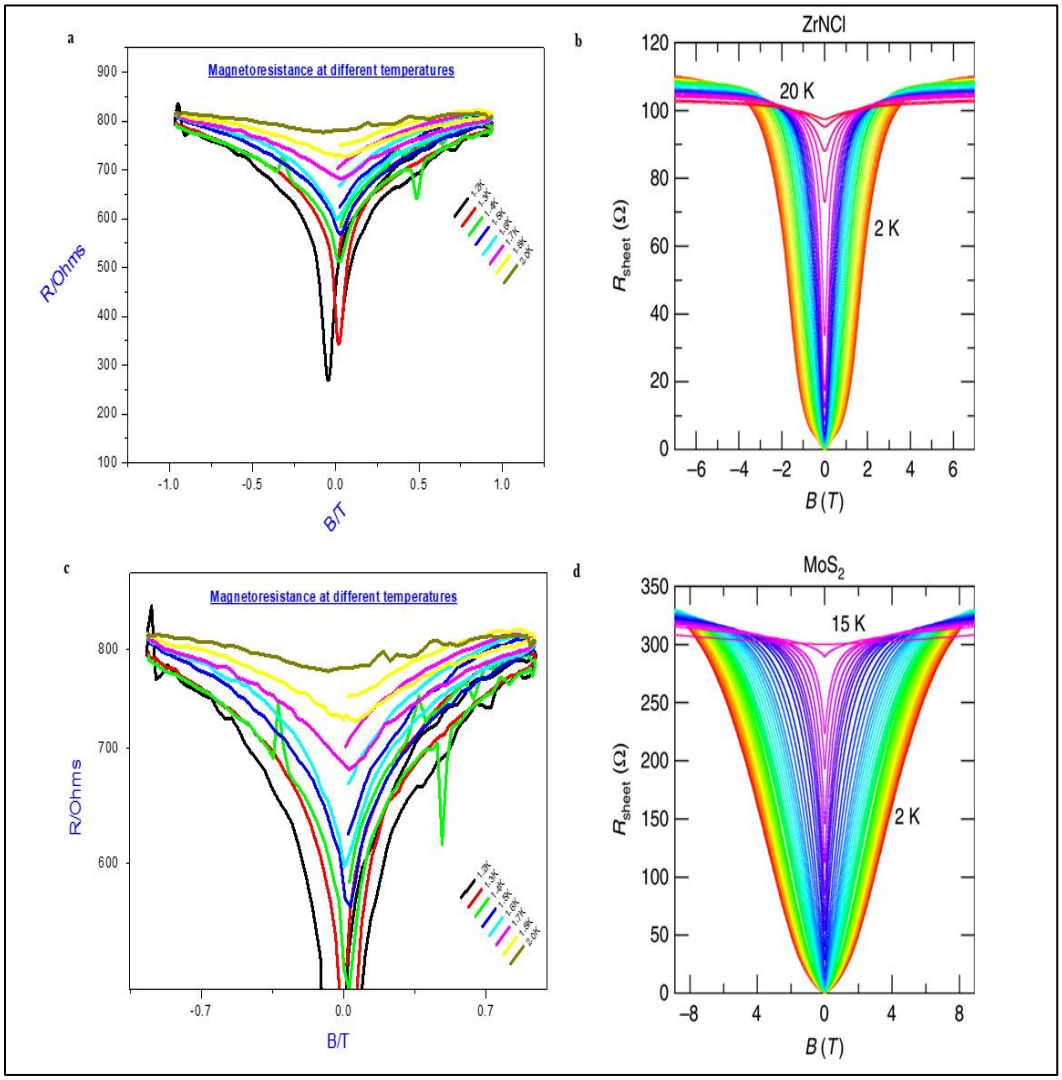


Figure 4.5: The magnetoresistance of the boron doped diamond shows characteristic pair breaking effects. As the field strength is increased, the resistance also increases up to the critical field where the system is no longer in the superconducting state and rather in the normal state. This can be compared to other type2 superconducting systems such as ZrNCl and MoS2 which have a larger characteristic critical field.

A peak in the low-temperature magnetoresistance measurements for samples close to the transition in **Figure 4.5** is explained due to corrections to the conductance according to superconducting fluctuations. In the fluctuation regime (i.e., temperatures around the critical temperature point), there are only a few predicted effects that lead to the slope of the resistance decrease as the system condenses to the superconducting state.

These are due to quantum interference effects of the electrons still in the normal state, the rapid depletion of the density of states of the normal electrons (as they condense to superfluid state) and lastly the Anderson Localization contribution which is related to the dimensionality of the system. These effects can be probed by studies of the magnetoresistance in this regime.

In our studies, we have investigated both the low field and high filed response to the system. As shown in the figure at low fields, the magnetoresistance at low temperatures shows the characteristic pair breaking that is expected for destabilized electrons due to interaction with the filed. This has the characteristic signature of increasing resistance with increasing field until all cooper pairs are broken up and the system is in the normal state. We have observed a variation in the critical field depending on the measurement bias (in agreement with the bosonic insulating phase discussed in the previous section which is more prominent at lower measurement bias). Here we observed that at higher current when the system is more likely to condense to the superfluid phase, the critical magnetic field is larger than at lower current (which favors the Bosonic Insulating peak). This is demonstrated in the figure where we have investigated many isotherms up to intermediate fields and extracted the coherence length as well as the critical field.

The results agree with previous reports, and we find that the critical filed of around 3 T as expected for a type two superconductivity which allows flux penetration instead of a pure Meissner effect. From the fitting to the Landau-Ginzburg theory we find that the experimental data fit the temperature dependence of the critical field well. From the field dependent change in resistance, we also extract the activation energy of flux line induced resistance, this activation energy is related to trapped flux lines which induced vortex states and lead to a finite resistance.

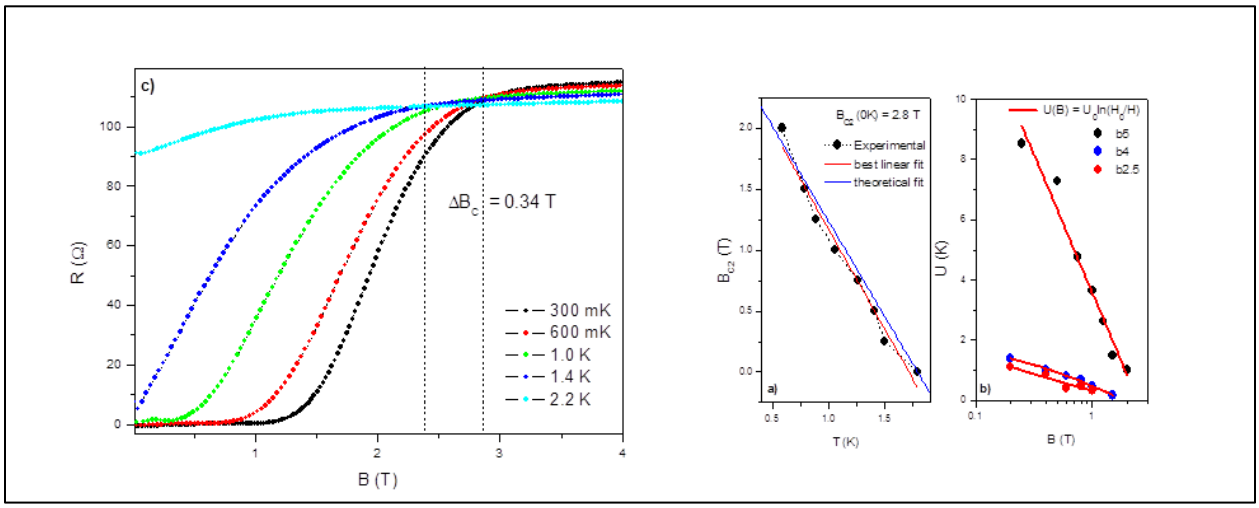


Figure 4.6: From the magnetoresistance data we are able to extract the critical field of the samples, as well as its temperature dependence, the activation energy of flux/vortex states that lead to finite resistance in the fluctuation regime. As can be seen in c) the critical field does exhibit some thermal shift and has a range of approximately 0.34 T.

Figure 4.6 shows that an increase in the magnetic field strength has similar effects as disorder. The relative number of vortex pinning centers grows, and the vortex lattice breaks down converting it into a vortex glass state that causes its melting. When the vortex lattice melts discrete vortices have the freedom to move which leads to dissipation. Thus, the strong magnetic field and strong disorder act on the various types of bosons differently: they suppress the coherent superfluid motion of 2e bosons, but at the same time delocalize vortices.

4.3 DC *I* - *V* measurements

One of the biggest advancements in the field of superconductivity research is the development of the concept of the order parameter. The order parameter generally describes the pairing of the electron of the systems and is based on the fermionic Pauli principal. Thus certain degrees of freedom (spin, parity and orbital angular momentum) must obey certain criteria. Different types of pairing can lead to exotic superconducting states such as the magnetically robust triplet superconducting state or even an odd frequency state.

The theory used to analysis such properties of superconducting systems can easily be tested in through contact measurements whereby point contacts are used to investigate the tunneling spectroscopy and Andreev spectrum of the system. Suppose we have an electron of mass *m* and charge -*e*, with energy *E*, incident upon a junction between a normal metal and a superconducting metal (called a S/N junction), both at temperature $T = 0$ (this makes statistical mechanics unnecessary for the problem). Electric current is not conducted normally inside of a superconductor: the charge carriers are *Cooper pairs* of electrons with opposing spins and momenta. The existing Cooper pairs inside of the superconductor exist at $E = -\Delta$. It takes an energy of 2Δ to break up a Cooper pair, at which point the electrons begin to propagate as *quasiparticles*, where they exist as both electrons and holes at the same time.

If an electron is incident with energy $E < \Delta$, then there is not enough energy to break up a Cooper pair. If there is no mechanism for reflection at the boundary, then the only possible outcome is for a hole to be reflected with energy -*E*, and for a Cooper pair to be formed inside of the superconductor, propagating with energy $E = 0$.

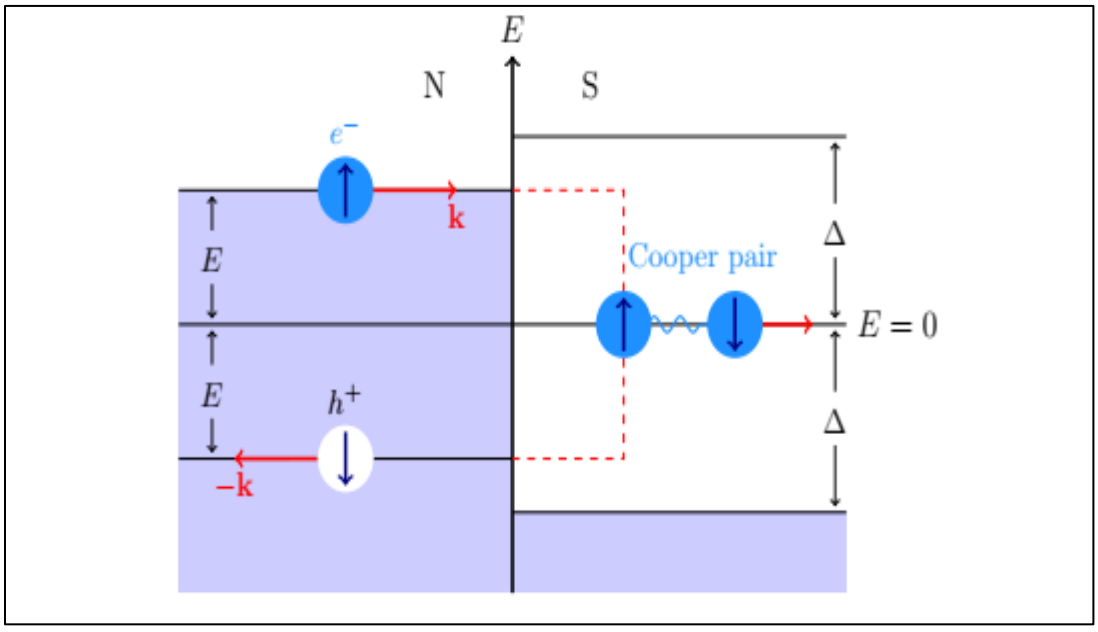


Figure 4.7: An illustration of Andreev reflection

The diagram in **Figure 4.7** is a simplistic picture of Andreev reflection. However, we can use a slightly modified version of Schrodinger's equation to look at this problem in a more formal light.

This work was first done by Blonder, Tinkham and Klapwijk in 1982, and is named BTK theory **[30]** after their work. What follows is a simple mathematical approach. The Bogoliubov de Gennes (BdG) equation describes quasiparticles of electrons and holes in superconductors, analogous to the way Schrodinger equation describes electrons and holes in normal solids. Using the standard two state basis of electron-like and hole-like states, we can describe the wave function as,

$$\psi(x,t) = \begin{bmatrix} f(x,t) \\ g(x,t) \end{bmatrix} \qquad \textbf{(18)}$$

and the BdG equation reads,

$$i\hbar \frac{d\psi(x,t)}{dt} = \begin{pmatrix} H(x)\ \Delta(x) \\ \Delta(x) - H(x) \end{pmatrix} \psi(x,t) \qquad \textbf{(19)}$$

where,

$$H(x) = -\frac{\hbar^2}{2m}\frac{d^2}{dx^2} + V(x) - E_F \qquad \Delta(x) \qquad \textbf{(20)}$$

is the spatially dependent superconducting energy gap (or quasiparticle coupling) and E_F is the Fermi energy. The mathematical structure of the equation implies time reversed dynamics of the holes compared to that of the electron quasiparticles. For the simplest scenario where we have $\Delta(x) = \Delta$ and V(x)=0, we can have an eigensolution of the form, $\psi(x,t) = \begin{bmatrix} u \\ v \end{bmatrix} exp^{i(kx-wt)}$

$$\psi(x,t) = \begin{bmatrix} u \\ v \end{bmatrix} exp^{i(kx-wt)} \qquad \textbf{(21)}$$

which gives the eigenenergy solution,

$$E^2 = (\frac{\hbar^2\, k^2}{2m} - E_F)^2 + \Delta^2\ . \qquad \textbf{(22)}$$

The positive solution of the energy refers to the electron quasiparticles and the negative one to hole quasiparticles. The superconducting energy gap is introduced whenever $\Delta > 0$, and this is typically in the order of 1meV for elemental (low T*c*) superconductors, while E_F is several eV in magnitude.

Another useful quantity is the density of states (DOS) which can be derived from elementary solid state physics, $\rho(k)dk = \frac{V}{(2\pi)^3} 4\pi k^2 dk$ and a simple expression for the DOS ratio between the superconducting state to the normal state can be easily derived.

Assuming equal Fermi energy N and S, $(E_F)_N=(E_F)_S$, and in the limit of small energy range compared to the Fermi energy, we have, $\frac{\rho_S(E)}{\rho_N(E)} = \rho(E) = \frac{E}{\sqrt{E^2-\Delta^2}}$ for $E > \Delta$ and zero otherwise.

The BTK theory seeks to address scattering conditions in junctions that involve superconductors and obtain reflection and transmission probabilities. It assumes a scenario of equal Fermi energy between a normal metal and the superconductor. Also, the superconducting gap Δ(x) is assumed to be independent of the location on the interface. The superconductor-normal metal junction gives rise to proximity effects due to diffusions of some Cooper pairs into the metal, which compromises the effective gap at the superconductor interface. Assuming that there is a sudden change of Δ neglecting interactions that happen within either material, i.e., V (x) = 0, for regions deep inside the conductors and in the vicinity of x → 0 we can model the interface scattering potential such as V (x) = Hδ(x) where H is the strength of the scattering potential. By defining a dimensionless quantity Z which expressed as $Z^2 = \frac{mH^2}{2\hbar^2 E_F}$ often called the barrier strength, representing the strength of the scattering potential $H\delta(x)$. Now we consider those energies less than the gap energy, *i.e.*, $|E| < \Delta$. The incident electrons cannot enter the superconductor as quasiparticles. If $Z = 0$, all electrons are Andreev reflected while for $Z > 0$ some electrons are normally reflected. As Z increases, Andreev reflection becomes less likely (and harder to observe). Any spike in current that can be observed will mostly be the result of tunneling.

An investigation of the tunneling through grain boundary junctions where the symmetries of the Cooper pairs are determined from the scattering events which lead to characteristic structures of the differential conductance provides an alternative to way to quantify effects in granular systems. We conduct IV characteristics measurements on the boron doped diamond films and identify some key features. These measurements are conducted using a four probe technique carried out in a variety of temperature and fields. We thus extensively investigate the change in the conductance spectra around the superconductor to insulator transition. Our spectra in the tunneling conductance have revealed sharp peak structures centered on zero voltage, this has been observed in other superconducting systems that do not have an s-wave parity of the order parameter. The observation here thus indicates that the pairing in superconducting diamond may not be as conventional as previously thought and may require a deeper investigation.

The robust nature of the superconducting phase is also observed by the application of magnetic field. The insulating phase is only observed at fields as high as 3T, a value that mirrors the transition in the temperature dependent resistance.

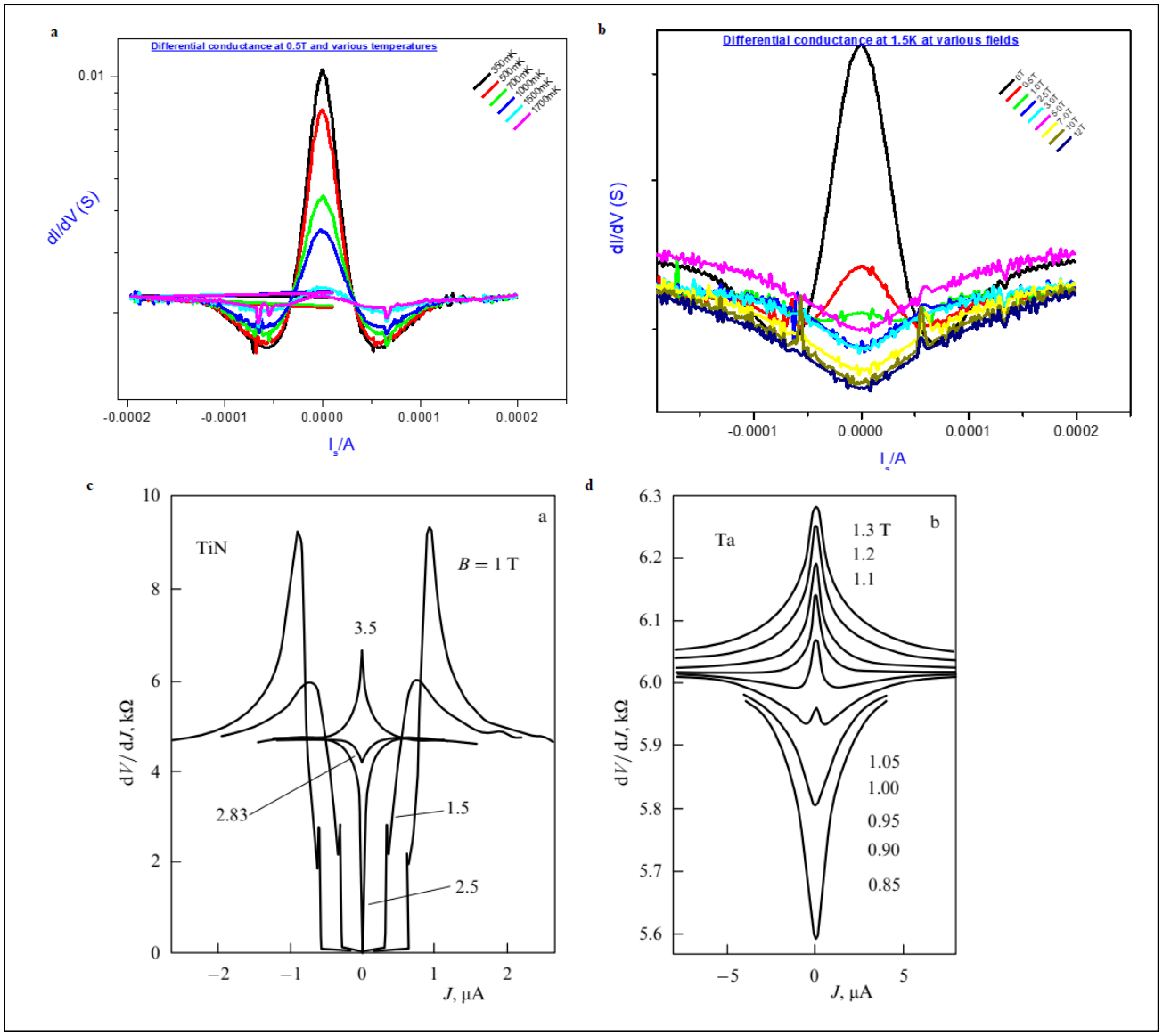


Figure 4.8: A comparison of differential conductance dI/dV and differential resistance dV=dJ of HBDD and TiN films in the vicinity of the superconductor–insulator transition at different fields and temperatures.

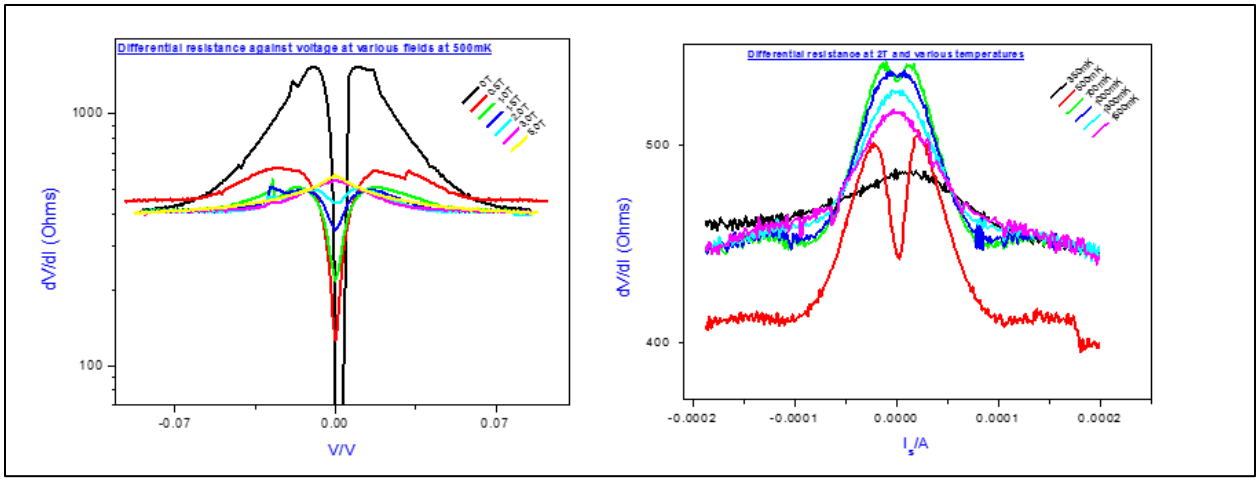


Figure 4.9: IV characteristics can be plotted as either differential conductance (dI/dV) of as differential resistance (dV/dI). As shown above through the application of the magnetic field we are able to tune the system from the superconducting state (valley at zero bias) to a resistive normal state (peak at zero bias). The field strength required to fully drive the system to the normal state corresponds to the same field obtained from temperature resistance measurements.

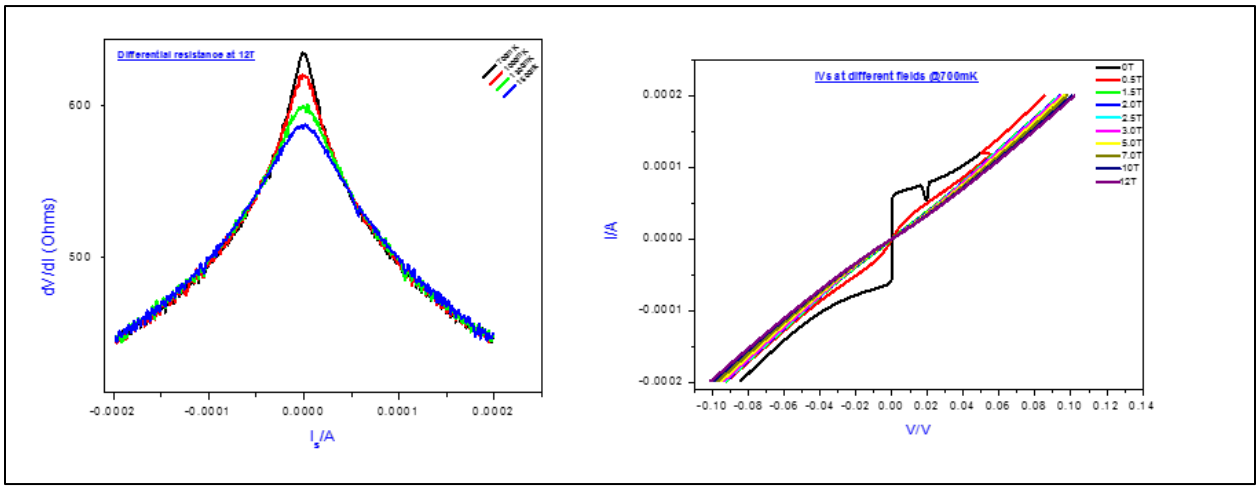


Figure 4.10: (a) At high field (12 T), the system is completely driven to a resistive state, the sharp peak feature can further be tuned by changing the temperature during measurement. Interesting observation is that at high fields, the maximum resistance (peak value), exceeds the normal state resistance, this is a possible indication of the filed induced superconductor o insulator transition where electrons are still bound in pairs but are in a localized state. (b) The IV characteristics that the differential resistance is obtained from, as can be seen here the application of magnetic field breaks the superconducting state, leading to some finite resistance.

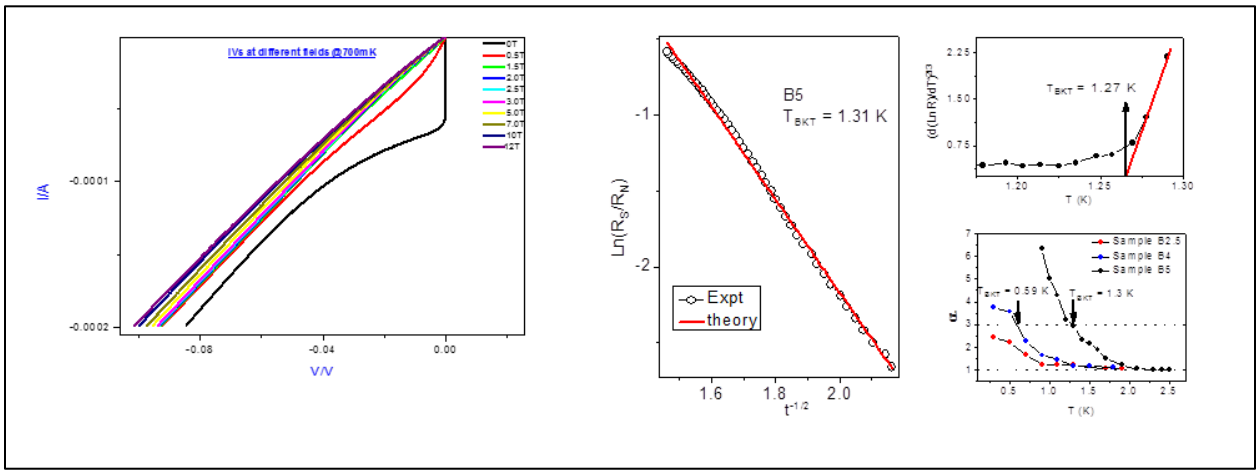


Figure 4.11: (a) The super linear IV characteristics is an indication of a BKT effect at low temperatures. This has been corroborated by scaling analysis of the b,c) temperature dependent resistance as well as the d) exponential dependence of the IV scaling.

As shown in **Figures 4.8** to **4.11**, *I-V* characteristics at different temperatures and field intervals show evidence for the BKT transition (vortex anti-vortex binding). The slopes of the respective curves are used to determine the α parameter (where $V \propto I^{\alpha}$) for the different boron-doped diamond samples at different temperatures and fields. According to the so called Kosterlitz-Thouless criterion the BKT transition temperature can be determined from the plots by determining the temperature at which the parameter α jumps from a value of 1 to 3. This is shown in **Figure 4.11**(d bottom right) where samples B5 and B4 have transition temperatures of T_{BKT} = 1.31 K and 0.59 K as indicated by the dotted line, the larger grain size sample B2.5 does not show this jump in our experimentally accessible temperature range and requires lower temperatures to observe the transition.

Further we see evidence of the BKT transition in the scaling of the resistance temperature data. This is shown in **Figure 4.11 b-c**, where the obtained temperature is of a similar value to that obtained from the IV characteristics, indicating a reasonable consistency between curve fittings. The observation of the BKT effect in this system is quite significant as it is hallmark feature of a 2D quantum system. It signifies the binding of free vortices which allows the system to condense into a completely coherent phase. As mentioned before we believe the observation here can be explained in analogy to the High Tc Cuprates where this transition is also observed.

In those systems the microstructure is quite complex and is compromised by 2D CuO planes separated by an insulating c plane. Thus the 2D physics can occur within the ab-planes. A similar effect must be at play in our system, and can be related to the grain boundary region where vortex and anti-vortex can get trapped (pinned) and lead to finite resistance until reaching the BKT point and binding.

Analysis

In this section, we have investigated the transport properties of the superconducting heavily boron-doped diamond thin films. We observe anomalous transport features that include a re-entrant resistive phase called the bosonic insulating peak as well as resonance zero-bias peak in the differential conductance. As the boron doped diamond is a structurally complex system, consisting of nanocrystalline grains separated by sharp grain boundaries it is not surprising so many interesting features are observed, specifically those related to low dimensionality and a 2D phase. We have attributed the re-entrant bosonic insulating phase to a possible charge-Kondo effect whereby the increase in resistance is a result of resonant scattering from impurities, in this case not of spin centers (as in the spin Kondo effect) but rather degenerate charge scattering points (likely due to the boron acceptor). As this insulating phase shows tunability due to an applied field as well as measurement current this feature may be of interest for quantum and superconducting technologies, particularly in hybrid quantum systems.

We have also investigated the magnetoresistance of this sample and determined a relatively robust nature under an applied field. The critical field is determined to be around 3 T, which is quite high even for a type 2 superconductor. This robustness at high field can also be applied for use in quantum metrology such as magnetometry sensing devices.

Lastly, we have investigated the zero-bias peak in the differential conductance in line with the BTK theory. This essentially allows us to determine symmetry properties of the Cooper pair wave function. Such a pronounced peak is not observed in conventional s-wave superconductors, and thus we expect some exotic pairing mechanism to be at play.

This work is particularly relevant for fundamental studies into unconventional superconducting systems, particularly at lower dimensions like 1D. It allows us to investigate the effects of localization on the superconducting states. More importantly, boron-doped diamond can be further investigated as a platform for novel electronic applications.

Our investigations into quantum criticality and phase transitions are particularly interesting for quantum technology developments like diamond based qubits as well as robust devices for circuit quantum electrodynamics.

Chapter 5

Literature Review

5.1 Quantum Information Theory

Introduction

Quantum mechanics is perhaps unrivalled as the most fascinating scientific discovery of the 20th century. Modern electronic devices that have changed the world of technology from lasers and magnetic resonance imagers (MRIs) to hard drives and liquid crystal displays (LCDs) owe their existence to the application of quantum mechanics **[31-35]**. The current challenge facing the information processing industry is to make more capable devices that are even smaller. Since the current best processors have approximately 14 billion transistors packed on a chip, the only way to keep improving technology is to reduce the transistor to the size of an atom. The laws of quantum mechanics dominate as the size of matter approach nanoscale sizes. Moore's law seems to disintegrate at a quantum level since currently not only the number of qubits matter but also of importance is the quality of the qubits and the amount of error correction that will be required. The expectation is that gate level quantum computers will need substantial amount of error correction so that logical qubits will consist of a number of physical qubits. The industry is toying with an idea of a metric that may be compared to Moore's law called 'quantum volume' recently proposed by IBM.

Matter at atomic level reveals a world wholly unfamiliar to our senses, where atoms can pass through barriers and the act of observing an object can change its state. Experiments demonstrating quantum behavior such as quantized photon energy (photoelectric effect), wave-particle duality (double-slit experiment), and electron spin (Stern-Gerlach experiment) were adequately explained by the end of the 1920s under the formalism of quantum mechanics. Many of the less intuitive predictions of quantum mechanics, such as quantum entanglement and measurement back-action, have remained untested until the past few decades.

Even though our world is, at the microscopic scale, composed of purely quantum objects, these objects interact randomly, or incoherently. When we take a closer look at the macroscopic world all the quantum interactions are ‘smeared out’ and we are left with the familiar classical mechanics.

In order to demonstrate quantum phenomena, we must then control our quantum systems and prevent them from interacting incoherently with the outside world (which includes ourselves as the classical observer). Generally, this has meant studying small objects with minimal interaction to the outside world such as single atoms. Unfortunately, making small, isolated quantum systems sets up a compromise as we as experimentalists reside definitively in the classical world and quantum systems are of little use to us if they cannot respond to our interrogation.

In the early– and mid–1980s researchers (many in John Clarke’s group at UC Berkeley, USA) identified macroscopic quantum coherence in Josephson tunnel junctions **[36]**. These experiments provided evidence for quantum behavior of a 10 μm × 10 μm device with multiple, controlled coupling lines to the outside world, a remarkable result considering the number of atoms present in such a system. This development started a cascade of work with recent experiments realizing quantum systems up the millimeter and even centimeter scales. These larger quantum devices make it much easier to couple quantum information to the outside world and to control where that information does, and equally importantly, does not go (e.g. into the measurement chain instead of leaking to the surrounding bath).

In recent years IBM and other companies have made quantum systems available online. This presents researchers with a rare opportunity to simulate quantum physics phenomena as well as test performance of possible quantum systems **[37]**.

The most important concepts in quantum physics are superposition, entanglement and interference. Superposition gives a quantum qubit possible states that go beyond just digital 1 or 0. The best analogy is a spinning coin where the spin is part of the equation for the state. It is from superposition that we get the exponential growth in the amount of data that can be handled during an active quantum computation.

While 1 qubit contains two pieces of information, 10 qubits contain $2^{10} = 1024$ pieces. On the other hand, entanglement is a strange concept where two qubits, once they have been entangled will have the same synchronized state even when they are miles apart. Both superposition and entanglement are part of the famous thought experiment of Schrödinger's cat. Then, there is interference where the right answer is amplified by the interference of qubit states and wrong answers are cancelled out. Interference is mainly a wave phenomenon which serves a very special role in the development of many qubit quantum computers. The power of a quantum processor is such that with enough high quality, usable qubits, we may be able to simulate and solve suitable complex problems.

There is no simple agreed upon formula that fully describes the power of a quantum processor. All that can be said is that the higher the qubit count, quality level, and connectivity, the better **[38]**. The number of logical qubits is a function of the specific error correction algorithm that is used with the physical qubits. It is not directly related to the qubit quality. However, the lower the qubit quality, the more error correction you may want to put in. This aspect of quality leads us to the concept of gate fidelity **[39]**. In quantum information theory, fidelity is a measure of the "closeness" of two quantum states. It expresses the probability that one state will pass a test to identify as the other. By studying the influence of the shape and power of the control pulses, we hope to find information on whether there are limitations in the gate fidelity. If so we want to know the source of the limitation. Is it mostly related to the external hardware or the intrinsic behavior of the superconducting qubit? Current capabilities of qubits allow us to do simulation to a reasonable enough level of accuracy. Quantum computation is rather more demanding in terms of error correction.

This dissertation details experiments aimed at the characterization of heavily boron doped diamond thin films in cryogenic high field measurement systems and simulate the performance of hybrid quantum devices in application using the IBM online quantum processor. In particular, we aim to prove the effective coupling between nitrogen-vacancy centers in diamond and superconducting flux qubits with a view to support research efforts towards the building of a viable hybrid quantum computer.

Quantum Computation basics

Computation and data storage in all modern systems takes place in so-called 'bits' – digital systems with only two discrete states (e.g. the on and off states of a transistor or north and south pointing magnetic fields which can be extended in quantum cases to up and down pointing of spin). The two states of these bits are referred to (in a mostly arbitrary way) as '0' and '1.' Since classical bits can occupy only one of the two available states at a time, a string of n bits can represent only one element of a 2^n space. Representing the full space, containing 2^n possible arrangements of bits, therefore requires 2^n bits (this assumes no compression which is the case when performing most computations of interest).

DiVincenzo Criteria

In order to have a more meaningful discussion about the architecture of a quantum processor, it is important to consider characteristics the qubit needs to satisfy. In other words, we should seek to answer the question what is it that we want out of a qubit? For any system to be able to perform useful quantum computation utilizing a gate-based architecture it must satisfy strict conditions known as the DiVincenzo **[40]** criteria:

1. The system must be scalable with well-defined qubits.
2. The computer must have the ability to initialize the state of qubits.
3. Qubits must have long decoherence times.
4. The computer must be able to perform a universal set of quantum gates on the qubits.
5. It should be possible to measure the qubits.

Some of these criteria are rather obvious considering any implementation (e.g. criterion 1) while others are more stringent to realise. We should also emphasize again that these are the requirements for universal gate-based quantum computers and other architectures may have lesser requirements. In particular, items **3** and **4** may not be necessary if one implements a quantum annealer such as is done by **D-Wave** (though it remains to be seen whether the **D-Wave** system enjoys a quantum speedup or is even truly quantum).

IBM has built a superconducting quantum processor available online under the IBM Q Experience flagship and we shall cover it in a bit more detail later **[41]** since it is the platform used for this work. While the technology IBM uses for the processor is a superconducting charge qubit, the difference with a superconducting flux qubit relates to the ease of manipulation and difference in vulnerability to various noise sources. For the purposes of this dissertation we will assume these qubits are interchangeable without material impact on the pattern of results. Nevertheless, in practice their merits and demerits differ and should be thoroughly understood.

Qubit Gates

A quantum bit, or qubit for short, is the quantum analogue of the classical bit. Just like a classical bit the qubit has only two discrete states available to it, $|0\rangle$ and $|1\rangle$. In contrast to a classical bit, a quantum bit can occupy simultaneously both the $|0\rangle$ and $|1\rangle$ states. To be precise, the qubit can have complex amplitudes in both the $|0\rangle$ and $|1\rangle$ eigenstates. This idea is expressed in **Figure 5.1.** Because the amplitudes are complex numbers we must express both the relative amplitude and phase of the $|0\rangle$ and $|1\rangle$ state occupations. The well-defined phase between eigenstate occupations is particularly important as it allows an ensemble of n qubits to entangle and represent a system exponentially larger than the number of qubits. Any process which tends to randomize the phase thus lessens the exponential advantage of the quantum system. We describe such processes as decoherence and they present a major challenge in the development of any viable quantum computer. A related process referred to as energy relaxation describes undesired transitions between the $|0\rangle$ and $|1\rangle$ states (in physical realizations of qubits this typically occurs due to energy relaxation from the excited to the ground state, hence the name). This process also limits the efficacy of a quantum system and must be suppressed for a viable quantum computer.

By maximally entangling n qubits (coherently) we can create a quantum system which simultaneously probes all elements of the possible 2^n states contained in the computation space. With appropriate algorithms we can utilize this massive entanglement to parallelize calculations which can only be performed in a serial process using classical computers, thus realizing a

massive quantum speedup as problems scale to larger and larger data sets.

A very good illustration of scaling is the famous wheat and chessboard problem **[42]**. If a chessboard were to have wheat placed upon each square such that one grain was placed on the first square, two on the second, four on the third, and so on (doubling the number of grains on each subsequent square), how many grains of wheat would be on the chessboard at the finish? The total number of grains equals 18,446,744,073,709,551,615, (1,199,000 million metric tons) whilst the global amount of wheat produced in 2016/2017 came to about 755 million metric tons. This illustrates how quickly exponential sequences grow and justify the criticality of the 2^n space to the operation of a quantum processor.

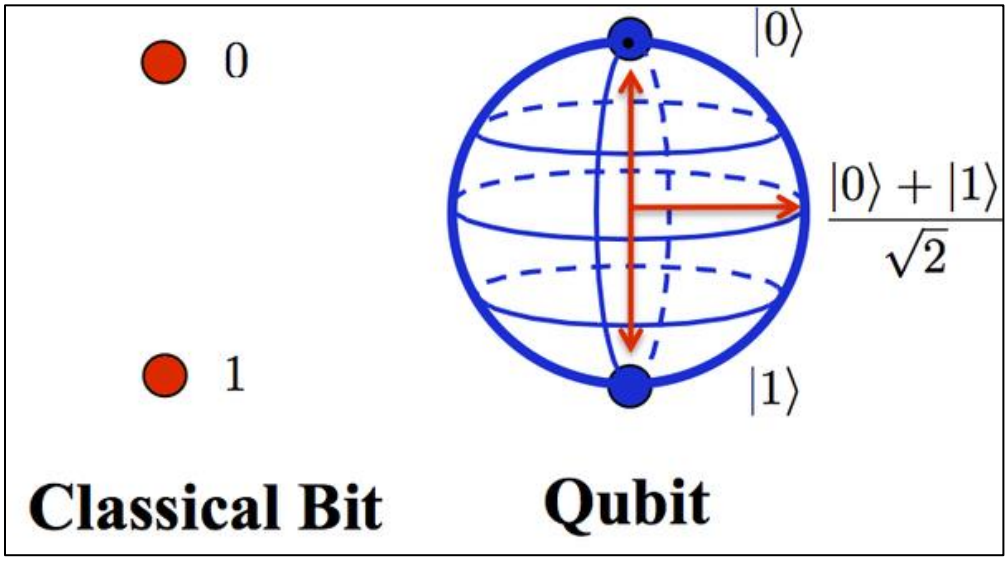


Figure 5.1: Classical bit vs quantum bit 'qubit' [IBM].

A classical bit, the "bit" is realized physically as a level of voltage across a particular element representing the bit in an electrical circuit. This voltage could be across a capacitor or a transistor, etcetera. A quantum bit is realized in a quantum mechanical system with two distinct states, much like a classical bit, but due to the superposition ability of quantum mechanical systems a qubit can exist in a continuum of possibilities between and including 0 and 1 as shown in **Figure 5.2.** This superposition of states is one of the key differences between a classical bit and a quantum bit.

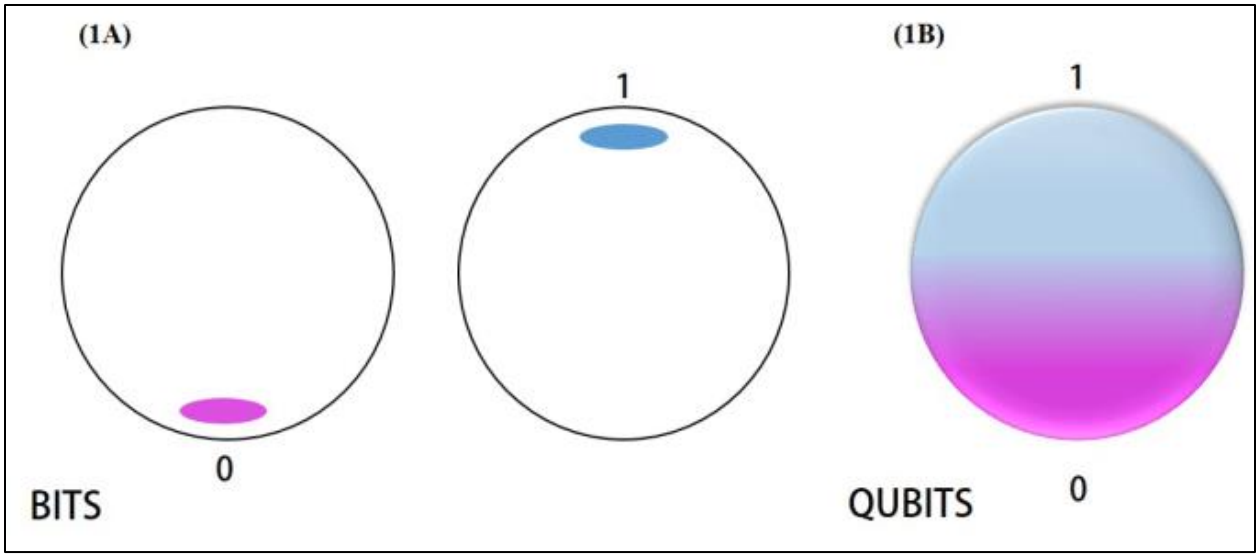


Figure 5.2: Classical bit space and elements in computation space [IBM].

In order to simplify what happens in a quantum circuit, visualization tools are important. A standard one is the Bloch Sphere, as it represents a qubit as a three-dimensional object. One should be cautious however because this tool will not be very helpful to think about multiple qubits, as it fails to demonstrate entanglement. Nevertheless, it remains very useful for understanding single qubits.

The general state of a single qubit is given mathematically as $|\Psi> = \alpha\,|0> + \beta\,|1>$. The first postulate of quantum mechanics tells us that the wave function $|\Psi>$ must be normalizable so we have the constraint that $|\alpha|^2 + |\beta|^2 = 1$.

Using the Bloch sphere context we can write $|\Psi>$ in the most general case in terms of spherical coordinates as

$$|\psi >= e^{i\gamma}(cos\frac{\theta}{2}|0 > +e^{i\emptyset}sin\frac{\theta}{2}|1 >), \qquad \textbf{(23)}$$

where γ, θ, and ∅ are all real numbers. The angles θ and ∅ are defined in **Figure 5.3.**

Typically, the global phase $e^{\,i\gamma}$ is omitted because it has no observable effects on single qubit observables.

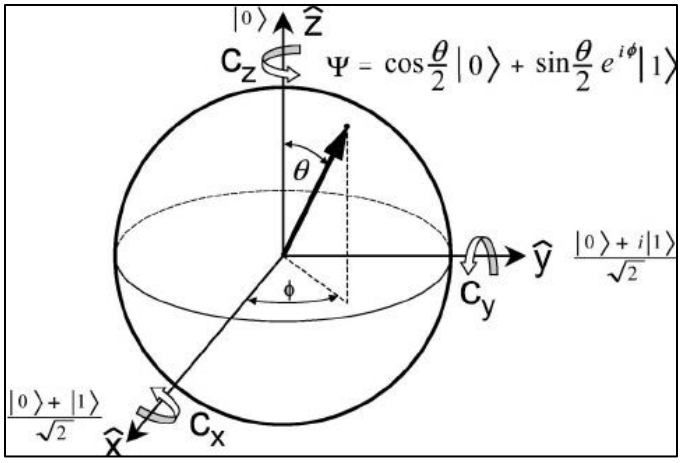


Figure 5.3: Bloch sphere representation of the qubit state control vectors ***[43].***

This yields the relations $\alpha = cos\frac{\theta}{2}$, $\beta = e^{i\emptyset}\sin\frac{\theta}{2}$. The angles θ correspond to rotations of the state vector in the x-z plane while the ∅ rotations correspond to rotations of the state vector in the x-y plane. The equator of the Bloch sphere correlates to an equal superposition of the two basis states |0> and |1> such that $|\alpha|^2 = |\beta|^2 = ½$ and the wave function has the general form $\frac{1}{\sqrt{2}}(|0> + e^{i\emptyset}|1>$. We have defined the system with an angle of θ/2 instead of just θ, this is due to the fact that a quantum mechanical two-level system is actually periodic with 4π rotations. Mathematically, $|\Psi>_{\theta=0} = |\Psi>_{\theta=2\pi} = |\Psi>_{\theta=4\pi}$.

The basis states are the eigenvectors of the chosen reference frame and are ultimately the observable states of that basis. A classical bit can only be in two states, which we can interpret here as a vector which points either up or down. A quantum bit, on the other hand, is a vector that can be in any state on the Bloch sphere.

A classical bit follows the laws of classical mechanics, while a quantum bit follows the laws of quantum mechanics. A classical bit can only exist in either of two non-coexistent logical states, while a quantum bit can exist in an arbitrary superposition of both of these states.

Qubit Manipulation

According to the second DiVincenzo criteria, it is important that we are able to initialize our qubits. In reference to the qubit model as shown by the Bloch sphere, this simply involves putting our qubit vector into any position on that spherical surface. There are 4 unique rotation operations which allow the vector to transform from any state into any other state in the Bloch sphere. These 4 rotations operations are rotations about each Cartesian axis and an identity rotation which does not alter the vector. In fact only two rotation axis are required for universal state creation **[43]**.

The language of quantum mechanics is Linear Algebra and the dynamics are governed by the time dependent Schrodinger equation,

$$i\hbar \frac{d}{dt}|\psi> = \hat{H}|\psi>, \quad \textbf{(24)}$$

The general solution for a time-independent Hamiltonian is,

$$|\psi(t)> = \exp(-\frac{i}{\hbar}\hat{H}t)|\psi_0>, \textbf{(25)}$$

where $|\psi_0>$ is the initial state of the system. Our rotation transformations will occur as a result of our Hamiltonian operator being exponentiated. As it turns out, the Pauli matrices when exponentiated are perfect rotation matrices about the respective axis. Specifically, the Pauli matrices are $\widehat{\sigma_I} = \begin{bmatrix}1 & 0\\ 0 & 1\end{bmatrix}, \widehat{\sigma_X} = \begin{bmatrix}0 & 1\\ 1 & 0\end{bmatrix}, \widehat{\sigma_Y} = \begin{bmatrix}0 & -i\\ i & 0\end{bmatrix}, \widehat{\sigma_Z} = \begin{bmatrix}1 & 0\\ 0 & -1\end{bmatrix}$ but when exponentiated

$R_I(\theta) = e^{-(\frac{i\theta\widehat{\sigma_I})}{2}} = \begin{bmatrix}e^{-i\theta/2} & 0\\ 0 & e^{-i\theta/2}\end{bmatrix}$ which can be repeated for different Pauli's matrices.

The effect of the rotation matrices is to change the values of α and β and effectively rotate our qubit vector around the Bloch Sphere. The key message is that a Hamiltonian with Pauli operators present indicates a physical system allowing for complete single qubit initialization and manipulation. We, therefore, have some kind of guide for what to look for in a physical system for single qubit manipulation.

There are 4 special rotation transformations which we should note as they are common to see in circuit diagrams and quantum science texts. These are the Pauli X, Y and Z gates as well as the Hadamard (H) gate.

The Pauli gates are simply transformation matrices equivalent to the original Pauli matrices. The Pauli X gate is like a classical NOT operation and maps the states |0>→ |1> and |1> → |0>. It corresponds to a π rotation about the X axis on the Bloch sphere. The Pauli Y gate is known as a conjugate bit flip in that it maps the states |0>→ $i|1>$ and |1> → −i|0> and is a π rotation about the Y axis on the Bloch sphere.

The Pauli Z gate is a phase flip gate in that it leaves the |0> state unchanged but |1>→ − |1>. This is also a π rotation about the Z axis on the Bloch sphere. Finally, we have the Hadamard gate which puts the qubit onto the equator of the Bloch sphere in a superposition state. Specifically, |0>→1/$\sqrt{2}$ (|0> + |1>) and |1>→ 1/$\sqrt{2}$ (|0> − |1>). This is equivalent to a π rotation about the (1; 0; 1) axis or the 1/$\sqrt{2}$ ($\vec{x}$+$\vec{z}$) axis.

The Hadamard transformation matrix is $\frac{1}{\sqrt{2}}\begin{bmatrix}1 & 1\\ 1 & -1\end{bmatrix}$. These are all single qubit gates.

This can be developed further in order to establish quantum gates which act on two or more qubits. From a mathematical approach, a quantum gate is viewed simply an operator that acts on a given system of qubits. For single qubit manipulations, these transformations act on a 2-dimensional space. Our Bloch sphere analysis of a general qubit allowed us to find all the operations we needed. However, extending the Bloch sphere to multiple qubits is impossible. Things get complex when we start talking about a larger number of qubits because this expands the dimensionality of the system. The dimension of the system is related to the total number of states realizable.

In the classical sense, the most important of the gates are the NAND and the NOR gates as it can be proven that all possible logic operations can be reduced to a series of either NAND or NOR gates. That is to say that the NAND or the NOR gate is a classical universal gate for classical computation. In a similar fashion, it also turns out that there are and it can be demonstrated that all quantum operations can be handled by a series of single qubit rotations and CNOT gates. The mathematical proofs are beyond the scope of this thesis, but an accepted universal set of quantum gates can be shown to be the Hadamard gate, the RZ(π=4) and the CNOT gate.

Whilst the gates we have covered will not always produce the most efficient set of gates to perform a particular operation, we can rely on them to reproduce any operation with reasonable efficiency.

This takes us to a point where we now have a guide for what to look for in a physical implementation for quantum computing. Specifically, we need to find a system with Pauli operators present which hopefully we can control. We also need a physical implementation for a CNOT gate such that if one qubit is in the excited state it will cause the other qubit to change states **[43].** Finally, implementing a functional Toffoli gate will complete the system so that all quantum and classical logical operations can be accomplished. **Figure 5.4** gives the common quantum gates and corresponding matrices. All of this was found just from considering general quantum information systems arguments and following the DiVincenzo criteria as well as the quantum postulates.

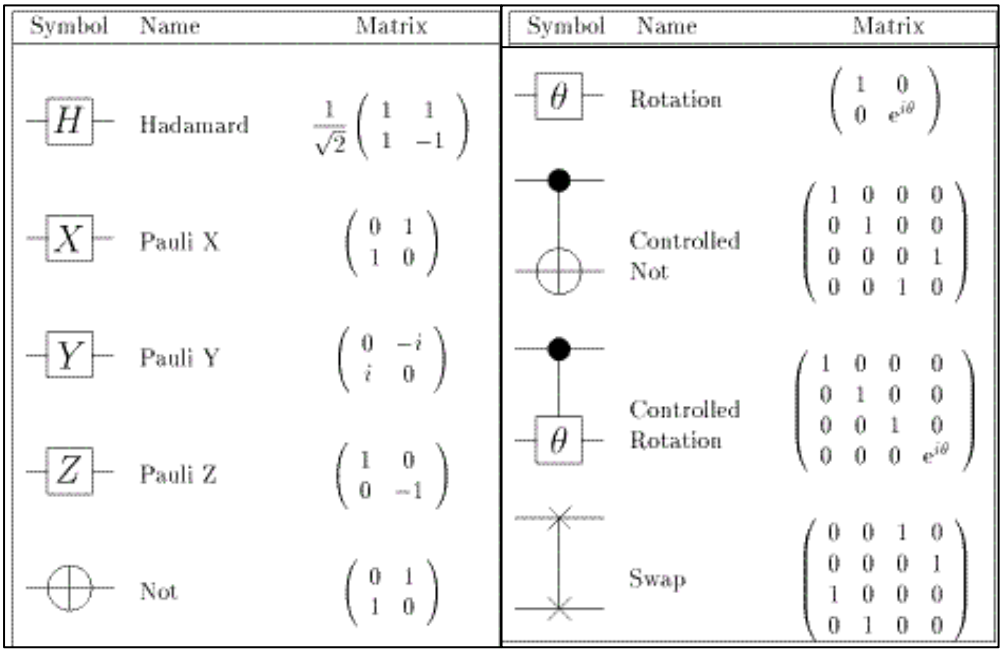


Figure 5.4: Common quantum gates names, symbols and matrices ***[Medium]***

Why quantum computation?

Quantum Computation is the art of manipulating the time evolution of highly complex, entangled quantum states in physical hardware registers for computation and simulation.

The origins of quantum computation are often attributed to Feynman's 1982 discussion of a universal quantum simulator **[44]**. It is from this initial proposal that further theoretical work has been done to develop quantum algorithms, which would work on universal quantum computers and allow for processing speeds that exceed known classical algorithms.
The development of robust quantum algorithms has been somewhat slow, in part due to the challenge of retrieving the answer from our quantum computer. While it would, of course, be possible to perform repeated measurements to map out the full 2^n states in our quantum system this would take exponential time and would negate any time savings from the parallel computation. Effective algorithms must, therefore, find ways to map the 2^n computation states to only n measurement states.

One may ask; why are we so interested in quantum computers and quantum simulators? The basic response is that quantum computers have certain problems they can handle much faster than classical computers. Hard problems are not only a question of whether they take a long time - the question is whether they can be solved at all and efficiently with available resources.

Computational problems are classified as illustrated in **Figure: 5.5.** The class of problems which quantum computation belongs to is called BQP (bounded-error quantum polynomial time). **Figure: 5.5** shows that the BQP only encompasses a rather limited space, basically not solving really hard problems. One may then go further and ask; what is the relationship between problems of practical interest and really hard mathematical problems – is it useful to have a quantum computer, and when is a quantum computer overwhelmed?

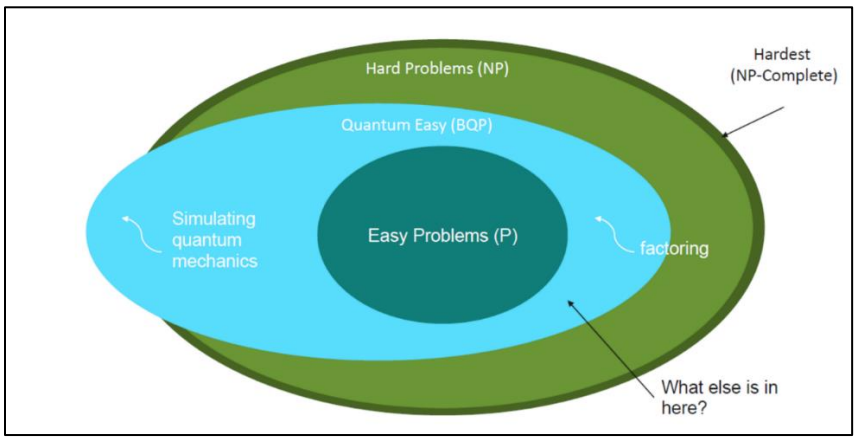


Figure 5.5: Classification of computational problems ***[Lev S. Bishop]***.

The concept of computational complexity comes from Turing Machines which provide digital models computing as follows: deterministic TM (DTM); quantum TM (QTM); classical non-deterministic TM (NTM). Manageable computations are defined by the polynomial time execution. Complexity classes here are grouped into clusters: those solvable with a classical computer (P), those checkable by a classical computer (NP), and those efficiently checkable by a quantum computer (QMA).

The first useful algorithm was Shor's algorithm proposed in 1994 **[45]**. This algorithm utilizes some clever, yet fairly straightforward, number theory manipulation to transform the problem of integer factorization into the problem of finding the period of a function [i.e. find r such that f (x+r) = f (x)]. While integer factorization may not seem important to the layperson it, along with the related discrete logarithm, underlies many modern encryption schemes, the most well-known of which is RSA (Rivest-Shamir-Adleman) public key cryptography **[46]**. It turns out period finding is straightforward using the quantum Fourier transform and with this technique integers can be factored in polylogarithmic time. The fastest known classical algorithm is sub-exponential but scales significantly faster than the polylogarithmic scaling of Shor's algorithm. We note briefly that this is only the fastest known classical algorithm--it is not necessarily the classical limit. Other popular quantum algorithms include Deutsch–Jozsa algorithm, Simon's algorithm and Quantum phase estimation algorithm amongst others.

Despite significant work (and progress) in the field of computational complexity analysis, the relationships between classical complexity classes P (deterministic Turing machine, polynomial time), PSPACE (deterministic Turing machine, polynomial space) and NP (nondeterministic Turing machine, polynomial time), and the quantum complexity class BQP (bounded error quantum computer, polynomial time), are mostly unknown. Thus it is possible (though believed to be unlikely) that quantum computers offer no exponential time or space improvements. This does not rule out sub-exponential improvement, however, as evidenced by Grover's algorithm **[47].** A quantum computer implementing Grover's algorithm can search an unsorted database of size N in time O (sqrt[N]) while the best classical computer requires time O (N) (classically we can do no better than to look at each element until we find the right one, taking on average N=2 time).

More specific quantum architectures such as quantum simulators, quantum annealers, and perhaps adiabatic quantum computers may also provide advantages in addressing specific problems of interest to the scientific community.

Qubit Requirements and Realizations

When discussing quantum computation in the abstract we always talk of prototypical qubits with ideal performance: two-state closed systems with perfect coherence and fully-controlled couplings. When attempting to build a quantum computer, however, such perfect qubits always seem to be in short supply. In reality, we have to make a series of choices about how we're going to make our qubits and these choices will inevitably lead to various challenges and compromises with the ideal.

There are multifarious ways to implement qubits ranging from optical lattices to trapped ions to semiconducting and superconducting circuits to liquid NMR (nuclear magnetic resonance) and even nitrogen-vacancy centers in diamonds. For each technique there are advantages and drawbacks – coupling and readout is difficult for optical lattices and trapped ions while scalability is an issue for NMR-based systems, but all of these techniques have only small decoherence **[48]**.

In this dissertation, we will focus on superconducting flux qubits and spin qubits based on NV^- centers in diamond. Looking beyond the more recent 3D superconducting qubit architectures, the more traditional 2D superconducting (and semiconducting) architectures are highly attractive when addressing the first DiVincenzo criterion because they build on the well-established techniques in micro- and nanofabrication technology developed by the semiconductor industry. Relevant to 2D superconductivity we characterize heavily boron doped diamond thin films to probe for quantum phase transitions (QPTs). Addressing the second criterion is straightforward with access to a dilution refrigerator as typical qubit energies are on the scale of ≈ 250 mK so cooling the entire system to 10-15 mK allows proper ground-state preparation (this ignores the challenges of properly thermalizing qubits at 10-15 mK but rest assured it is possible, at least to the extent required for the superconducting qubits of today).

Requirements four and five are manageable with superconducting qubits where coupling strengths are far larger than in many competing approaches, though this should not undermine the extraordinary effort past and present which has made this possible.
The drawback of this larger environmental coupling is increased decoherence (both T_1 and T_2 processes). Only a few years ago the entire superconducting qubit field fell short of even the most liberal requirements for decoherence.

Recent work, some presented in this thesis, other available in **[49-50]**, has demonstrated superconducting qubits on the threshold of the more forgiving fault-tolerant quantum computation schemes. Before moving to a brief review of superconductivity we wish to point out that the DiVincenzo criteria must all be satisfied together and that as systems scale requirements **2–5** scale as well. Thus devices which may seem to meet the criteria in a **1** or **2** qubit system must continue to improve as systems are scaled up to useful sizes.

5.2 Quantum Information Processing

Quantum information processing is a broad field encompassing all things related to computation, communication, storage, encryption, etc. which are based on the laws of quantum mechanics.
It also tries to formulate procedures and suggest experiments to better understand basic properties of quantum systems and develop intuition for the predictions of quantum mechanics through experiments. The concept of what makes up a computation has been a subject of continuing debate ever since the times of Leibniz, Babbage, and Turing. Technology has also continuously progressed, giving new impetus to efforts in developing quantum processors and simulators. Recently, quantum physics has taken center stage as a powerful way to harness the laws of nature to solve certain problems. Various professionals from the fields of Physics, Computer Science, Mathematics, Engineering, and Information Theory are coming together in order to cope with the demands of this new and promising field.

While, initially theoretical work was all that could progress, current developments in technology supported by stretched classical processors compels researchers to implement basic ideas and concepts from quantum information in specific quantum physical systems.

Major triggers for the upswing in momentum we currently witness in the field of quantum information technology are the discovery of fast quantum algorithms and the identification of concrete physical systems in which a quantum computer could be realized. Meanwhile, a broad spectrum of research activities is happening, ranging from the study of fundamental concepts such as quantum entanglement, to novel applications such as quantum simulators, and with significant spin-off also to other fields of research**.** The following list reviews the main current areas of quantum information theory.

Quantum algorithms & complexity

Quantum processors are very useful in implementing quantum algorithms **[52]**. We are only aware of a few examples up to date, such as Shor's factoring algorithm, but scientists are working on new techniques and protocols. The ability to use a quantum system to perform simulation is very crucial in quantum information theory research. There are a variety of models & architectures for quantum systems available online from a variety of big and small players like Rigetti, Alibaba, IBM, D-Wave among others. These players are provoking renewed interest in science and engineering. Quantum algorithms are being developed and tested and new physical implementations are being considered.

Topological approaches

Topological methods are one of many pathways being considered as the world attempts to build a universal and scalable quantum processor **[51]**. Their main attraction is based on their intrinsic fault-tolerant properties that make active error detection and recovery unnecessary. However, their drawback is that they have longer operation times, such that there is still so much more work to be done to identify the available schemes that are well suited for quantum computation. Companies like Microsoft are supporting research efforts in this space.

Quantum simulations

Developments in the field of quantum technology suggest that quantum simulators are becoming the first short-term application of quantum computers. The benefit of quantum simulators stems from the fact that they offer a platform to test thoughts and ideas involving quantum mechanics which their classical peers struggle to handle; and they can deliver on this with modest hardware capabilities. In order to build a useful quantum processor more stringent requirements have to be met. There are a variety of problems where simulators can be employed immediately like in chemical simulation, drug discovery, artificial intelligence, process optimisation, high energy physics and condensed matter physics **[52]**. Our work here is made possible by the availability of a quantum simulator from IBM.

Quantum error correction & purification

Quantum materials provide the environment where qubits, the elemental unit of quantum information processing, are defined and live. Therefore, quantum materials are the basis of a quantum computer. To have a working quantum computer you need to couple together many qubits, while maintaining their long coherence time **[53-56]**. These demands are often in conflict. Qubits that are hard to couple together have long coherence time because they tend to achieve adequate levels of isolation. On the other hand, systems that are easy to couple together tend to decohere quickly, because they can be perturbed easily by the environment. The precision of the qubit materials is of major importance in order to solve these two challenging requirements.

From the foregoing we can see that though it has incredible computational capabilities the quantum computer will be unreliable due to disturbances and errors. There exist methods to preserve quantum states from unintended perturbations. New methods are being developed continuously until a scalable quantum computer that operates reliably is ready. One of the most commonly used measures of quantum gate efficiency is Randomized Benchmarking (RB). The figure of merit here is fidelity.

Multi-partite entanglement & applications

In order to build a universal scalable quantum computer it should be possible to achieve multi-particle entanglement. The ability to achieve that will have a profound impact on the ability to implement novel protocols in quantum information processing. Multipartite entangled states represent keys resources, both for quantum computers and for novel communication schemes with several users such as quantum-secret sharing, quantum voting, etc. **[57]**. Alternatively one can consider multi-partite fingerprinting schemes that would allow for the determination of whether or not a number of databases are identical with very little resources. Further, solid state lattice platforms can prove useful in building hybrid quantum systems.

Quantum Communication

For any system to deliver value it has to be scalable. The ability to move quantum data from one place to another within the local system as well as with other remote systems is called quantum communication. At the basic level quantum states encode quantum information: hence quantum communication means the transmission of quantum information as well as the distribution of quantum resources such as entanglement. Quantum Communication covers aspects ranging from elementary physics to practical applications that are relevant to society today. From an application point of view, a major interest has been focused on Quantum Key Distribution (QKD) **[59]**, as this offers a provably secure way to establish a confidential key between distributed partners.

This has the potential to solve long-standing and central security issues in our information based society as well as emerging problems associated with long term secure storage (e.g. for health records and infrastructure) and will be critical for the secure operation of applications involving the Internet of Things (IoT) and cloud networking**.** All communication channels are prone to noise. Noise inevitably destroys entanglement or other quantum properties that are useful for the successful implementation of quantum systems like security.

Fundamental quantum mechanics and decoherence

Like Feynman said when you think you understand quantum physics then it means you don't **[60]**. There are still many aspects to understand in the field of quantum physics which have been hidden by the failure to experiment and simulate. Quantum nonlocality research by Einstein-Podolski-Rosen **[61]** gave birth to this field and it is now understood that it is one of the central aspects of quantum mechanics. In general, quantum information benefits substantially from studying the fundamental aspects of quantum mechanics and, at the same time, it yields new perspectives, raising hopes of gaining a deeper understanding of its very basis. In particular, quantum information theory can provide deeper understanding of dynamics of open quantum systems.

Spin-off to other fields

A very exciting aspect of theoretical work in quantum information theory is the impact that it is beginning to gain on other fields of science. Examples are given by the theory of classical computing, by field theory, thermodynamics, quantum gravity and in particular by condensed matter physics. Many of the questions that are now being asked in this area can only be answered or even formulated correctly because of the many insights and techniques gained in the research in entanglement theory in recent years.

Entanglement

A unique and purely quantum aspect; entanglement demonstrates a strong form of correlations that has no equivalent in classical systems. It is an essential resource in quantum information theory and, at the same time, one of the special features of quantum physics. Further insights in the theory of entanglement will keep on having far reaching impact, and applications will spill over to other areas not only in field of quantum information technology itself, but other areas of physics, such as field theory and condensed matter physics**.** Entanglement is a superposition that extends between two or more particles and remains in force even if the particles are separated by a large distance between them.

This novel aspect can find ready application in classical cryptography where, for perfect secrecy, sender and receiver hold two identical and therefore perfectly correlated code-books whose contents are only known to them. Such secret correlations can remain intact regardless of public discussion or an attempt to create new correlations. Over and above quantum communication, distributed quantum computation and general quantum manipulations benefit greatly from entanglement. Albeit problems in entanglement detection, there are numerical methods that exist and work well in most situations **[62]**. Researchers are still a long way from an adequate understanding of entanglement, which undoubtedly is a crucial resource for quantum information processing. We expect that increased effort towards the classification and quantification of entanglement in multipartite entangled states brings insights in the theory of entanglement.

Superposition

Things are very simple and easy to comprehend in everyday life-for example, they have spatial and temporal exactness. The world of quantum physics on the other hand is controlled by uncertainty and chance. Electrons spinning around the nucleus of an atom cannot be located with certainty both in place and time whilst a photon can travel along two different paths at the same time. Such composite conditions produced from interference are called superpositions. It is only when a measurement is made that the particle collapses into one of the possible alternatives; chance determines which one. The concept of superposition is a general physics concept which also applies to other fields such as energy, electric charge and velocity.

Decoherence

Due to their small size quantum systems are very sensitive to their surroundings. Composite states due to superposition eventually diminish and finally collapse – and their desired quantum characteristics then disappear. This process is called decoherence and is one of the greatest challenges to be faced in quantum technology. The two forms of coherence are relaxation and depolarisation. Relaxation is usually referred to as T_1 and is a measure of how long it takes a system to spontaneously move to ground state; depolarisation also called T_2 which measures how long it takes the system to lose the superposition state.

In building a quantum system we have competing interests: isolating the system from its surroundings to avoid decoherence and the need to be able to manipulate the system.

Squeezed states

More than a decade ago when the field of quantum physics was born, Heisenberg's uncertainty principle arose as one of the leading theories. The principle states that there is a limit to the precision with which the position and velocity of an object can be known at the same time. The same theory applies to other intertwined variables such as frequency and time. The uncertainty normally affects the variables in a way that splits possibilities equally. However, it is possible to manipulate the quantum system so that you can ensure that the uncertainty affects one variable more than the other thereby producing what is called a *squeezed state* **[62]**.

5.3 Superconducting Qubits

The devices described in this thesis are all fabricated with superconductors and operated in their superconducting state. At this point, it is not necessary to give a detailed theoretical background on superconductivity as it suffices to only know the basics. A detailed look at superconductivity has been adequately covered in **Chapter 2**; however, where more advanced concepts arise within this section of the dissertation we will strive to give succinct descriptions of the relevant theory without getting lost in details. What follows is a background of superconducting principles that are required to comprehend the flux qubit.

Superconductivity

A superconducting material has zero resistance when cooled below a certain temperature (about 1K for superconducting aluminum and 1.2K for HBDD thin films).

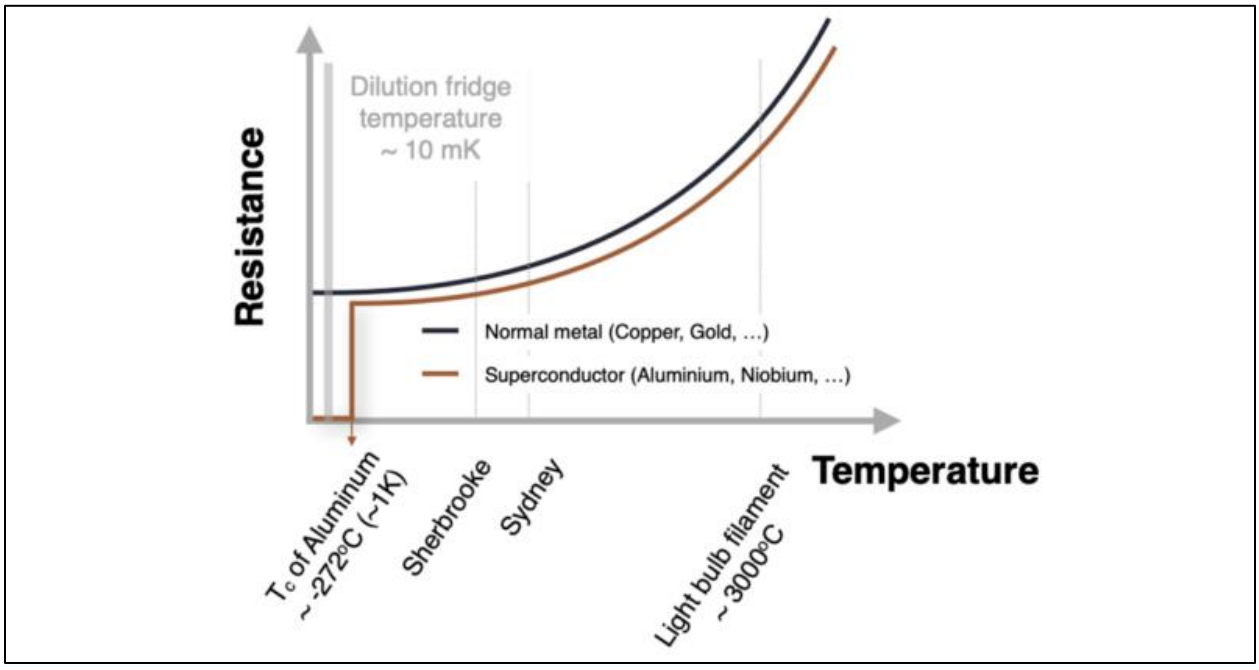


Figure 5.6: A comparison of resistance and temperature for superconductors and normal metals [67].

Collective Wavefunction

When electrons in superconducting materials are cooled below the transition temperature T_C, they form so-called Cooper pairs **[63]**. An effective attractive potential arising from electron-phonon interactions results in electrons with opposite momenta effectively binding into bosons (spin-0 is most common but spin-1 is possible). Since Cooper pairs are bosons they can simultaneously occupy the same state. In superconductors below T_C we find from BCS theory **[67]** that the Cooper pairs form a highly-degenerate condensate which can be effectively modelled by a single wavefunction with amplitude and phase, represented by

$$\psi(r) = [n(r)]^{1/2}.e^{i\theta(r)} \qquad \textbf{(26)}$$

A closer look at ψ(r) shows that n(r) represents the fractional density of Cooper pairs while θ(r) represents the phase of the collective wavefunction (also referred to as the superconducting order parameter). It can be shown that the collective occupation of the Cooper pair ground state opens a gap in the energy spectrum and that small excitations are therefore not allowed in superconductors (excitations must provide an energy equal to or greater than the gap). One consequence of this is a vanishing DC electrical resistance. Static currents can thus flow perpetually in a superconductor once established with no extra energy input required (and without resistance, there is no Joule heating to warm the superconductor above its T_C).

Flux Quantization

Because θ(r) represents the phase of the order parameter it should be a single-valued function (modulo 2π) and thus its value can only change by a multiple of 2π when traversing any closed contour within the superconductor. This can be stated mathematically as

$$\oint \nabla\theta(r).dl = 2\pi m \qquad \textbf{(27)}$$

where m is an integer and the integral is around any closed contour within the superconductor. We know from Ginzburg–Landau theory **[39]** that in the interior of a superconductor (assuming vanishing supercurrent).

$$\hbar\nabla\theta = qA \qquad \textbf{(28)}$$

where A is the magnetic vector potential and q is the charge of a Cooper pair. Substituting this into **Equation (5)** we find (inserting q = −2e and immediately absorbing the minus sign into m)

$$\oint A.dl = \frac{hm}{2e} \qquad \textbf{(29)}$$

Using Stokes' theorem we can rewrite this expression as

$$\iint B.dA = \Phi = m\frac{h}{2e} \qquad \textbf{(30)}$$

where we have substituted B = ∇ × A and rearranged terms on the right hand side. For solid superconductors with no vortices the constant m is zero but for superconducting rings this need not be the case. In fact, from this expression we see that the flux threading a superconducting ring is quantized in integer multiples of the magnetic flux quantum $\Phi_0 = h=2e$ (where a supercurrent is present the magnetic flux is replaced with a fluxoid accounting for the phase drop from the current flow).

Josephson Junctions (JJs)

According to classical electrodynamics if we separate two metal electrodes with an insulating barrier the two electrodes will be completely isolated and no current will flow. Quantum mechanics has a different twist to this same scenario since the electron wavefunction will decay exponentially in the insulating region. If the barrier is thin enough, then, it is possible for the wavefunction to tunnel through or 'leak' across the barrier to the other electrode. In the case of normal metal electrodes, this modifies the resistance from the classically expected value but otherwise leaves the physics unchanged. With superconducting electrodes, however, new physics arises (in part due to the coherent wavefunction of all electrons and in part due to the gap in the excitation spectrum).

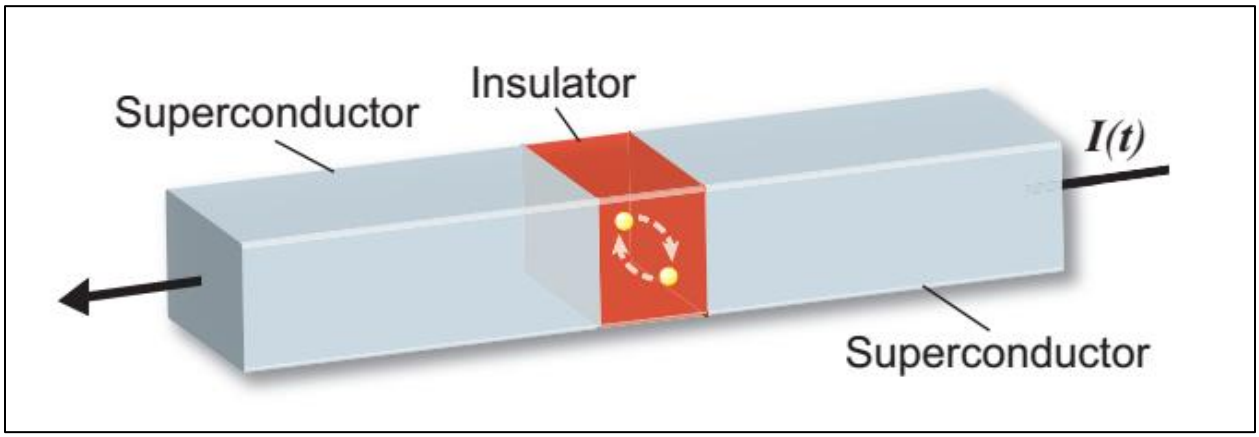


Figure 5.7: Illustration of a Josephson junction ***[68]***.

When two superconductors are impeded by a thin insulator through which Cooper pairs with certain properties can tunnel through that junction is called a Josephson junction. This junction is very important in superconducting qubits since it is a non-linear element and introduces the desired property of anharmonicity.

Josephson Relations

Brian Josephson showed in 1962 that for a thin enough insulating barrier Cooper pairs will tunnel coherently from one electrode, through the insulator, to the second electrode, forming what is named after him the Josephson junction (JJ) **[69]**.

In his seminal paper on Josephson junctions (as a graduate student, no less), Josephson predicted that the following relations would hold:

$$I(t) = I_C \sin[\delta(t)], \qquad \textbf{(31)}$$

$$\text{and } V(t) = \frac{\hbar}{2e}\frac{d\delta(t)}{dt} \qquad \textbf{(32)}$$

Here, $\delta = \theta_2 - \theta_1$ is the difference in phase between the superconducting electrodes. Starting with **Equation (32)** we see that the voltage difference across the junction is directly proportional to the time rate of change of the phase difference across the junction. For a constant phase difference we thus find there is zero voltage across the junction. Looking at **Equation (31)** we see that with a constant phase difference the junction can sustain a static current up to a critical current I_C. When this current is exceeded a voltage develops across the junction and the phase varies in accordance with **(31)**. For the work presented in this thesis we will never exceed the critical current in our junctions and thus no static voltages will develop across the junctions.

Josephson Inductance

To facilitate later discussions it is helpful now to combine **Equations (31)** and **(32)** (the Josephson relations) to aid in modeling junctions embedded in superconducting circuits. By taking the time derivative of **Equation (31)** and inserting the result in **Equation (32)** we find

$$V = \frac{\hbar}{2eI_C\cos(\delta)}\frac{dI}{dt} \qquad \textbf{(33)}$$

The reader will recognize this relation between voltage and current with $\frac{dI}{dt}$ proportional to V, describes an inductor. By defining a Josephson inductance L_J according to the conventional

definition $L_J = \frac{V}{dI/dt} = \frac{\hbar}{2eI_C\cos(\delta)} = \frac{L_{J_0}}{\cos(\delta)}$ **(34)**

one finds $L_J = \frac{\Phi_0}{2\pi I_C\cos(\delta)}$ **(35)**

The 1/ cos δ term reveals that this inductance is nonlinear. It becomes large as $\delta \rightarrow \pi/2$, and is negative for $\pi/2 < \delta < 3\pi/2$. The inductance at zero bias is $L_{J_0} \equiv \frac{\hbar}{2eI_C} = \frac{\Phi_0}{2\pi I_C}$

In this form the nonlinearity versus applied current becomes quite clear. It is also worth pointing out at this time that for currents small on the scale of I_C we can approximate the junction inductance by the linear inductance L_{J_0} which will greatly simplify interpretation of the qubit circuits presented in the next chapter**.**

Josephson Energy

An inductance describes an energy-conserving circuit element. The energy stored in the junction is called the Josephson energy and is accounted for below. **Equations (31)** and **(32)** can be multiplied and integrated to form an energy term. The resultant equation

$U = \int IVdt = -\frac{\Phi_0 I_C}{2\pi}(1 - \cos(\delta)) = -E_J(1 - \cos(\delta))$ where $E_J = \frac{\Phi_0 I_C}{2\pi}$ **(36)**

sets the energy scale E_J for the junction according to the junction critical current. This energy scale will be useful when discussing qubit design in later chapters.

Superconducting Qubits

Earlier in this Chapter I asserted that superconducting qubits are strong candidates for use in a quantum computer because they give a relatively straightforward path to satisfying the DiVincenzo criteria (or at least most of them). What I have not described, however, is how to make a qubit out of a superconductor. We can fabricate superconducting circuits into structures described classically by a capacitance and an inductance and thus superconducting circuits are essentially just parallel LC oscillators.

Quantum LC Oscillator

The Hamiltonian for quantum LC oscillators is well-known and can be expressed using the canonical conjugates Q and Φ, where Q = CV is the electric charge on the capacitor and Φ = LI is a generalized flux variable (for superconducting circuits not all inductance is the classical geometric inductance and thus actual flux may or may not be produced by current flowing

through a superconducting inductance). Using these coordinates we can write the classical Hamiltonian as

$$H = \frac{1}{2}\frac{Q^2}{C} + \frac{1}{2}\frac{\Phi^2}{L} \qquad \textbf{(37)}$$

Noting that the voltage across the capacitor and inductor must be equal we can easily see that Q and Φ satisfy the relations for canonical variables

$$\frac{dH}{dQ} = \frac{Q}{C} = -L\frac{dI}{dt} = -\dot{\Phi} \qquad \textbf{(38)}$$

$$\frac{dH}{d\Phi} = \frac{\Phi}{L} = I = \dot{Q} \qquad \textbf{(39)}$$

This Hamiltonian can be transformed to a quantum version by replacing the canonical variables with their respective operators. It can easily be shown that our canonical operators $\hat{\Phi}$ and $\hat{Q}$ satisfy the commutation relation $[\hat{\Phi} \cdot \hat{Q}] = i\hbar$. The reader will note this is analogous to the position-momentum commutation relation $[\hat{x};\hat{p}\,] = i\hbar$. In fact we can draw a perfect analogy between our LC oscillator and the canonical quantum harmonic oscillator. In this analogy the capacitive term $\frac{Q^2}{2C}$ acts like the kinetic energy term $\frac{p^2}{2m}$ where the mass of our 'phase particle' is its capacitance. The inductive term $\frac{\Phi^2}{2L}$ acts as the potential energy term $\frac{mw^2x^2}{2}$. We can see this explicitly by rewriting the inductive energy term as $\frac{C\omega^2\Phi^2}{2}$ with $\omega = \frac{1}{\sqrt{LC}}$. The reader will note this frequency is none other than the classical LC oscillator resonant frequency. For superconducting qubits this frequency is in the gigahertz (GHz) range and thus benefits from the well-developed microwave technology in telecommunications for control and readout. Since our Hamiltonian has now been transformed into the well-known quantum harmonic oscillator problem we know the solution to our quantum LC oscillator must be the same as the quantum harmonic oscillator **[65]**. In particular we know the eigenenergies of our Hamiltonian must form an equally spaced ladder expressed as $(n + \frac{1}{2})\hbar\omega$.

Harmonic Ladder and Nonlinearity

The harmonic ladder of eigenenergies produced by the simple LC oscillator is unfortunately not suitable for use as a qubit. Any attempt to drive transitions between two levels of the ladder will result in unintended resonant transitions between all energy levels because the energy spacing between neighboring states is always $\hbar\omega$. Thus with a harmonic ladder of energies it is impossible for us to isolate only two levels to use as our qubit states. What is required is an anharmonic potential which yields an uneven spread of energy levels and thus allows us to isolate two states to use as our qubit 0 and 1 states. Fortunately for us Josephson junctions, with their nonlinear inductance, provide an effective means of introducing anharmonic behavior into our LC resonators without introducing loss **[65]**. With the nonlinear Josephson inductance L_J described previously we can fashion nonlinear resonators whose energy spectra will be anharmonic. The specific energy spectrum will depend on the exact nature of the circuit and we leave this discussion for later.

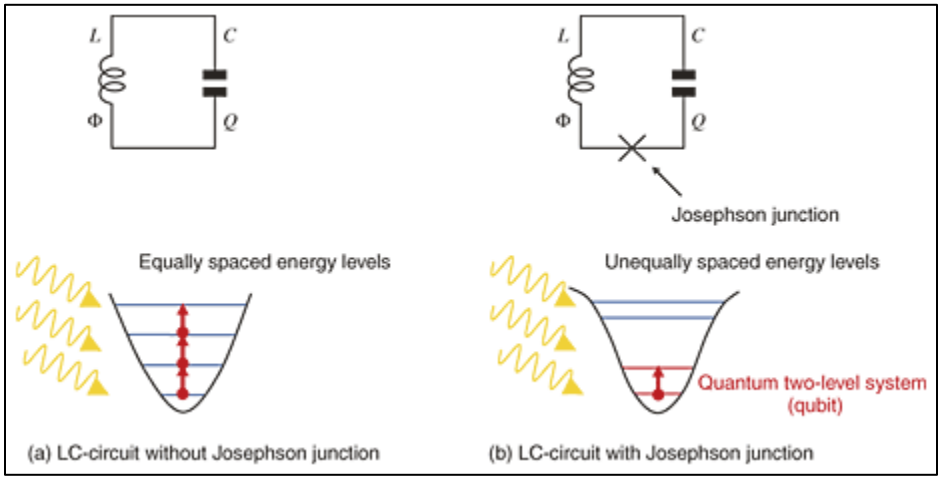


Figure 5.8: A demonstration of how the Josephson junction brings about anharmonicity ***[67].***

Table 5.1 below gives a simple analogy among the different representations of harmonic oscillators in the classical and quantum scenarios.

	Classic Mechanical	Classic Electronic	Quantum Mechanical	Quantum Electronic
Displacement	x	Φ	$\hat{x}$	$\hat{\Phi}$
Flow	p	Q	$\hat{p} = -i\hbar\frac{d}{dx}$	$\hat{Q} = -i\hbar\frac{d}{d\Phi}$
Force Proportionality	m	C	m	C
Restoring Proportionality	k	$\frac{1}{L}$	k	$\frac{1}{L}$
Resonant Frequency	$\omega = \sqrt{\frac{k}{m}}$	$\omega = \frac{1}{\sqrt{LC}}$	$\omega = \sqrt{\frac{k}{m}}$	$\omega = \frac{1}{\sqrt{LC}}$
Commutation Relations	-	-	$[\hat{x}, \hat{p}] = i\hbar$	$\left[\hat{\Phi}, \hat{Q}\right] = i\hbar$

*Table 5.1: Relationship of variables between the mechanical and electronic harmonic oscillator at both classical and quantum mechanical level **[67]**.*

Superconducting Quantum Interference Devices (SQUIDs)

We can also make a tunable nonlinear inductor by combining two Josephson junctions together with a superconducting loop forming a so-called Superconducting Quantum Interference Device (SQUID) **[67]**, shown in **Figure 5.9**. In this case we must revisit the flux quantization argument presented previously to include the contribution of a supercurrent term. This can be accounted for by including the phase drop across the junctions when integrating the phase gradient around the loop as was done in **Equation (29)** (this treatment assumes the geometric inductance of the loop is small and therefore the magnetic flux induced by the supercurrent can be ignored). The result is that the flux quantization condition now becomes,

$$\Phi = m\Phi_0 + \frac{\Phi_0(\delta_2 - \delta_1)}{2\pi}, \qquad \textbf{(40)}$$

where δ_2 and δ_1 are the phase drops across the first and second junction, respectively.
Setting m = 0 we can rewrite this as

$$\Delta\delta = 2\pi\frac{\Phi}{\Phi_0} \qquad \textbf{(41)}$$

This gives us a simple way to relate the phase drop in the loop to the generalized flux threading the loop.

Writing out the current through our SQUID as the sum of the currents across the two junctions (with assumed equal critical currents) we find

$$I_{SQUID}(\Phi) = I_C[\sin(\delta_1) + \sin(\delta_2)] \qquad \textbf{(42)}$$

With some simple trigonometry and substitution of **Equation (41)** into **Equation (42)** one can easily show that the critical current of this device (a SQUID with zero loop inductance) scales with applied flux as $I_{SQUID}(\Phi) = 2I_C \sin\left(\frac{\delta_1+\delta_2}{2}\right)\cos(\frac{\pi\Phi}{\Phi_0})$ **(43)**

To find the actual supercurrent sustained by the SQUID we must maximize this equation with respect to $\delta_1 + \delta_2$ [constrained by **Equation (41)**]. It is straightforward to see the result scales as

$$I_{SQUID}(\Phi) = 2I_C\left|\cos(\frac{\pi\Phi}{\Phi_0})\right| \qquad \textbf{(44)}$$

Here we see the critical current of the SQUID modulates between 0 and 2Ic as the flux is varied over a flux quantum. The inductance of such a device will also tune with the applied flux and thus we have created a flux-tunable nonlinear inductor. While the devices presented in this thesis will not make use of this tunability we will point out how it can be used to add another degree of freedom to our devices.

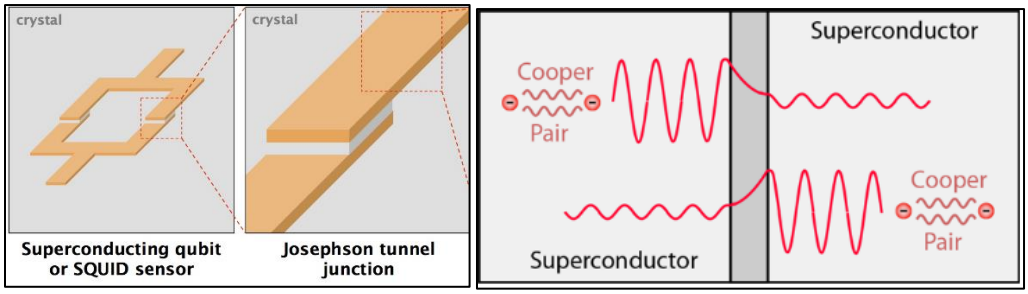


Figure 5.9: A SQUID and a superconductor-insulator-superconductor (SIS) Josephson junction. **[67]**

Intuitive Qubit Behaviors

The Cooper pair box is the simplest device that combines the principles of superconductivity (Josephson junction effect) and tunneling (Coulomb blockade) of Cooper pairs **[38]**. It is illustrated below in **Figure 5.10**.

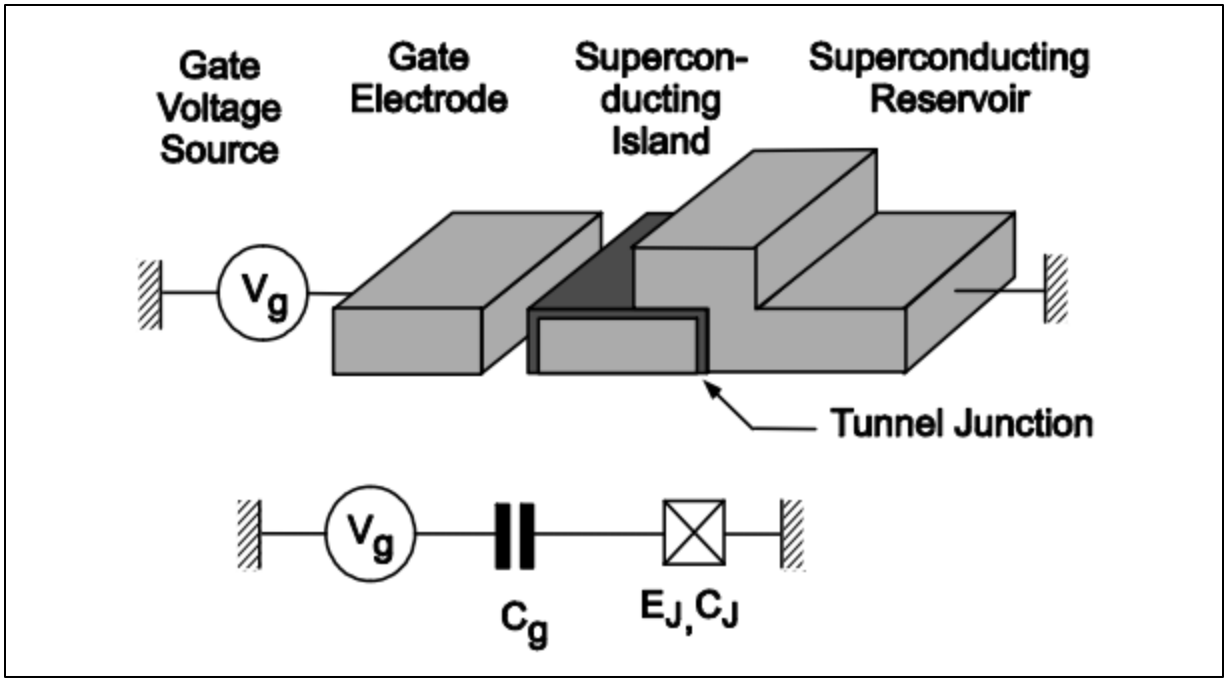


Figure 5.10: The basic Cooper pair box. [Denis Vion]

The basic Cooper pair box (CPB) is driven by a gate electrode coupled to the charge of a small electrode and it is for that reason that it is named 'charge' qubit. The gate voltage performs manipulation of the quantum state of the charge qubit. Nevertheless, reading out the state of a charge qubit with a high efficiency is a difficult task. Moreover, preserving its quantum coherence is a challenge (even at ultra-low temperature) due to its macroscopic character. With the linear capacitance and nonlinear inductance we can being to understand some simple behaviors of superconducting qubits. The capacitance C sets an energy scale according to $E_C = \frac{e^2}{2C}$ while the junction comes with associated energy E_J as described previously. The ratio of these two energies determines whether the eigenstates are defined by states of definite charge or flux (or a combination of the two). In the case of a charge qubit $(\frac{E_J}{E_C} = 1)$, which is simply a superconducting island capacitively coupled to a reservoir of Cooper pairs, eigenstates are represented by the number of Cooper pairs occupying the island. In the case of a flux qubit $(\frac{E_J}{E_C} = 50)$, formed by a superconducting loop interrupted by typically three Josephson junctions, the eigenstates are represented by definite flux (or more correctly fluxoid) states formed by counter-rotating persistent currents in the superconducting loop.

Unsurprisingly, the E_J and E_C values also set the sensitivity to fluctuations in charge/flux inversely in accordance with their associated energy scales. This can easily be understood by recognizing that for example devices with very small E_C (e.g. transmons) are not significantly affected by charge variations and thus the energy bands vs charge are quite flat. Fluctuations in the charge thus have relatively minimal effect on the qubit Larmor frequency ω_{01} (where $\hbar\omega = E_1 - E_0$, the energy difference between the ground and first excited state of the qubit) and therefore have minimal effect on dephasing. A significant drawback is the rather large value of E_J in typical flux qubits (especially when compared to the small value of E_C) which leads to energy levels which are very sensitive to flux. The tradeoff of decreased (increased) noise sensitivity is a corresponding decrease (increase) in anharmonicity. For devices with small anharmonicity control pulses driving the $0 \rightarrow 1$ transition must be carefully timed and shaped to prevent spurious excitations of levels outside the $\{0,1\}$ manifold, while devices with large anharmonicity can be driven with strong, fast pulses without concern for spurious excitation of higher modes.

5.4 The Flux qubit

Why the flux qubit?

An important advantage of the flux qubit, also shared with other superconducting qubits is that a scalable quantum processor is promising due to multi-particle entanglement. The fabrication of solid state based devices is easier than for many other proposals as the technology for realizing such a system is already well-developed (see **Figure 5.11**). Additionally, superconducting structures allow strong coupling between each other and with spin based technologies thus enabling quantum processes on short timescales as well as storage **[69]**. The direct advantage of flux qubits is that they are insensitive to charge noise and can be miniaturized.

Theory of flux qubits

Also called the Josephson persistent current qubit, flux qubits are micrometer-sized loops of superconducting material typically interrupted by three Josephson junctions. In our work we have considered a four junction flux qubit because it becomes more robust against state leakage from the qubit subspace to the third level **[68]**. A careful approach is used to fabricate the junction because the dimensions influence the possibility of having the desired persistent current flow when a suitable magnetic field is applied. The superconducting ring can only be penetrated by an integer number of flux quanta. Currents are generated in the loop to either screen or compensate for a non-integer external flux. A half-integer number of flux quanta, creates quantum superposition of the clockwise and anti-clockwise currents in the two lowest energy eigenstates. This differentiates the relative quantum phase between the composing current-direction states.

Contrarily, higher energy eigenstates correspond to much larger persistent currents that induce an additional flux quantum to the qubit loop. This uneven energy distribution of eigenstates gives the flux qubit its anharmonicity or "qubit non-linearity". This criteria creates the desired two level system between the two lowest eigenstates only. These two eigenstates can now be used as the computational basis for a logical qubit.

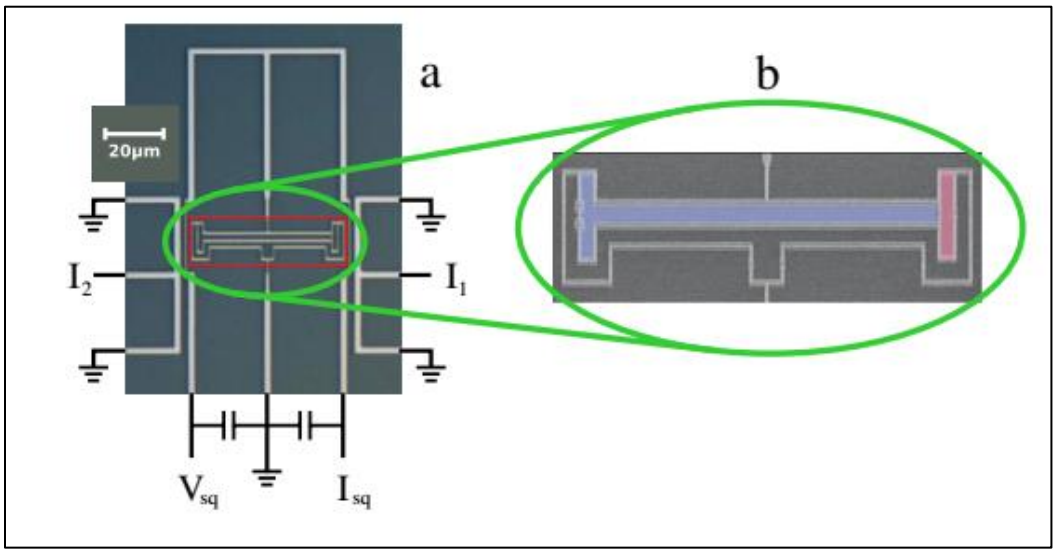


Figure 5.11: Optical micrograph and the circuit scheme of the aluminum flux-qubit (a) and a magnified view of the chip under the red box region (b). ***[68]***

Superconducting flux-qubits, which consist of four Josephson junctions (4JJ) connected by a low inductance superconducting loop, are a promising candidate for constructing quantum processors **[68]**. The only tunable parameter in this system is the magnetic flux (Φ_m) penetrating the loop. At the degeneracy point, namely when $\Phi_m = (n+ 1/2)\Phi_0$ (with integer n), the energy spacing between the ground state and first exited state reaches the minimum value "gap (Δ)". The degeneracy point is optimal because at this point the qubit is decoupled from low frequency flux noise and has maximum coherence time. However, the gap of the flux-qubit is untunable since it is only determined by its intrinsic parameters, e.g. Josephson energy E_J and charge energy E_C of the four Josephson junctions (see **Figure 5.12**). One way to overcome this is to replace the smallest junction of the flux-qubit with a DC-SQUID. By varying the magnetic flux of the DC-SQUID, which is equivalent to changing the parameters of the smallest junction, we can tune the gap of the flux-qubit. This is a significant advantage when coupling to other quantum systems. Our flux-qubit can be tuned into or out of resonance with other quantum systems while keeping the qubit at its optimal work point.

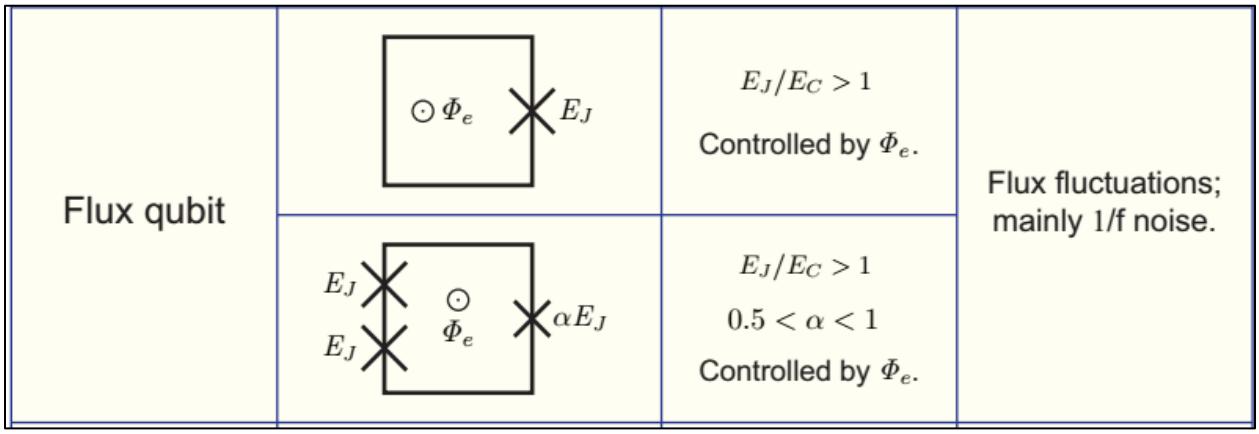


Figure 5.12: Typical flux qubit parameters at a glance.

By varying designs as well as the numbers of Josephson junctions, we can influence the behaviour of the two level system. The Hamiltonian for the two-level system of flux qubit is

$$H_{FQ} = -(\frac{\hbar\varepsilon}{2}\sigma_z + \frac{\hbar\Delta}{2}\sigma_x) \qquad \textbf{(45)}$$

where, $\hbar$ is the reduced Plank's constant, $\hbar\varepsilon$ is the magnetic energy bias of the flux qubit, $\hbar\Delta$ is the coupling energy due to the quantum tunneling of electrons between the two current states and σ_x and σ_z are the Pauli's spin-1/2 matrices in persistent current basis.

By diagonalizing **Equation (23)**, the eigenvalues are found to be $\pm\frac{\hbar}{2}\sqrt{\varepsilon^2 + \Delta^2}$. Thus the energy gap of the two level system is $\hbar\sqrt{\varepsilon^2 + \Delta^2}$. However, the flux qubit has maximum coherence time at degeneracy point, where ε=0, since it is not coupled to the low-frequency noise at this optimal point. 1/f flux noise is the largest threat to the attraction of a flux qubit. IBM Q uses the charge qubit whilst Google has opted for the transmon qubit for similar reasons. That said, none of the latter can effectively couple with a spin based quantum system in a better way than a flux qubit **[70]**.

Flux qubit manipulation

In order to operate a flux qubit, microwave pulses with frequency that corresponds to the two level system is applied to the qubit. A suitably controlled pulse duration and pulse phase drive the qubit into a quantum superposition of the two basis states. Subsequent pulses can change the probability of when a measurement is to be made thus giving the qubit its computational ability. The ratio of the charging energy and coupling energy differentiates the flux qubit from other similar technologies such as charge and phase qubits. For the flux qubit the charging energy of the junctions is far exceeded by the coupling energy. Typically, the coupling energy usually exceeds the coupling energy by about 10 to a 100 times. This ratio makes it possible for Cooper pairs to flow continuously around the flux qubit loop giving rise to a persistent current, rather than tunnel discretely across the junctions as in a charge qubit.

The ability to effective couple many flux qubits makes it possible to implement multi-qubit gates thus making it efficient to do quantum computations. There are two basic coupling mechanisms namely; direct inductive coupling (through external flux) and indirect coupling (via a microwave resonator). Direct coupling is much simpler and happens when the clockwise current in one qubit induces a counter-clockwise current in the other just like in mutual induction. In order to be useful in hybrid quantum system application, the coupling needs to be tunable. We should have varying coupling strengths; very strong coupling in some cases and very weak to no coupling in others.

We can rely on the Pauli Matrices formalism to implement a controlled-NOT gate using a $\sigma_Z\sigma_Z$ term in the Hamiltonian. To enhance direct coupling qubit loops are made to touch one another on a common edge thus introducing kinetic inductance. This topological approach makes the currents to flow through one superconducting line. If a Josephson junction is placed on that joint line a Josephson inductance term is added to the circuit thus increasing the coupling. By tuning the energy separation of the qubits to match one of the resonators, the phases of the loop currents are synchronized, and a $\sigma_X\sigma_X$ coupling is implemented. Tuning the qubits in and out of resonance by modifying their bias magnetic flux can be used to control the duration of the gate operation**.**

The most important and delicate exercise is to measure the qubit state after computation. For the flux qubit, this is achieved through a suitably sensitive probe optimized for these purposes, usually a DC-SQUID. This quantum probe is very sensitive to small changes in its environment and introduces very little back-action during measurement otherwise t influences the result that it is meant to read out. These devices should only interact during computation and then be turned "on" briefly for read-out. Read-out probes for flux qubits work by interacting with one of the qubit's macroscopic variables, such as the circulating current, the flux within the loop or the macroscopic phase of the superconductor. We can use low noise electronics to track small variations in qubit properties in a technique called projective measurement.

5.5 NV^- center in Diamond

For our work in this thesis we will concentrate on the negative NV center, since its spin displays unique optically induced polarization (or initialization), optical readout and outstanding coherence properties which are most useful for quantum information purposes. Whenever NV center appears in this work it shall be the negatively charged center unless specified otherwise.

Why NV center?

The NV center is of great interest in experimental quantum physics. The defect behaves as a two qubit system. It consists of an individual electron spin surrounded by two different nuclear spins;

one from nitrogen and others from carbon-13.
It is possible to manipulate the NV center as a qubit under simple conditions. The NV center can be excited using visible light and it is also a stable single-photon emitter. The single electron spin can be initialized and read out using optical methods whilst it can also be controlled through electromagnetic effects. Variation in photoluminescence that arises due to field effects can be accounted for in terms of quantum entanglement, spin-orbit interaction and Rabi oscillations **[71, 72]**.

Recent advances in the field of quantum technology presents great opportunities for NV centres in hybrid quantum systems. Given their good coherent times, nuclear spins interacting with the NV electronic spin are being proposed as quantum registers. Moreover, at very low temperatures it is possible to coherently interface the electron spin with photons thus building a quantum bus for networking. Finally, single shot read-out is possible for both the electron spin and nuclear spin states. Experiments are already being carried out to show that the NV centre is a good candidate for implementation of quantum registers and networks **[73-74]**.

Nitrogen-vacancy center theory

Owing to a combination of several excellent intrinsic properties including hardness, high thermal conductivity, and electron affinity, diamond comes through as an ideal material for many technical applications. Diamond thin films are a prominent subject of current research in quantum technology. At a structural level, diamond is made of carbon atoms that are joined as sp3 hybridised bonds. The NV colour centre (shown in **Figure 5.13**a) is one of many extrinsic point defects possible in diamond synthesis. It is formed inside the diamond lattice where it replaces one carbon atom with a substitutional nitrogen atom and another adjacent one with a vacancy, oriented along one of the four crystallographic {111} directions and displaying C3v trigonal symmetry. Nitrogen is a group five element with five valence electrons and forms three covalent bonds with three neighboring carbon atoms leaving one freely hanging bond within the vacancy. The three surrounding carbon atoms share this freely dangling bond.

Diamond is a wide bandgap semiconductor and this makes it transparent in the visible region, and any colors observed arise from defects – impurities, dislocations, vacancies, and complexes – which create electronic energy levels within the bandgap. Whilst there are many possible centers in diamond, the NV center is the most intensively researched. The NV color center shows at least three remarkable properties: it is extremely bright and a single center can be seen at room temperature; it can be spin polarized by shining white light on it; and its spin state can be read out by using the difference in fluorescence between the bright spin zero ground state and the relatively dark spin ±1 ground state. The NV center can be in either of two charge state, neutral charge state, known as NV0, which is a spin-1/2 system and the negative charge state, known as NV-, which is a spin-1 system.

If an electron, usually from an impurity like a nitrogen atom, also called P1 center, is captured by the vacancy (NV0) then the NV center is negatively charged and known as NV-. Since a total of six electrons are involved with the vacancy, it becomes a spin-1 system. The simplest distinguishing factor between NV0 and NV- is the emission spectra of the zero phonon line (ZPL) (**Figure 5.13b**). The NV^0 has its ZPL at 575 nm whereas the NV- at 637nm **[75-77]**.

Our work seeks to digitally simulate a hybrid quantum system including NV- centers on an online quantum platform. Optical initialization and readout of the spin state. Rabi oscillations can be observed by applying microwave radiation to the NV. Inhomogeneous dephasing of the qubit due to coupling with proximal electronic and nuclear spins can be overcome using spin-echo, which allows for refocusing of the qubit state, thereby extending the coherence time of the qubit. While we can easily manipulate and read out NV centers, the host material, diamond, imposes a fundamental constraint on the readout efficiency. Given the high refractive index of diamond, the collection efficiency is limited by a very shallow critical angle of total internal reflection. This limitation can be overcome by use of solid immersion lenses (SILs) on the surface of bulk diamond. This eliminates dispersion due to refraction, thereby improving the overall collection efficiency.

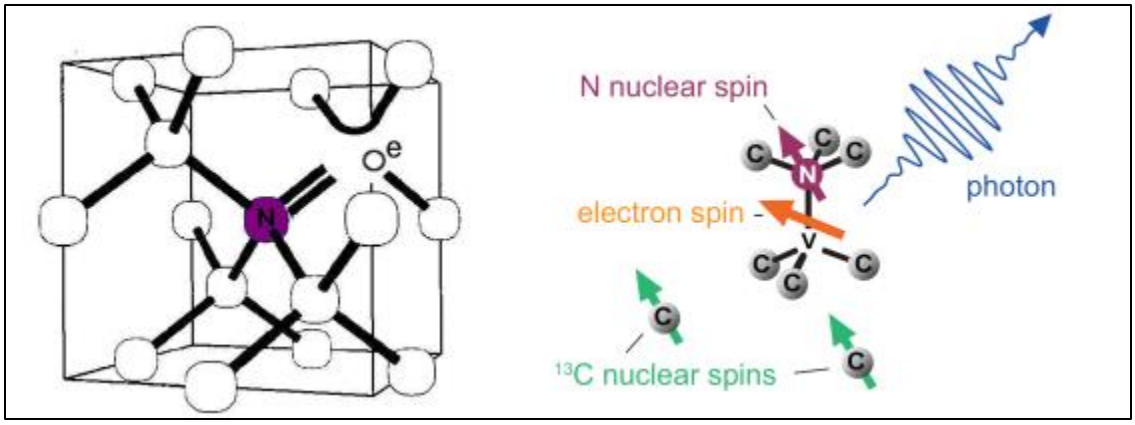


Figure 5.13: (a) Nitrogen-vacancy (NV) defect in diamond lattice. The nitrogen atom (14N) is marked with purple while the white-coloured atoms represent carbon (12C). (b) The two spins (orange for electron and purple for 14N spin) at NV centre represent the two qubits of the quantum register. Nuclear spins of the surrounding 13C nuclei are the main cause of decoherence in this system since they are coupled to the electron spin. Optical transitions inside the NV centre and the emission of photons is used for initialisation and readout. ***[76]***

The two qubits are represented by two different spins. The first qubit is defined by the spin of the electrons in NV centre and is also referred to as the electron spin. In the ground state the six electrons form a triplet (S = 1) so there are three possible values of projection of the spin alongside the NV axis, $m_S = 0, \pm 1$. The energy level of state $m_S = 0$ is separated from that of the states $m_S = \pm 1$ due to anisotropic interactions. Furthermore the states $m_S = +1$ and $m_S = -1$ are separated by the use of a static magnetic field along the axis of anisotropy (direction of NV axis, also z-axis).

In the experiment described later on a magnetic field $B_0 = 51$ mT was used. Transitions between these three spin states have different frequencies and it turns out that this qubit can be manipulated using AC magnetic field pulses. When using a frequency of 1.4 GHz only states $m_S = 0$ and $m_S = -1$ are affected. The state $m_S = +1$ remains idle because the transition frequency to this state is different as it is shifted by the magnetic field. The states $m_S = 0$ and $m_S = -1$ are later on denoted by $|0\rangle$ and $|1\rangle$ respectively. The electron spin thus represents a valid qubit. The second qubit is represented by the spin of the ^{14}N nucleus and is thus named nuclear spin. Its magnitude is I = 1. Similarly to the electron spin the energy levels of the states $m_I = -1$, $m_I = 0$ and $m_I = +1$ are different enough in the static magnetic field B_0 for the state $m_I = -1$ to remain idle. This qubit is manipulated using AC magnetic pulses of frequency 2.9 MHz.

The two states of $m_I = 0$ and $m_I = +1$ are later on denoted by $|\downarrow\rangle$ and $|\uparrow\rangle$ respectively.
The big difference in the frequencies of the AC magnetic pulses that are used for manipulation of the electron and nuclear spin is very welcome, as it enables us to control qubits independently. Most of the decoherence in this system is caused by the ^{13}C nuclear spins which interact with the electron spin. This is also why ^{13}C nuclei are shown in **Figure 5.13** (b). These nuclei are common isotopes of carbon found in nature at a rate of 1.1 % and are therefore present in diamond as well.
The decoherence interaction happens typically in a time frame of a few µs, the electron dephasing time is $T*_{2,el} = 3.6$ µs. In contrast the nuclear spin of the NV centre barely interacts with other spins besides the electron spin of the NV centre itself. Decoherence of the nuclear spin can be understood as second-order process compared to decoherence of the electron spin.

Thus the nuclear dephasing time is larger, that is $T*_{2,nu} = 5.3$ ms. Therefore we can neglect the decoherence of the nuclear spin. Different dephasing times together with different frequencies required to manipulate the two qubits lead to different qubit types so this system is an example of a hybrid spin register. Coherence is a critical parameter in quantum systems that are used for quantum information processing **[77-78]**. The coherence time is the time under which a quantum system stays in a well-defined quantum state. Due to influences from the surroundings a quantum system is naturally going to fall back to the ground state after being initialised in a process called decoherence. Decoherence takes the superposition state $|\Psi\rangle$ to a mixed state which has the probability $|\alpha|2$ of being found in $|0\rangle$ and $|\beta|2$ of being found in $|1\rangle$. Quantum systems that suffer huge decoherence are not useful as they are difficult to control.

Given that it is practically impossible to eliminate decoherence completely, a quantum system has to operate within some tolerances that depend on architecture, quantum material, and error correction techniques. Ways of protecting quantum information are continuously being developed. NV center nitrogen nuclei have good coherence times and that is the reason why we are interested in testing them for hybrid quantum systems. Quantum coherence in NV centers is preserved because phonons do not readily couple to the centers, with decoherence predominantly arising due to proximal nuclear spins (especially 13C). The good thing is 13C constitute about

1% in natural diamond and during synthesis in the lab it can be reduced significantly. Inhomogeneous broadening due to both these factors is almost completely eliminated when NV diamond is prepared, with the use of the existing cutting-edge technologies from isotopically purified carbon-12 with ultralow concentrations of excessive nitrogen **[79].**

The coupling of NV– centers **[74]** to nearby spins as well as superconducting based qubits like the flux qubit makes them a testbed for exploring hybrid quantum systems. We envisage a coupled system where the NV– is coupled to a flux qubit and provides a clear way to initialize and readout. In general the NV– center acts as 2 qubits, one for storage and another for coupling to the flux qubit. The NV– center is thus a competent alternative for a matter-based quantum architecture.
It is important to realize that although very long decoherence times for NV– have been observed at room temperature, photon coupling seems to require cryogenic temperatures and this is consistent with the demands for a flux qubit **[80]**.

Electron spin of the NV centre

The NV center is merely a spin-1 system made up of six electrons. Despite simplicity in its outlook, the spin properties of NV centers are rather complex. The NV is a color center which emits photons as a result of the optical transition between its ground and excited electronic states, which are triplet states. In order to explain the transitions, it is better to look at the NV center as having molecular orbits (MOs), rather than atomic orbitals (AOs).

Since there are four atomic orbitals involved in the NV center; one from the nitrogen and three from the carbon atoms, the linear combination of atomic orbitals leads to the construction of four molecular orbitals (MOs)**.**

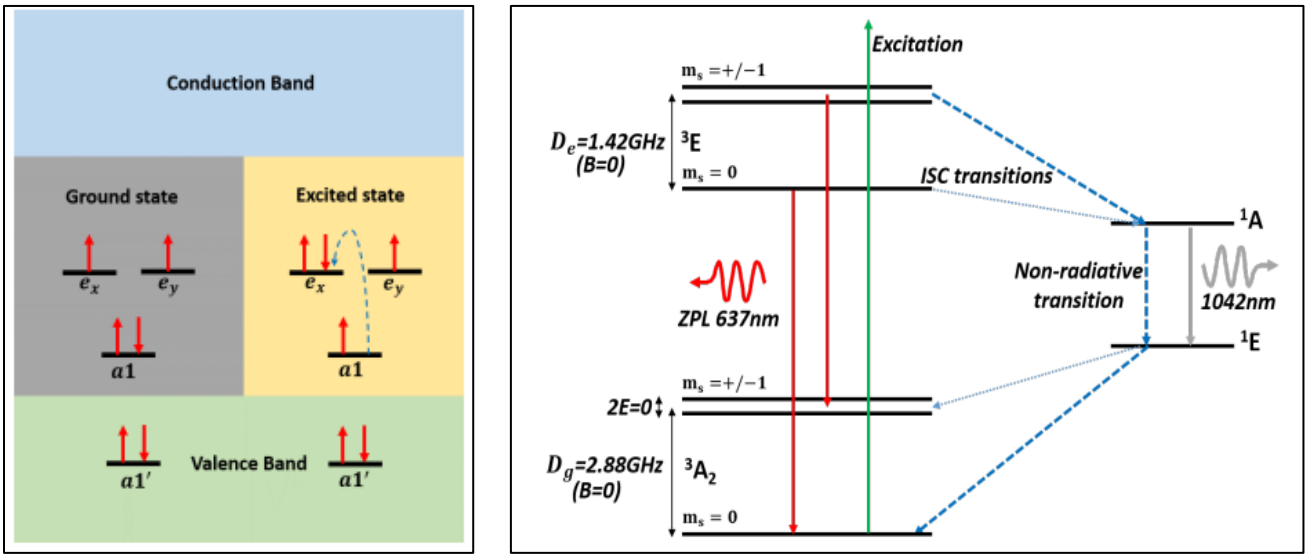


Figure 5.14: The molecular orbits for the NV centre showing ground and excited states. ***[IOP].***

There are two unpaired electrons in the excited and ground states and their interaction results in a splitting in both the ground and excited spin triplet states at zero magnetic flux. The core physics of the NV center can be best illustrated through a spin level scheme (**Figure 5.14**).

Electronic spin energy level scheme

The green arrow shows off-resonant excitation of the ground triplet state ($^3A_2$) to the excited triplet state (^3E), while radiative transition between them gives the characteristic ZPL of 637 nm. Significant and negligible inter-system crossing (ISC) transitions from ^3E to ^1A and ^1E to $^3A_2$ are shown in blue dashed and dotted arrows, respectively. The radiative transition between ^1A and ^1E corresponds to emission of light at 1042 nm. The triplet ground and excited states are denoted as $^3A_2$ and ^3E, respectively, while the two intermediate singlet states are denoted as ^1A and ^1E. The triplet states are given in terms of m_s, which is the projection of the spin along the quantization axis of the NV. The ground triplet spin state ($^3A_2$) of the NV centre needs to be explained in more detail as it is important for our work here.

Ground state of the NV centre

If we neglect any hyperfine interactions between the electron and nuclear spin (only the spin due to nitrogen will be mentioned as nuclear spin without emphasis) and choose the z-axis as the quantization axis then the ground triplet spin state can be explained with a ground-state spin Hamiltonian,

$$H_{gs} = \hbar D_g S_z^2 + \hbar E\left(S_x^2 - S_y^2\right) + g_e \mu_B B \cdot S \qquad \textbf{(46)}$$

where, $\hbar$ is the reduced Planck's constant (h/2π), D_g=2π ~ 2.88GHz is the zero field splitting due to the interaction between the spins of the two unpaired electrons in the MOs e_x and e_y, E is the strain-induced splitting between the $m_s = \pm 1$ levels of the ground triplet states, g_e is the electron g-factor, μ_B is the Bohr magneton, B is the external magnetic field potentially acting on the NV and S(S_x; S_y; S_z) are the Pauli matrices for the spin-1 operators. The last term of the equation is the Zeeman interaction term and can be expanded in x-, y- and z-coordinates. However, restricting ourselves to the weak magnetic field regime that does not affect the quantization axis, we can neglect the x and y components of the Zeeman interaction term.

Thus the splitting between the $m_s = +1$ and $m_s = -1$ due to the off-axis strain is 2E and in the absence of an external magnetic field or in the absence of any stress, $m_s = +1$ and $m_s = -1$ are degenerate. However, we can see from **Equation 37** that in the presence of an external magnetic field along the quantization axis, the degeneracy of $m_s = \pm 1$ will get lifted even in the absence of any stress due to the Zeeman splitting. **Figure 5.15** shows the Zeeman splitting of ground state $m_s = \pm 1$ spin states, for the applied magnetic field along the quantization axis, z.

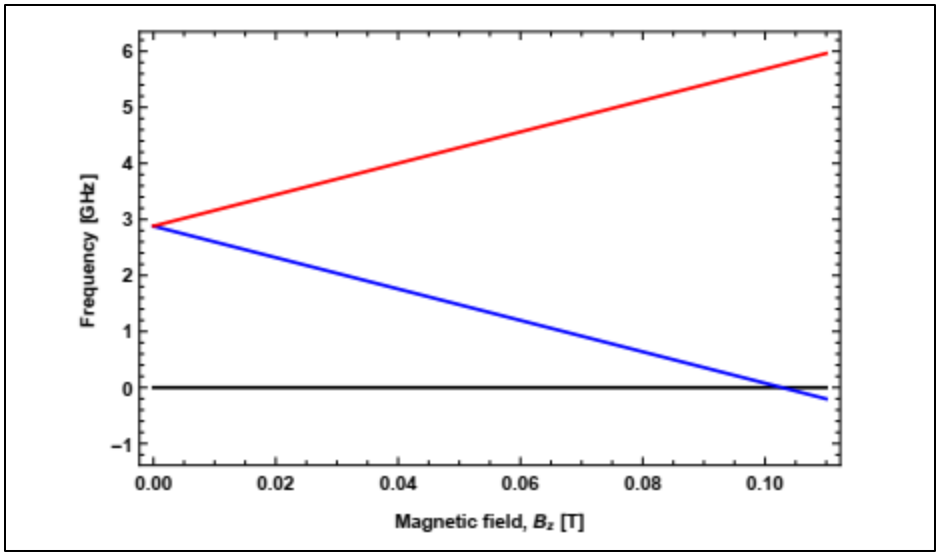


Figure 5.15: Zeeman splitting of ground state $m_s = \pm 1$ spin states. The black line represents the $m_s = 0$ state, the blue line represents the $m_s = -1$ state and the red line represents the $m_s = +1$ state. The stress splitting has been taken as $E/2\pi = 5MHz$. ***[Wikimedia]***

Figure 5.15 has been obtained from **Equation 24**, by considering the positions of the $m_s = \pm 1$ spin states relative to the $m_s = 0$ state. The stress induced splitting value is taken as $E/2\pi$=5MHz, which is a typical value for nanoscale diamonds. The plot clearly shows that when $B_z \approx 0.1$ T, then the $m_s = 0$ and $m_s = -1$ states would be degenerate in energy, which is referred to as 'level anticrossing'. The Zeeman splitting of the $m_s = \pm 1$ ground spin states can be used to detect an external magnetic field by quantifying the energy splitting, using an experimental method called optically detected magnetic resonance (ODMR) **[82, 84].**

Control of the NV centre spin

The ability to interact and control the NV centres through external electromagnetic fields makes them attractive for solid state quantum technologies. The NV centre spin can be initialized into the $m_s = 0$ ground state using lasers while precise control is done through external microwave pulses resonant with the spin-splitting transition.

Spin polarization of the NV centre

With an excitation of suitable wavelength (for example 532 nm) the NV centre undergo spin selective optical transition ($\Delta m_s = 0$), from $^3A_2$ to ^3E (**Figure 5.14**). The ^3E triplet state is coupled to the upper singlet state ^1A and the lower singlet state ^1E is coupled to $^3A_2$ through spin-orbit interaction. If the NV centre reaches the $m_s = 0$ state of ^3E it undergoes radiative transition to $m_s = 0$ of $^3A_2$ with emission of photons at 637nm, while the inter-system crossing (ISC) transitions from $m_s = 0$ of the triplet ^3E state to ^1A are negligible. On the other hand, the probability is low for a an NV centres that reach the $m_s = \pm1$ state of 3E to undergo non-radiative ISC transitions to the ^1A singlet state and undergo a decay along with a radiative transition at 1042 nm between the two singlet states ^1A and ^1E. It ultimately end up in the $m_s = 0$ state of $^3A_2$ from ^1E through the ISC transition; the transitions from ^1E to $m_s = \pm1$ of $^3A_2$ are instead negligible.

An NV centre polarised into its $m_s = 0$ state of the ground triplet $^3A_2$ displays maximum fluorescence upon excitation as there is no ISC transitions. However, if a MW field in resonance with the energy difference ($\sim$2.88 GHz) of $m_s = 0$ and $m_s = \pm1$ states of the $^3A_2$ manifold is applied, a decrease in fluorescence intensity is observed as the spin state $m_s = \pm1$ scatters less photons than the 'bright' ms = 0 state (note that in the ideal case, i.e. no stress or zero magnetic field, $m_s = +1$ and $m_s = -1$ are degenerate. The degeneracy can be lifted by means of an external magnetic field or induced stress). This property can be used for read out of the NV centre spin **[83-85]**.

Spin control of the NV centre in the ground state

The ability to coherently manipulate the spin polarised NV centre is an important requirement for quantum technological applications. This is readily achieved with an external MW field. The dynamics of the spin state of spin polarised NV centres can be traced via their fluorescence. By applying a MW frequency resonant with the $m_s = 0$ and $m_s = \pm1$; the fluorescence reveals an oscillatory behaviour. This oscillation is known as Rabi oscillation between the population of $m_s = 0$ and $m_s = \pm1$ states of $^3A_2$, with the characteristic frequency known as Rabi frequency.

The Rabi oscillation can be understood by visualizing the spin states in the Bloch sphere as shown in **Figure 5.16**. The general representation of the spin state in the Bloch sphere is,

$$|\psi_{sp}> = \cos\frac{\theta}{2}\,|0> + e^{i\phi_{ph}} sin\frac{\theta}{2}|1> \qquad \textbf{(47)}$$

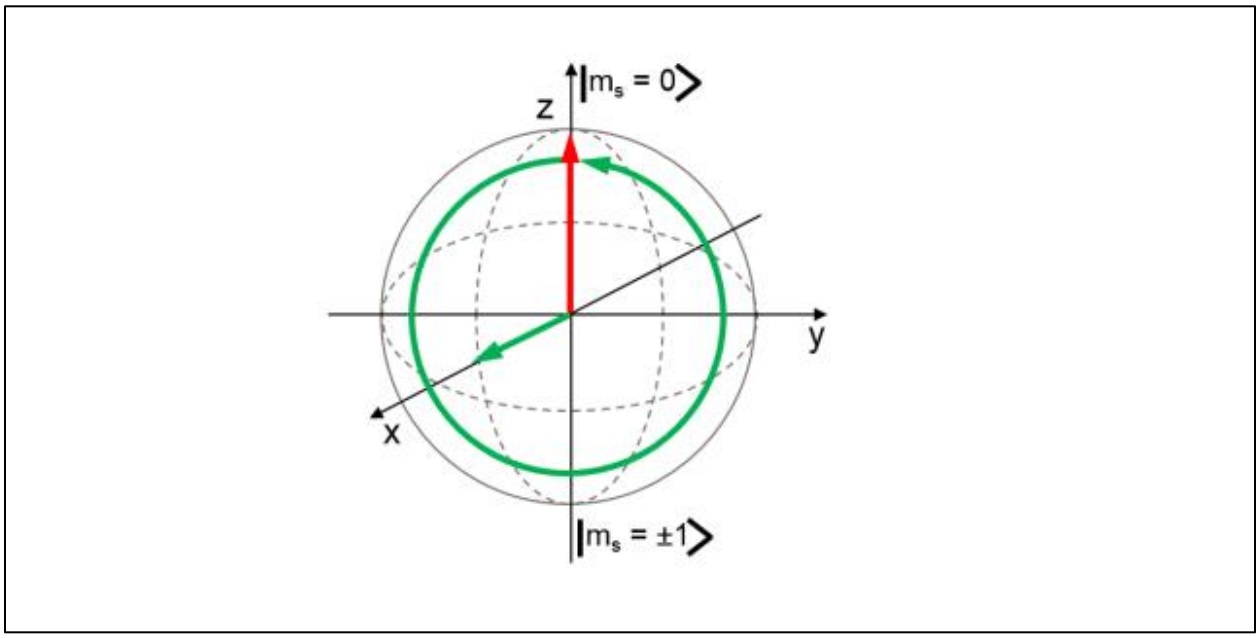


Figure 5.16: Spin state fluorescence represented on a Bloch sphere. Red arrow-spin state of the NV centre. Green arrow-externally applied MW field. Green rounded arrow-Larmor precession of the spin state around the applied MW field. ***[44]***

The angle θ is the angle to the state from the z-axis and the phase angle ϕ_{ph} is the angle to the projection of the state in the *x-y* plane from the *x*-axis. Here, we consider the spin polarised system so that the spin state of the system in the Bloch sphere is represented along the *z*-axis (red arrow). When a resonant microwave field (magnetic field strength H) is applied to the spin polarised system of the NV centre, along the x-axis (ϕ = 0), the spin will undergo a Larmor precession around the applied field. The frequency of the precession is known as Rabi frequency and the spin state oscillates between |0> and |1>.

The fluorescence of the NV centre is a measure of the probability of finding the system in |0>. The length of the MW pulse for which the spin state of the spin-polarised NV centre inverts from $m_s = 0$ to $m_s = \pm 1$ (correspondingly lower fluorescence) is known as a π pulse (θ = π in the Bloch sphere).

Duration and phase of the microwave pulses are employed to simulate quantum gates of choice in implementing a quantum processor. In that way NV centres appear to be naturally predisposed to operate in quantum computation applications.

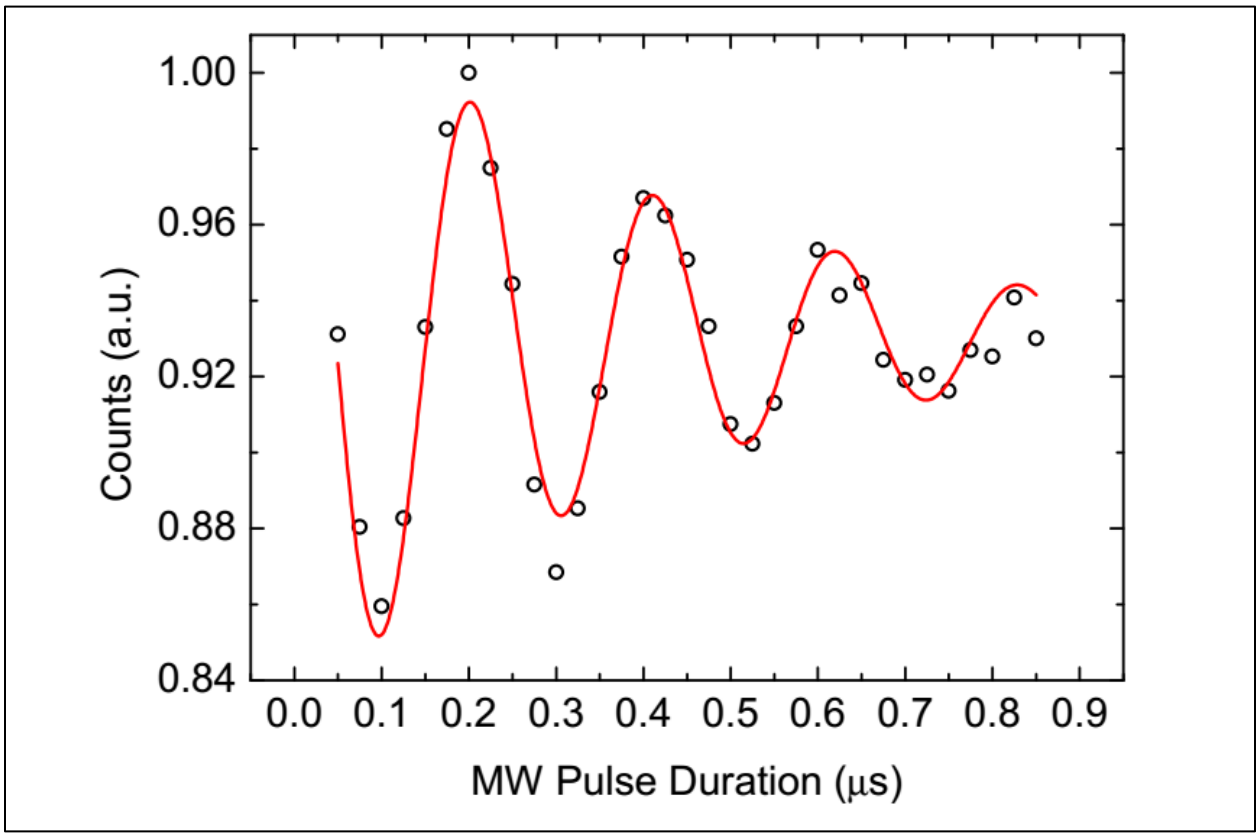


Figure 5.17: Rabi oscillation for a single NV centre showing a fit to experimental data points. ***[82]***

The Rabi oscillation of a single NV centre shown in **Figure 5.17** shows an exponentially decaying behaviour. This is due to decoherence, which is basically the irreversible loss of coherence due to interaction with the environment.

Relaxation times

The spin polarised NV center system cannot last in the desired state forever. The system relaxes over time due to environmental effects. This loss in valuable information is accounted for by two variables: 'longitudinal electron-spin relaxation time (T1)' and 'transverse spin phase coherence time (T2)'.

T1 is the lifetime of a polarised spin state, and its deterioration is due to random processes (e.g., interactions with phonons) which produce irreversible changes in the axial spin projection of the state. Room temperature relaxation T1 for an NV center in diamond is in the millisecond range which means that at lower temperatures where there is limited phonon interaction it can be tremendous and comparable only to trapped ions.

T2 is the measure of time in which loss of phase coherence of spin state is taking place and determined by the (off-resonant) interaction between a single spin and the 'spin bath' of the surrounding environment. This interaction results in the loss of phase memory of the single spin via the dipolar interaction with the fluctuating local field generated by the local spin bath. Experiments give an average value of the inhomogeneous dephasing times, which is usually denoted as T2 * (≤T2). A pictorial view of what happens on relaxation is shown in **Figure 5.18**.

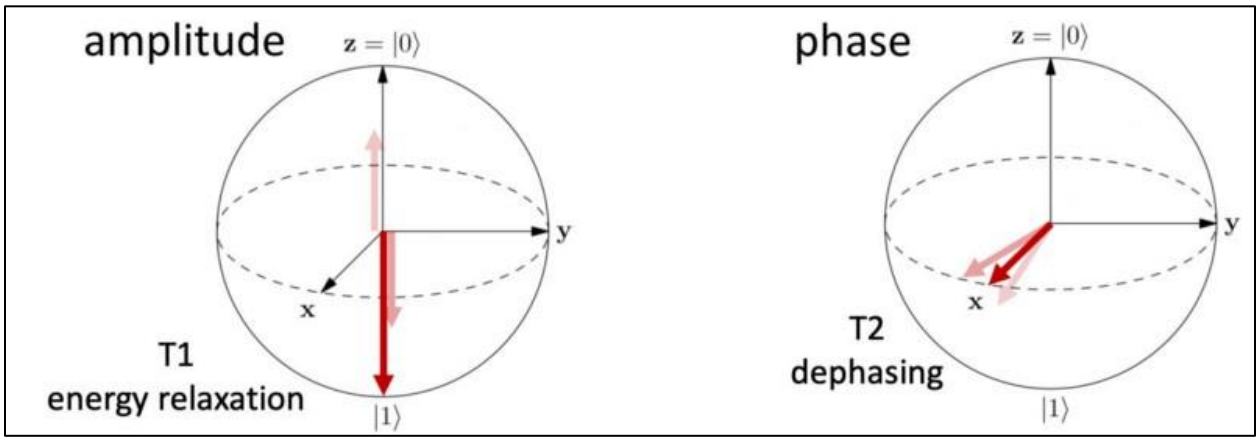


Figure 5.18: Energy relaxation and dephasing as decoherence sources.[IBM]

The main culprit for dephasing in diamond NV centers is the surrounding paramagnetic impurities in the lattice (e.g., N and 13C atoms) which display dipolar coupling to the NVs. At room temperature, T2 for nanodiamond NV centers is in the microsecond range. Decoherence time can be improved either by lowering the temperature or by using samples with lower number of P1 centers. Another pathway is dynamical decoupling, which involves the decoupling the NV spins from their spin bath, for instance by using an inverted or fast pulse sequence.

5.5 Hybrid Quantum System

Why a hybrid quantum system?

A major challenge in using a solid-state system as a platform for a quantum computer is decoherence, which is the irreversible loss of quantum information that is encoded in a qubit. Decoherence of a solid-state qubit is caused by uncontrolled interaction of the qubit with its environment. To minimize such interaction, it is attractive to encode the qubit in the magnetic moment (spin) of a single impurity atom which is trapped in the lattice of a host material. This type of qubit combines the good isolation and associated long coherence time of a trapped atom with the versatility and potential scalability of a solid-state based system. A comparison of different quantum technologies and their parameters is shown in **Table 5** below.

	Atom, molecule, ion	*Electron spin*	*Nuclear spin*	*Superconducting qubit*
Size	$\sim 10^{-10}$ m	$\sim 10^{-10}$ m (impurities) $\sim 10^{-8}$ m (quantum dot)[a]	$< 10^{-10}$ m[a]	$\sim 10^{-6}$ m
Energy gap	10^5–10^6 GHz, $\sim$ GHz (Rydberg atoms)	1–10 GHz	1–10 MHz	1–20 GHz
Frequency range	Optical, microwave	Microwave	Microwave	Microwave
Operating temperature	nK to μK	$\sim$ 100 mK (quantum dot) room temp. (NV center)	$\sim$ mK	$\sim$ 10 mK
Single-qubit gate operation time τ_1	$\sim$ μs (atom) $\sim$ 50 ps (ion)	$\sim$ 10 ns	$>$ 10 μs	$\sim$ 1 ns
Two-qubit gate operation time τ_2	$\sim$ μs (atom) $\sim$ 100 μs (ion)	$\sim$ 0.2 ns	$\sim$ 10 ms	$\sim$ 10–50 ns
Coherence time T_2	ms to s	ms to s	$\sim$ s	$\sim$ 10–100 μs
T_2/τ_1	10–10^4	10^5–10^8	10^6	10^4–10^5
Coupling type	Electric or magnetic	Magnetic or electric	Magnetic	Electric or magnetic
Coupling strength with the cavity	$<$ kHz (B-field), $\sim$ 10 kHz (E-field), $\sim$ 10 MHz (Rydberg atoms)	$\sim$ 100 Hz (impurities) $>$ MHz (quantum dot)	$\sim$ 0.1 Hz	$\sim$ 0.1–1 GHz

Table 5: Comparison between different systems used as qubits.

Nuclear spins are generally more robust to decoherence than electron spins because of their smaller magnetic moment and accompanying smaller interaction with the environment. Nuclei are therefore more attractive for storing quantum information. However, the weak interaction between different nuclei, even if they are only a few lattice sites apart, makes coupling them very

difficult. Electrons, on the other hand, interact much stronger but correspondingly have shorter coherence times. An appealing idea is to develop a hybrid system, consisting of qubits of different species each optimized for its specific task. Nuclei store quantum information, electrons mediate the transfer of quantum information between superconducting and spin qubits. The NV center acts as both quantum register and quantum bus whilst the flux qubit acts as a fast processing qubit.

Superconducting qubits, atoms and spins can also couple to co-planar waveguide resonators, producing a hybrid cavity-quantum electrodynamics (QED) system. In the direct-coupling case, superconducting qubits couple with NV centers via electromagnetic fields whereas indirect-coupling relies on a high-fidelity quantum resonator (e.g., coplanar waveguide resonator) that can be based on HBDD thin films to act as a data bus to transfer (quantum) information between the components of the hybrid quantum system. HBDD thin films are a promising material for quantum hardware.

Coupling diamond NV centers to a superconducting flux qubit

The NV centre is robust and can thus be coupled to other quantum systems like superconducting flux qubits to build hybrid quantum systems. The goal in building a hybrid quantum systems is to combine outstanding properties of each subsystem to build a scalable and universal quantum system capable of quantum computation and quantum simulation. NV centers have long coherence times whilst superconducting qubits are exceptional at processing speed. Moreover, it is possible to couple these two subsystems directly through external magnetic flux and indirectly through a resonator. In summary a hybrid quantum system made from the NV center and flux qubit has the following advantages; good tunability, scalability, long coherence times and stability. In addition, the magnetic coupling between superconducting qubits and NV centers can be stronger than that between NV centers and a transmission line resonator by three orders of magnitude making direct coupling a first choice consideration.

Amongst the distinct advantages of this hybrid system is the ability to be used as a platform for simulating the abundant features of many-body systems like the Jaynes Cummings (JC) lattice,

and quantum phase transition in superconducting thin films.

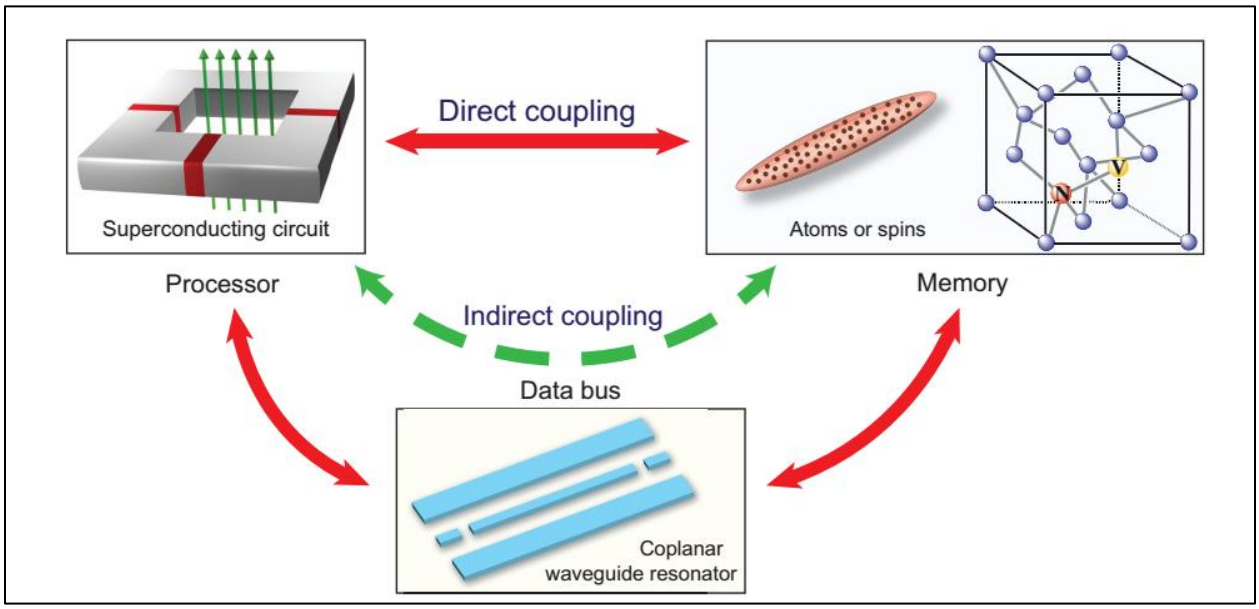


Figure 5.19: The different mechanism of coupling in hybrid quantum systems. ***[74]***

Cavity-mediated coupling, a direct coupling between a flux qubit and a spin ensemble can be achieved (see **Figure 5.19**). However, the application of the flux qubit in quantum computing is limited due to its short coherence time. The nitrogen-vacancy (NV) center has been used as the quantum memory in the hybrid system owing to the attractive properties of extremely long coherence time. In this thesis we seek to explore direct coupling of the flux qubit with a spin centre.

Implementation of a hybrid qubit system

The magnetic field applied to operate the flux qubit, together with the strain field in the diamond crystal lift the degeneracy of the ground state ms = ±1 of the NV centre. Thus the $m_s = 0$ and $m_s = 1$ form an effective two-level system to which one can couple the resonant flux qubit.

The Hamiltonian for this coupled system can be written as,

$$H = H_{NV} + H_{FQ} + H_{int} \qquad \textbf{(48)}$$

where H_{NV} is the ground-state Hamiltonian of the electronic spin of the NV centre and H_{FQ} is the Hamiltonian of the flux qubit. The interaction Hamiltonian can be written as,

$$H_{int} = g_e \mu_B \sigma_Z B_{FQ} \cdot S \qquad \textbf{(49)}$$

where, $\mathbf{B_{FQ}}$ is the magnetic field generated by the flux qubit.

Considering the fact that the coherent coupling is not possible along the quantization axis of the NV centre, which is considered as the z-axis in the present study, the interaction Hamiltonian can be rewritten as,

$$H_{int} = g_e \mu_B B_{FQ}^{(x,y)} \sigma_Z (S_x \cos\theta_{xy} - S_y \sin\theta_{xy}) \qquad \textbf{(50)}$$

where $B_{FQ}^{(x,y)}$ is the magnetic field generated by the flux qubit in the x-y plane. θxy is the angle from the x-axis to $B_{FQ}^{(x,y)}$ in the x-y plane which depends on the position of the NV centre. The strength of the coupling of a single NV to a flux qubit is

$$g = g_e \mu_B B_{FQ}^{(x,y)} \qquad \textbf{(51)}$$

The next step is to break down the Hamiltonian into unitary evolution matrices that we will use for digital implementation. Lloyd (1996) argued that any Hamiltonian, say

$$H = \sum_{i=1}^{m} H_i \qquad \textbf{(52a)}$$

which can be decomposed into m local terms $\{H_i\}$ can be simulated efficiently by a universal quantum computer. Each H_i term acts on at most k qubits.

The foundation of this idea is founded on the Trotter splitting "trotterisation" of all non-commuting operators,

$$e^{-iHt} \approx \left(e^{-\frac{iH_1 t}{n}} e^{-\frac{iH_2 t}{n}} \ldots\ldots e^{-\frac{H_m t}{n}} \right), \qquad \textbf{(52b)}$$

Previous research of coupling NV centers in diamond to flux qubits have used ensembles to achieve strong coupling regimes. It is also possible to increase the coupling strength through the application of strong magnetic fields at the NV center location **[84]**.

The NV centre is randomly located inside the diamond which is assumed to be spherical for simplicity. When we place the diamond crystal in the vicinity of the flux qubit, an NV centre would experience a (slightly) different coupling strength. The interaction between the NV center and the magnetic field produced by the flux qubit leads to a coupling between the two systems magnetic field applied to operate the flux qubit, together with the strain field in the diamond crystal lift the degeneracy of the ground state ms = ±1 of the NV centre. Thus the $m_s = 0$ and $m_s = 1$ form an effective two-level system to which one can couple the resonant flux qubit.

Chapter 6

Experimental Methods

6.1 Quantum Simulation

Quantum simulation builds upon a long tradition of simulation in the classical realm: The 20th century can be seen as the age of information and computers. But, even supercomputers have their limitations. For this reasons already in classical computer science the concept of special purpose computers has been developed. Such “classical simulators” are unlike universal classical computers – they can only simulate or calculate certain restricted class of models describing nature. For example, the best simulations of classical disordered systems, such as spin glasses, are nowadays obtained with such computers of special purpose - “classical simulators”. Similarly, the simulation of the aerodynamics of cars in a wind tunnel can be seen as a classical special purpose computation in this sense.

The basic idea of a quantum simulator is both ingenious and rather simple: Instead of trying to simulate quantum dynamics on standard computers, one intentionally and artificially reproduces the quantum dynamics on another quantum system, under precisely controlled conditions in the laboratory. This approach allows for reproducing known physical systems in a setting where a plethora of different ways of probing and measuring the system is available, for example by emulating a solid state system on a much larger length scale, such that optical resolution of individual atoms can be achieved.

The basic idea of a quantum simulator is due to Feynman, who not only “invented” the concept in a keynote speech. He also addressed rather subtle issues of the mutual efficient inter-convertibility of different quantum systems, anticipating a scientific discussion about the precise validity in quantum mechanics of the Church Turing thesis, which captures how well computer architectures can simulate each other. Yet, it is only now, with experimental procedures having progressed to an extent that such controlled quantum many-body dynamics is really conceivable that quantum simulation has developed into a burgeoning field of research.

By now, many realistic experimental candidate systems exist, which already demonstrated their potential to truly outperform classical computers. These include for example ultra-cold atoms in optical lattices, ultra-cold trapped ions, atoms in arrays of cavities, ultra-cold atoms near nano-structures, arrays of quantum dots, superconducting circuits, photons in linear optics devices, as well as photons/polaritons in arrays of cavities.

Scalable quantum computing relies on quantum entanglement and superposition in order to outmuscle classical computers on certain problems. Superposition allows the quantum processor access to a huge operating space whilst entanglement allows for storage of information and parallelism when it comes to information processing. Moreover, universal quantum computing requires gate operations with fidelities above a certain threshold. Reaching this threshold remains challenging, primarily due to two issues: (i) the control fields driving the gate operations have often experimental uncertainties, such as amplitude errors, that are bigger than the allowed deviations and (ii) the quantum systems cannot be completely shielded from the effects of a noisy environment**.**

IBM quantum computers allow a user to utilize gates from the Clifford+T gate library with some restrictions on the applicability of C-NOT gates based on the selected architecture. Building upon the demonstration of coherent control and single-shot readout of the electron and nuclear spins of individual ^{13}C and ^{14}N atoms in diamond, we run a digital experiment to explore the aspect of hybrid quantum systems and acquire knowledge useful to future success in building a scalable quantum computer.

6.2 IBM Quantum Experience (IBM Q)

In May 2016 IBM made a universal quantum computer available to the public online via the cloud. The IBM Q Experience is an online platform that gives users in the general public access to a set of IBM's prototype quantum processors via the cloud, an online internet forum for discussing quantum computing relevant topics, a set of tutorials on how to program the IBM Q devices, and other educational material about quantum computing. It is an example of cloud based quantum computing.

As of May 2018, there are three processors on the IBM Q Experience: two 5-qubit processors and a 16-qubit processor. This service can be used to run algorithms and experiments, and explore tutorials and simulations around what might be possible with quantum computing. The site also provides an easily discoverable list of research papers published using the IBM Q Experience as an experimentation platform.



Figure 6.1: (Left) A look inside the 50-qubit quantum computer at IBM. (Right) The enclosure of the quantum computer. ***[IBM]***

IBM's quantum processors are made up of superconducting transmon qubits, located in a dilution refrigerator (see **Figure 6.1**) at the IBM Research headquarters at the Thomas J. Watson Research Center **[80].**

IBM Q Architecture

From the many ways to implement qubits, the IBM Q quantum computer favors a superconducting qubit architecture called a transmon to create a quantum system. The superconducting circuit is the quantum processor.

The 5-qubit processor is a connection of qubits and resonators to allow for communication (see **Figure 6.2**). In order to execute quantum computations, a series of electromagnetic impulses at microwave frequencies (around 4–6 KHz) are sent to the resonator coupled to the qubit. This frequency resonates with the energy separation between the energy levels for |0⟩ and | one ⟩.

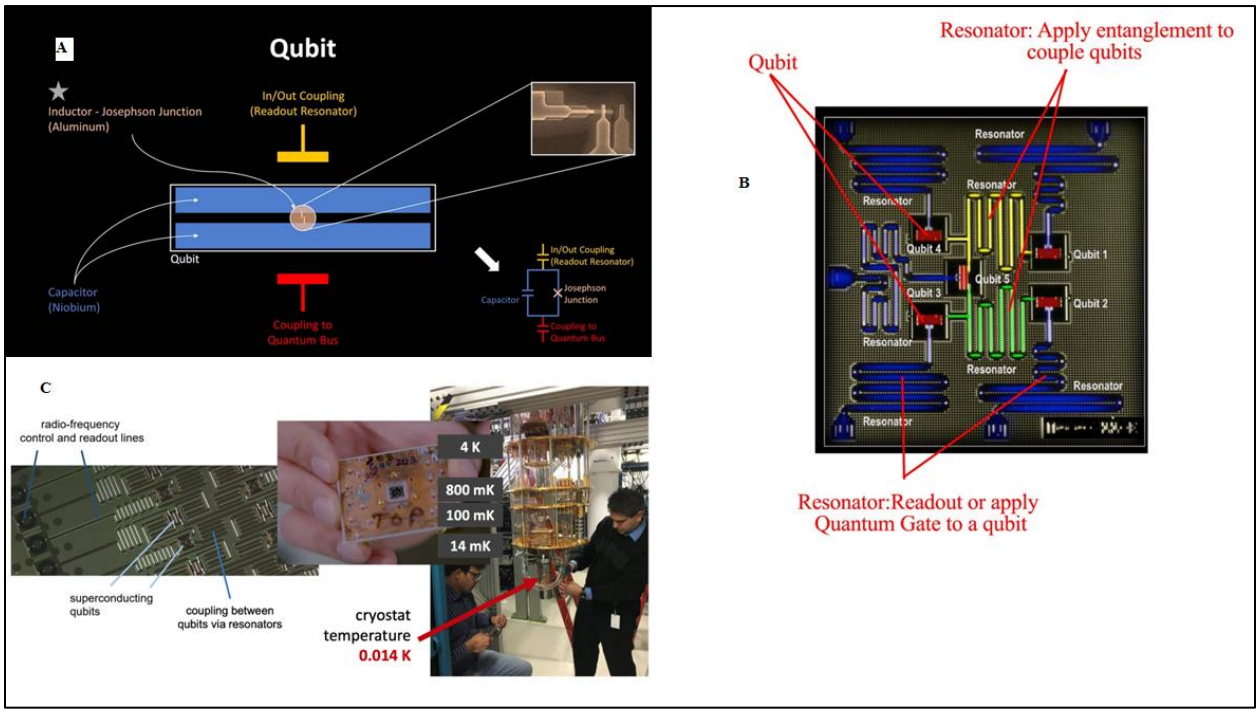


Figure 6.2: Qubit architecture (a) The transmon qubit with the JJ enlarged. (b)Modified diagram of the 5-qubit processor. (c) The 5-qubit enlarged then actual size and the dilution refrigerator electronics. ***[IBM]***

Perhaps the most critical piece of hardware after the actual quantum processor is the cryostat (dilution refrigerator) illustrated on **Figure 6.3**. Its purpose is to protect the sensitive qubits from environmental perturbations as much as possible. It provides very low temperature during operation and also has shielding for stray electromagnetic fields. This dilution refrigerator uses helium-3 and helium-4 gases for cooling to lower the lowest level temperature from 4K to 15mK.

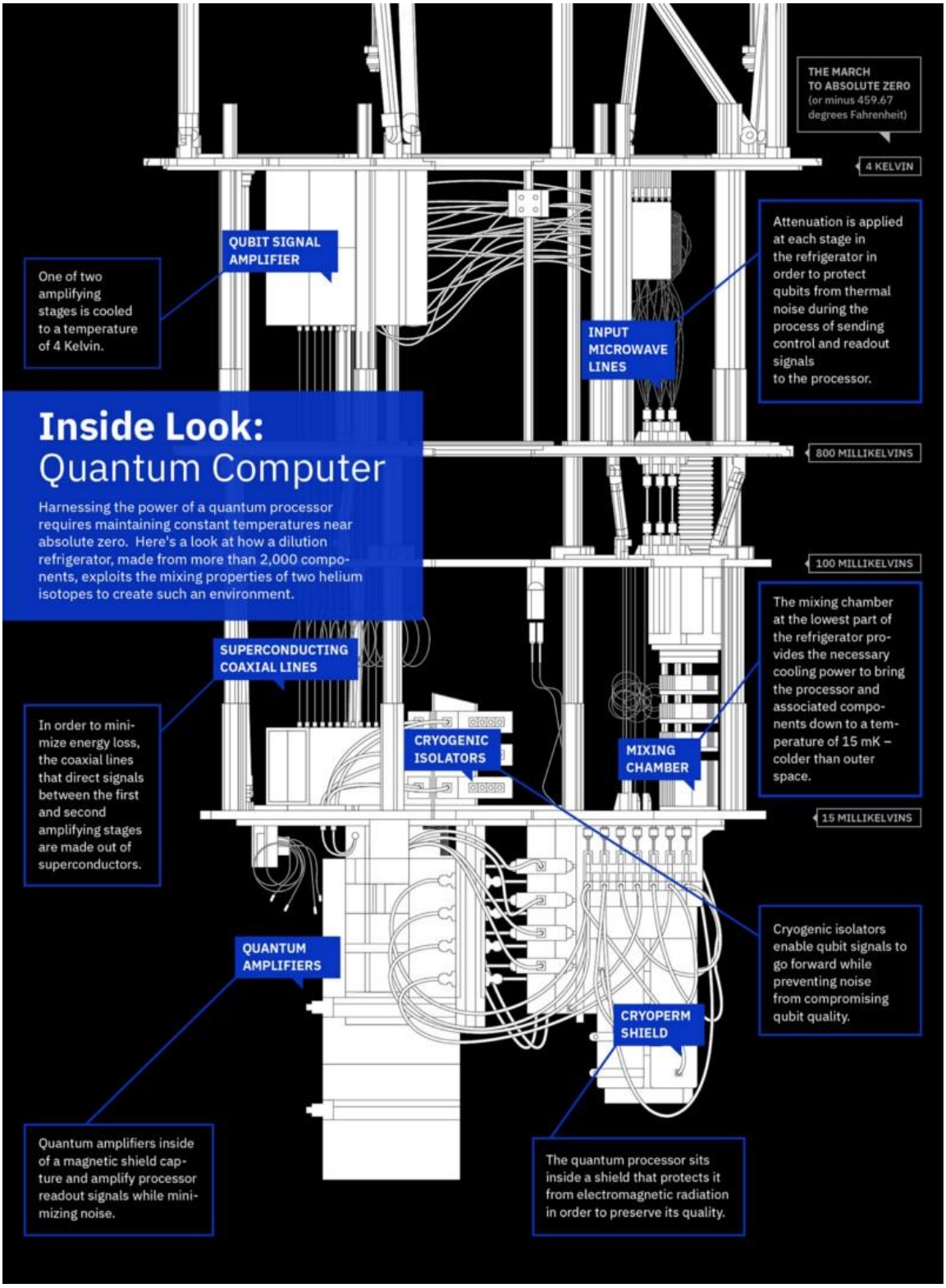


Figure 6.3: An inside look into the IBM Quantum Computer. ***[IBM]***

Interacting with IBM Q

In general, to program the IBM quantum processor we can begin by breaking down the Hamiltonian of their quantum model into unitary evolution gates through "Trotterisation" or by applying the Quantum Fourier Transform (QFT). This converts a problem into quantum gates or a quantum circuit model. The gates are then applied onto the IBM processor through a graphical user interface called a composer. Adding quantum gates on the platform is practically feeding information about pulse durations and phases of microwave pulses that are going to be applied. In particular, it is just a variation of the frequency of the signals which perhaps is similar to a variation of tones that makes up music. We guess this where the idea of a quantum composer comes from. Analogous with classical computers adding quantum gates to the composer is like writing quantum assembly language code. One would be programming the quantum processor hardware to behave according to the commands. When you click the system to run the quantum gates added to the composer are converted into microwave pulses and send through resonators to the 5-qubit processor, which is made up of transmon qubits that are connected in a star geometry (**Figure 6.4**). Principally, a full Clifford algebra is available, with the exception that the CNOT gate can only be performed on the center qubit with any of the four peripheral qubits. IBM cautions that the system is only robust enough to allow research experiments, and in particular the demonstration of quantum entanglement.

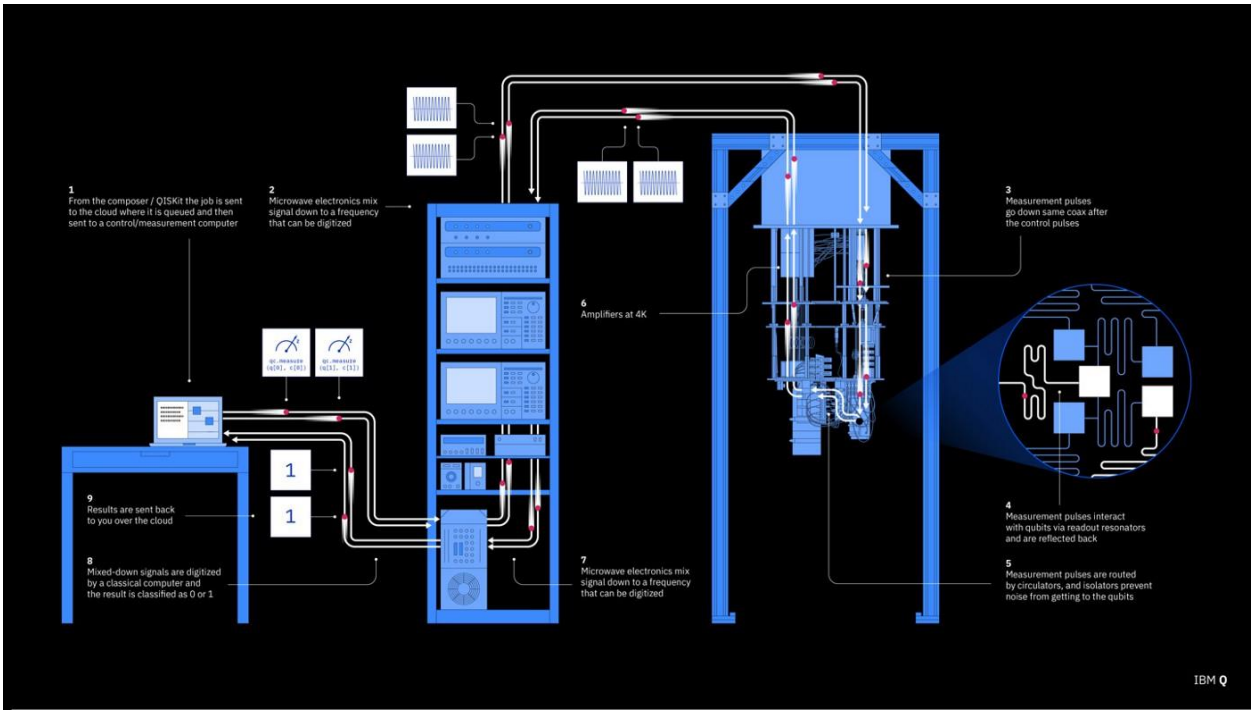


Figure 6.4: Process flow diagram for a quantum algorithm through the IBM Q platform from pulse generation, qubit control and readout.

Quantum Experience as IBM calls it is calibrated daily, and its typical temperature is around 15mK and the decoherence time of the single qubits are between 50-100μs. However, we should hasten to say that only projective measurements of the single qubit states in z-direction qubits can be performed, i.e., it can be measured whether the single qubits are in $|\uparrow\rangle$ or $|\downarrow\rangle$. No quantum tomography for the joint state is available, which means that no direct measurements of correlations between qubits can be performed. Unlike classical computing, we don't apply logical operations or common arithmetic on qubits. There is no "while statement" or "branching statement" in quantum computing. Instead, we develop unitary operators to manipulate qubits with the principle of interference in quantum mechanics. But what is the real meaning of unitary in the real world? It means operations are reversible. For any possible operation, there is another one that can undo the action. If an operator is unitary, it can be implemented in a quantum computer. IBM Q computers use microwave pulses of different frequency, phase, and duration to build a basic set of quantum operators on qubits composed of superconducting circuits. **Figure 6.5** shows the sequence of operations used to implement a quantum algorithm.

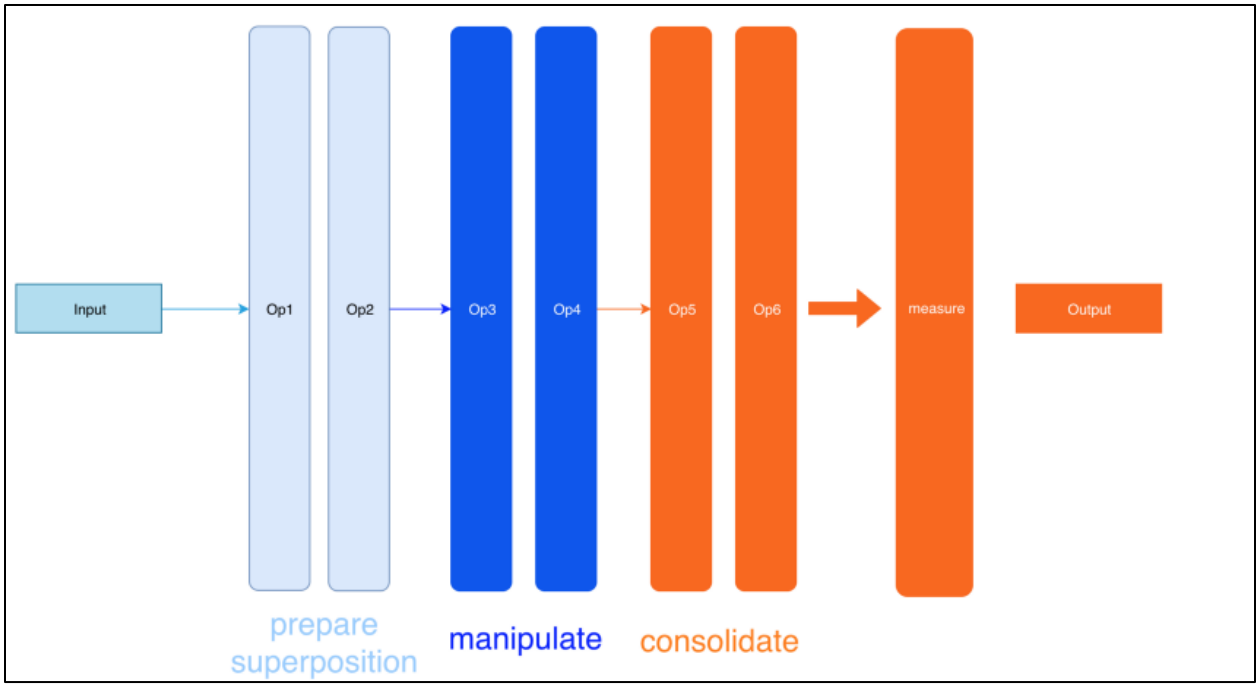


Figure 6.5: A quantum algorithm can be composed of three stages before making a measurement. These stages are initialization, computation and measurement where measurement collapses the state to either |0> or |1>. ***[IBM]***

At the basic level a quantum gate is any operation that is applied to a qubit in order to change its state. One of the most important features of a quantum processor is the ability to generate entanglement. At least a two-qubit gate equivalent to the CNOT is required to implement entanglement.

For the IBMQ quantum gates are performed by sending electromagnetic impulses at microwave frequencies to the qubits through coaxial cables. These electromagnetic pulses have a particular duration, frequency, and phase that determine the angle of rotation of the qubit state around a particular axis of the Bloch sphere. For single-qubit operations, only one pulse type needs to be calibrated, namely $X_{\pi/2}$. From that pulse, we can create all the gates you found in the Quantum Composer library. For example, we implement the S gate with the help of a phase transform performed purely in software, which affects the physical implementation of subsequent gates. However, this does not mean that the gate is necessarily error-free, as doing a software phase transform still requires very good phase stability from the instruments. Another example is the Hadamard gate performed by the sequence $SX_{\pi/2}S$.

6.3 Fundamental gate operations

Hadamard gate

First, we prepare a superposition so we can take advantage of quantum parallelism. Once it is in a high dimensional space, we create a lot of elbow room for manipulation. Then, we consolidate the superposition before the measurement. The most common and effective way to prepare superposition is the Hadamard gate. For example, we apply n Hadamard gates in parallel to prepare n qubits in one single step.

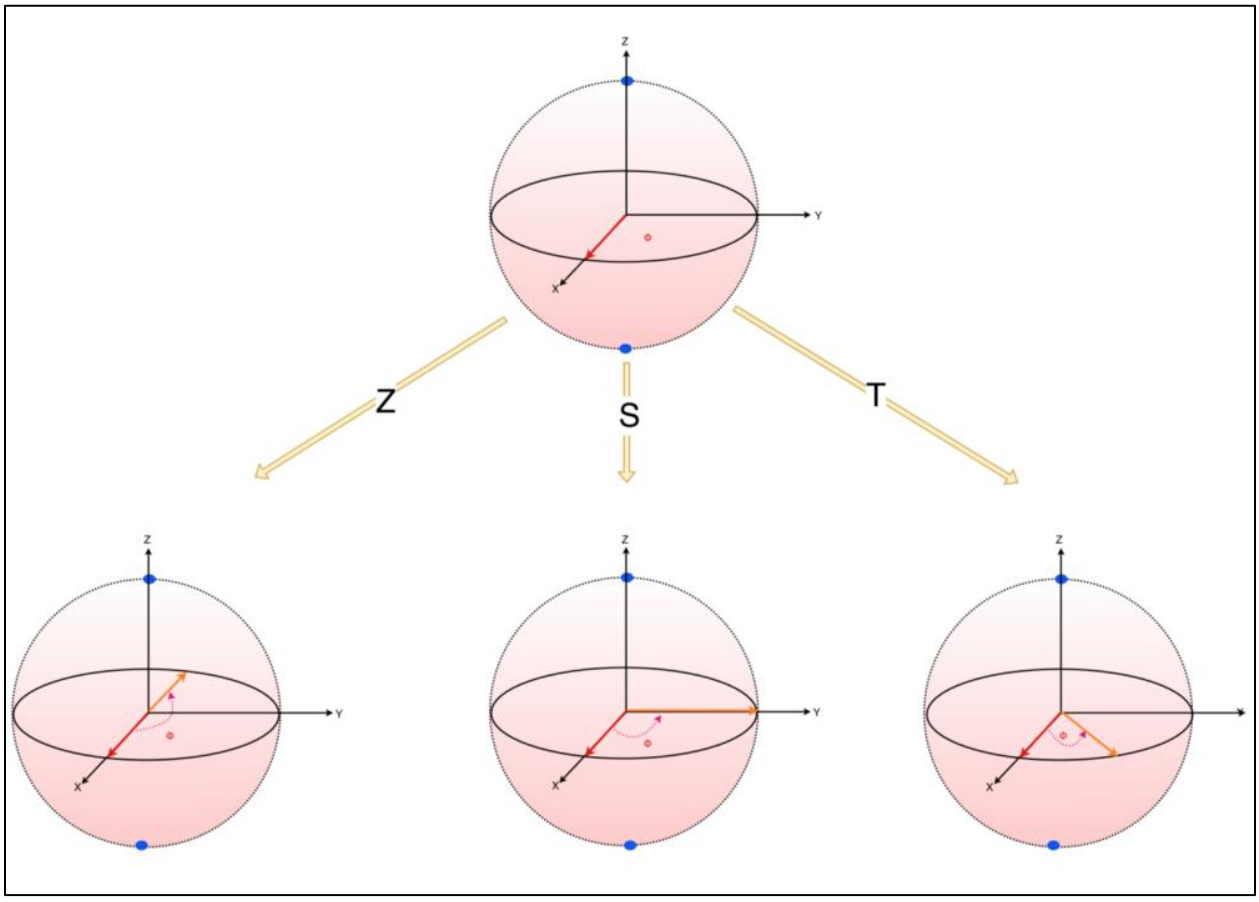


Figure 6.6: The gates that rotate the vector around the z-axis, namely Z, S, and T-gate.

As shown in **Figure 6.6** we just cover the Z-gate that rotates Φ by π. S-gate changes the phase of |1⟩ by a factor of i. i.e. a π/2 rotation around the Z-axis. T-gate has a π/4 rotation around the Z-axis. The generic phase shift gate rotates z by an arbitrary θ. It changes the phase of |1⟩. Quantum computers are built on top of single-qubit and 2-qubit operators.

CNOT-gate (controlled-NOT)

CNOT-gate operates on two qubits as shown in **Figure 6.7**: the control qubit |x⟩ and the target qubit |y⟩. If the control qubit is 0, it does nothing to the target qubit. Otherwise, it flips it. This is one of the most common gates in a quantum algorithm.

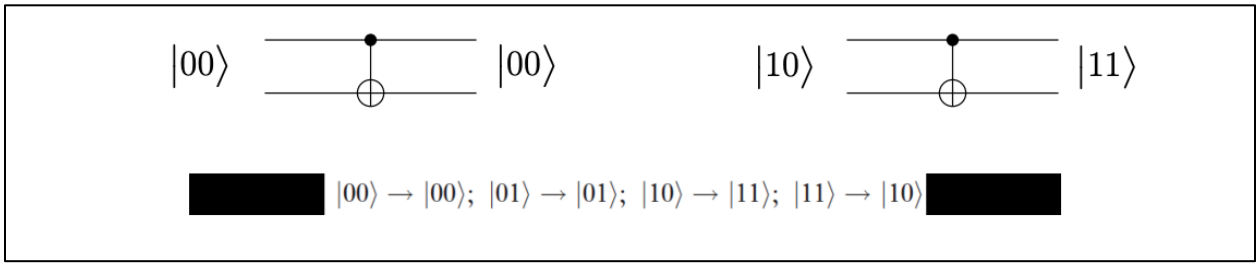


Figure 6.7: Gate operation of the CNOT-gate

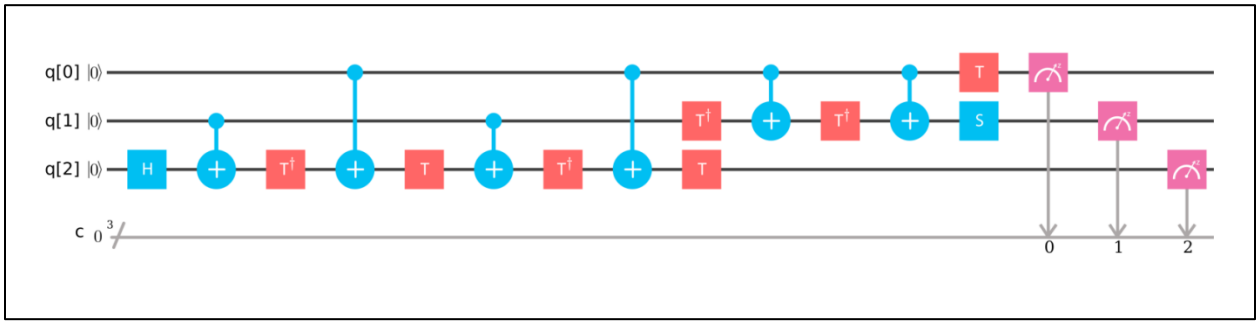


Figure 6.8: Typical 3 qubit gate sequence on an IBM composer.

A quantum algorithm depends on the available qubits and also on how those qubits are connected (see **Figure 6.8** for a typical quantum circuit). Different models of quantum computers may do it differently. Decoherence is another major issue in quantum computing. One cannot expect to pause a running program. Once the run button is hit the program must finish quickly before the quantum information is decayed. Actually the metric of interest specifies the ratio of coherence time/single gate operation time. Precision and errors remain an issue for quantum computing. As indicated above, different qubits have different gate error and readout error. Gate error is about the precision in applying a quantum gate. i.e. how accurate can we control the superposition? Readout error is the error in measuring qubits. There is no simple agreed upon formula that fully describes the power of a quantum computer.

All that can be said is that the higher the qubit count, quality level, and connectivity, the better. The quality of the quantum computers can be measured by the relaxation time (T1), coherence time (T2), readout errors, and gate errors. Quantum computers are built out of qubits. But just having lots of qubits is not enough. A billion qubits working in complete isolation will never achieve anything. They need to talk to each other. This means that the need to be connected by so-called controlled operations. Every device has its own rules for which pairs of qubits can be connected in this way. The better the connectivity of a device, the faster and easier it will be for us to implement powerful quantum algorithms**.**

The nature of errors is also an important factor. In the near-term era of quantum computing, nothing will be quite perfect. So we need to know what kinds of errors will happen, how likely they are, and whether it is possible to mitigate their effects in the applications we care about. These are the three most important aspects of a quantum device: qubit number, connectivity and noise level. To have any idea of what a quantum computer can do, you need to know them all. A lot of work has been done in quantum computation since the field started in the ’80s. Many generations of theoretical physicists have proposed and improved quantum algorithms, but most of them have not been tested in real devices. It is a good moment to check the literature and push these works into the open. We are living through an amazing period, witnessing the birth of a technology that involves the creation of a new paradigm in computation. In my opinion, the opening of the experiments and their programming tools to everybody not only democratizes science but also boosts its progress. The IBM Q platform is one such effort.

6.4 Hybrid qubits implementation on IBMQX4

IBM has developed prototypes of 5-, 16-, 20- and 50-qubit quantum computer, which has attracted the attention of a large number of researchers working in various sub-field of quantum computation and quantum information. A number of experiments have been tested and verified using 5-qubit and 16-qubit quantum computer. For this work we used IBM’s 5 qubit quantum processor. ‘**ibmqx4**’ shown in **Figure 6.9** to demonstrate the working of a hybrid quantum simulator. We entangle a superconducting qubit and an NV centre. The information about the entangled state can be retrieved by using an ancilla representing another superconducting qubit.

Demonstrating entanglement in hybrid systems is important because it's likely that a resilient quantum computer will combine different qubit systems. Further, entanglement gives quantum computing its special power of parallel processing and storage. Since the introduction of quantum mechanics, it has been taught mostly as a theoretical subject. It is also viewed as a theory that provides a best understanding of the nature, but which does not have much practical applications in our day to day life. This notion has been considerably changed in the recent past with the advent of quantum information processing and availability of online quantum platforms. In this thesis, we will show that the IBM quantum computer can be used to demonstrate fundamental concepts of quantum mechanics, quantum computing and communication.

6.5 Mapping physical system on physical chip

The interaction between the superconducting flux qubit and the NV centre can be implemented in a digital way using CNOTs, which connect central qubit with four others. Realising entanglement is not a straight forward exercise due to decoherence and depolarization which are difficult to manage in real quantum devices. The electron spin and ^{14}N either do not interact with each other directly or do interact: additional CNOTs between Q3 and Q4 as well as between Q0 and Q1 can be used to implement digitally pairwise interaction of corresponding spins, whose quantum states are encoded into these four qubits.

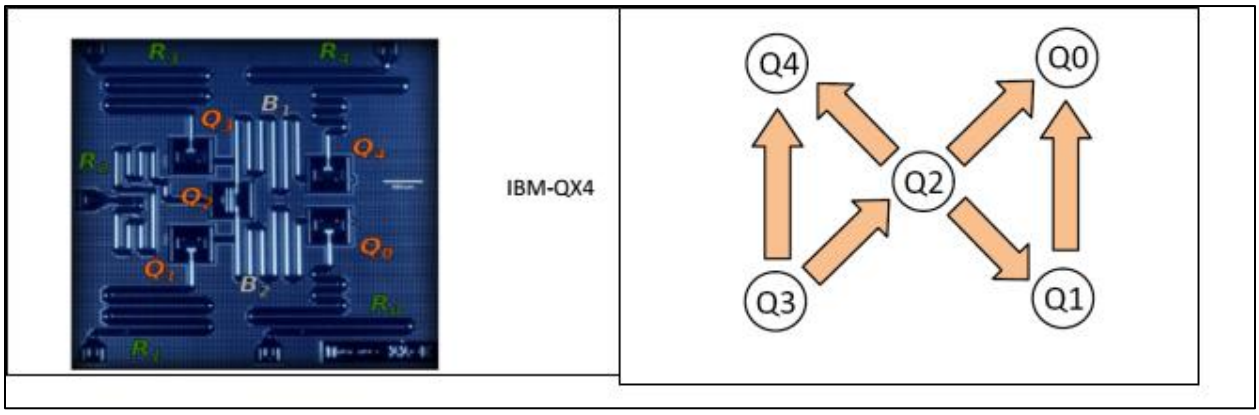


Figure 6.9: Schematic view of IBMqx4 chip. Two qubit gates and their directions are shown by arrows.

We are going to analyze the dynamics starting from initial conditions which is unexcited electron spin and unexcited spin of the ^{14}N. The IBM Q chip architecture can be viewed as a central spin model combined by a bosonic system. The central spin models are usually used reliably to study decoherence processes in quantum dots and other systems. In real physical systems, particles have their own environments. However, influence of these additional baths can be neglected within some initial time interval during the free evolution, provided the coupling to the central spin is larger. The electron spin is initialized and entangled with the flux qubit for computation and read out as in **Figure 6.10**. Using a different frequency the electron spin can now be entangled with a ^{14}N nucleus in order to simulate storage. The electron spin is thus effectively used as a quantum bus.

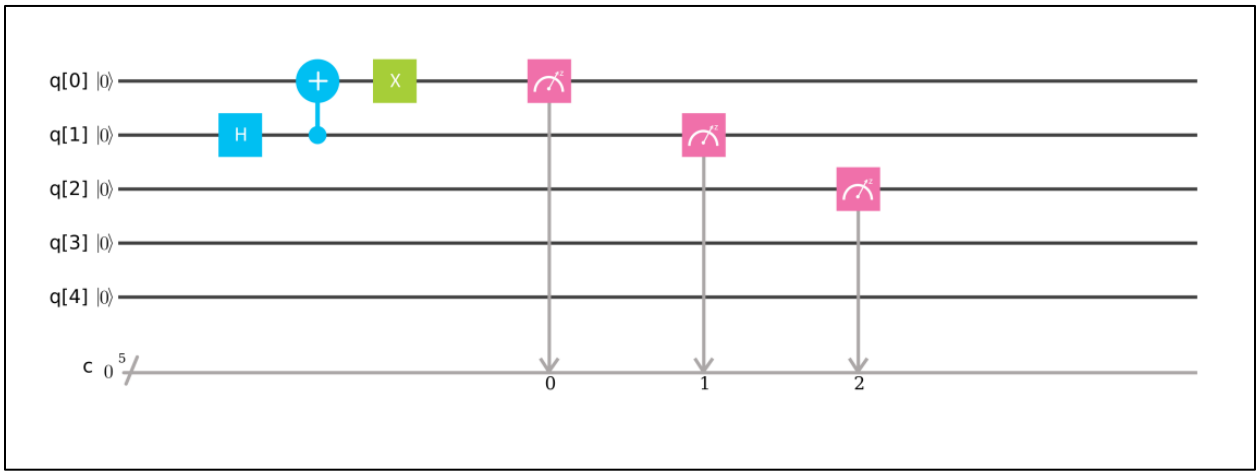


Figure 6.10: Entanglement with bit flip (SWAP).

Chapter 7

Results and Analysis

7.1 Simulation set-up

Nitrogen-vacancy centers in diamond and superconducting flux qubits are ideal platforms for quantum simulation, which allows one to handle problems that are intractable theoretically or experimentally **[86]**. Here we propose a digital quantum simulation scheme to simulate the quantum decoherence occurring in nitrogen doped thin films placed in a parallel magnetic field due to a gap tunable flux qubit as shown in **Figure 7.1**. The quantum simulator employs high quality superconducting and spins qubits achievable in nitrogen-vacancy centers and can be realized with existing technology. The coupling strength between two physical systems is the key factor necessary for quantum memory operation in hybrid systems because the time taken to transfer information between the systems is inversely proportional to the coupling strength, so faster operation within its coherence time leads to high-fidelity operation. Entanglement is a direct measure for effective coupling.

The problem can be mapped onto the Hamiltonian of three entangled qubits represented by the flux qubit, electron and nuclear spins **[77]** as shown in **Figure 7.2**. The simulation uses the Trotter algorithm, with an operation time of the order of 100μs for each individual run. Demonstrating how the fidelity of the spin centre varies with perturbation from the ^{13}C nuclear spins around it. Variation in surroundings will influence when central spin has high fidelity.

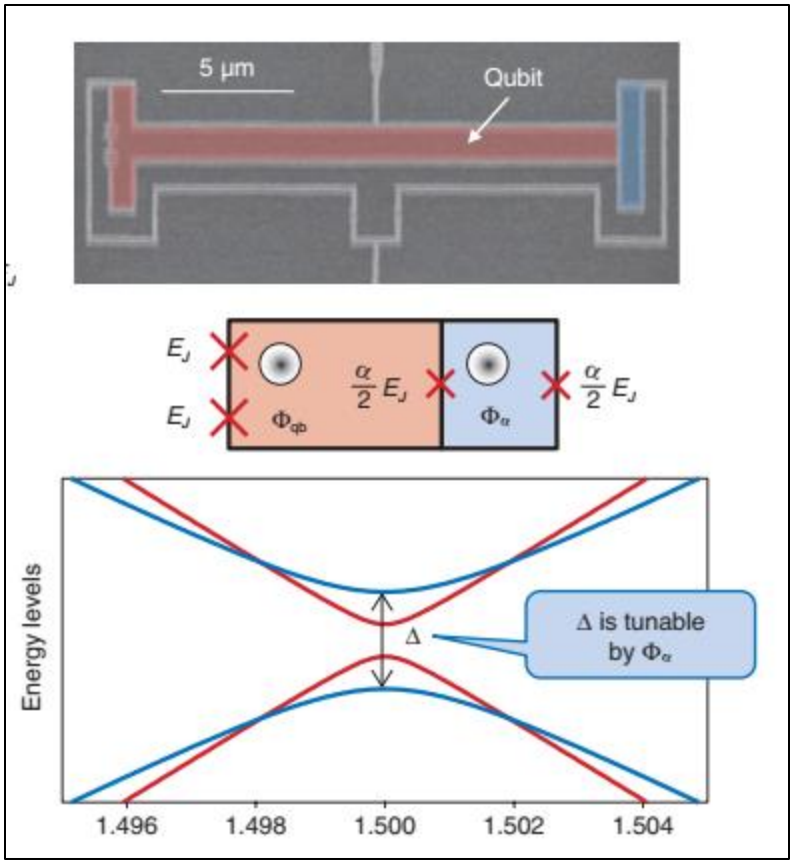


Figure 7.1: Gap tunable superconducting flux qubit and its energy levels

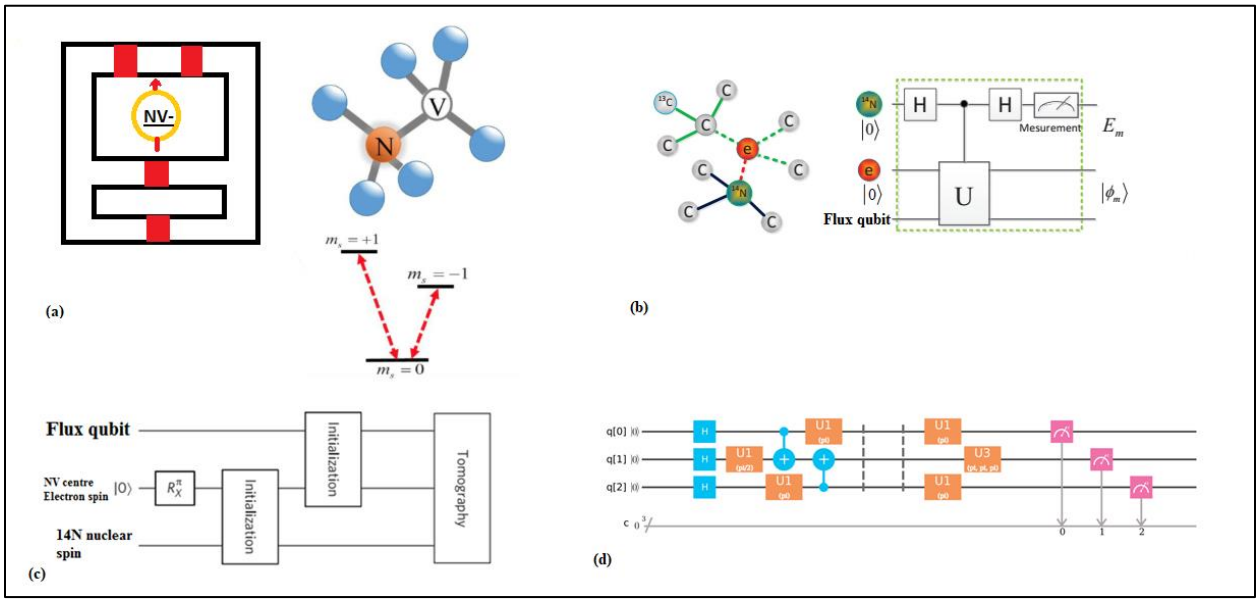


Figure 7.2: (a) NV center coupled to a superconducting flux qubit consisting of four Josephson junctions in red, crystal-lattice and energy diagrams of an NV center in diamond. (b) Nitrogen-Vacancy center in diamond. (b) The Quantum circuit describing the simulation. (d) Two qubit

control and flux qubit-nuclear entangling gate.

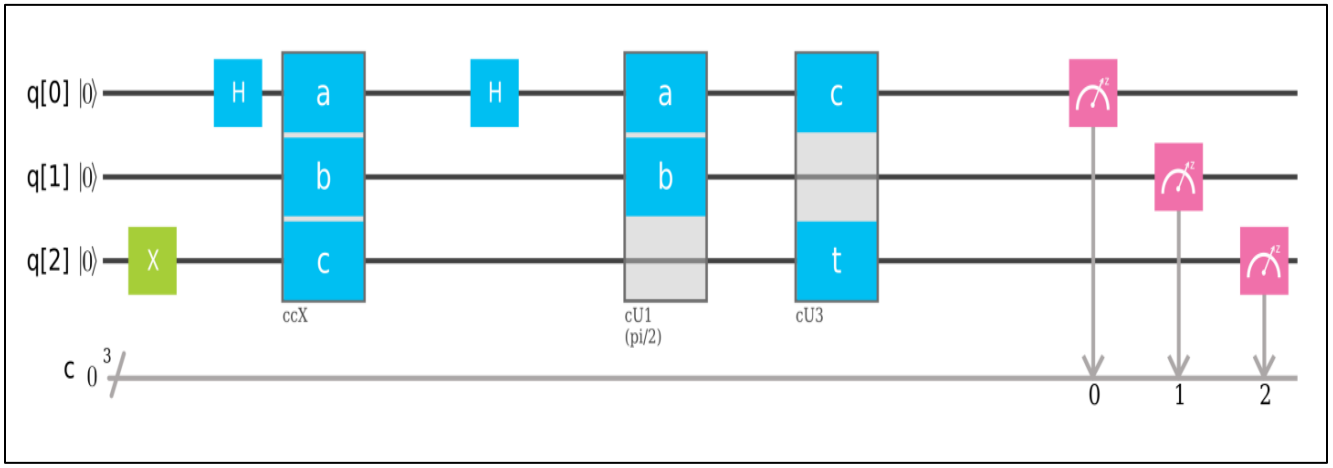


Figure 7.3: Unitary gates generated from the Trotterisation of ***Equation 53****.*

An unpaired electron on the center form an effective electron spin with a spin triplet ground state (S=1). The nuclear spin of the substitutional ^{14}N atom is also employed in our simulation. The ^{13}C atom is the source of decoherence. The Hamiltonian of the two spins and flux qubit in an external magnetic field B_0 is ($\hbar$= 1)

$$H_0 = \{DS_Z^2 + \gamma_e B_0 S_Z - \gamma_C B_0 C_Z\} - \{FQ\} + \{J_C S_Z C_Z + J_N S_z FQ\} \qquad \textbf{(53)}$$

Here $S_z, C_z, and\ N_z$ are operators for the electron spin, 14N nuclear spin and flux qubit, respectively. **D/2π=2.87 GHz** is the zero splitting tensor of the electron spin which originates from the anisotropic magnetic dipole-dipole interaction between the two unpaired electrons of the NV centre in diamond. The second to fourth terms are the Zeeman interactions of each spin with the gyromagnetic ratio$\gamma_e/2\pi = 2.8MHz/Gauss, \gamma_C/2\pi = 1.1kHz/Gauss,$ $\gamma_N/2\pi = 0.3077\text{kHz/Gauss}$. **$B_0$** is an external magnetic field used to manipulate the 3-qubit system. Q/$2\pi = -5.1MHz$ is the quadrupole splitting tensor of the nitrogen nuclear spin. The hyperfine coupling constant between the electron spin is selected to be $\mathbf{J_C/2\pi = 14MHz}$ to fulfill the parameter relations in this particular simulation. The hyperfine coupling constant between the electron spin and the 14N nuclear spin is **J_N/2π=2.1MHz**. The unitary gates produced from Trotterisation of **Equation 53** are shown in **Figure 7.3**.

Besides the spin of the nitrogen host, the NV electronic spin also couples to ^{13}C nuclear spins (I = 1/2) in the environment. In non-purified diamond, the ^{13}C isotope occurs with a natural abundance of 1.1% within the otherwise spin-free ^{12}C material, and the resulting spin bath is to a large extent responsible for the dephasing of the electronic spin31. However, individual ^{13}C atoms that are located only a few lattice sites away from the NV center experience a strong hyperfine interaction, and are usable as qubits. The flux qubit is used to encode the τ pseudospin, and the ^{14}N nuclear spin is the readout spin. The simulation consists of a quantum algorithm of finding eigenvalues. The procedure is illustrated in **Figure 7.2(b**). At the beginning, the ^{14}N nuclear spin is prepared in |0>. The electron spin and flux qubit are prepared in an arbitrary state |0>. Appropriate microwave (MW) and radiofrequency (RF) pulses would prepare the electron spin and ^{14}C nuclear spin into the state |0>.

The simulation is premised on this experiment being performed in a wet dilution refrigerator capable of achieving a base temperature of 15mK. Qubit frequencies are chosen to be in the 4.8-5.5GHz range with exact frequencies optimized per qubit based on desired state and spectra. Typical gate errors are assumed to be 0.03 for the spins and 0.05 for the flux qubit. Obtained gate fidelities for the entangled qubits range from 0.5 to 0.97 depending on the number of implementation steps and duration of sequences. Lifetimes up to 5 microseconds were obtained.

We determine their fidelities experimentally, using a nuclear spins as qubit and a different nuclear spin system as the noisy environment. We consider a system qubit S, which is coupled to a noisy environment via a dephasing interaction HSE = $b(t)S_Z$, (1) where the (semi-)classical field b(t) has a finite correlation time τ_c. Dynamical decoupling by sequences of inversion pulses can suppress the dephasing effect of this interaction and prevent the decay of the coherence in the system **[87]**. This is well explored in the context of quantum memories, where the goal is to keep a specific quantum state unchanged. Here the effect of DD can be roughly described as a prolongation of the dephasing time T2. In the case of quantum computing, the goal is not the preservation of a quantum state, but the precise control of a quantum system such that it evolves along a well-defined path in Hilbert space.

7.2 Entanglement

An important application of NV centers that can now be realized is quantum simulation. Quantum simulators like IBMQx4, which serve as pure quantum systems, offer an exciting pathway towards problems that cannot be solved theoretically or tested experimentally.
Is a quantum system coupled to a thermal environment capable of generating entangled states? A demonstration of entanglement is considered to be a critical milestone for any approach to building a quantum computing technology. Herein, we demonstrate a digital method to detect entanglement. Occupation of the two states of interest can be tested and interpreted (^{14}C and flux qubit being controlled by the NV centre-when the |000> and |111> show equal probabilities then entanglement is demonstrated).

Here we analyze the dynamics starting from initial conditions which is unexcited electron spin and unexcited spin of the ^{14}N. All quantum gates are initialized to the unexcited state on the IBM quantum processor. For this experiment, the IBM Q chip architecture can be best viewed as a central spin model linked to a bosonic system. The central spin model is usually relied upon to study decoherence processes in quantum dots and other systems. Dynamics are highly sensitive to frequency as shown in **Figure 7.4**(a). This sensitivity proves the occurrence of entanglement and quantum superposition in the device. These results support the view that excitation can be restricted to the nuclear spin or flux qubit thereby enabling storage and accurate computation. The electron spin is initialized and entangled with the flux qubit for computation and read out. Using a different frequency scheme the electron spin can now be entangled with a ^{14}N nucleus in order to simulate storage. The electron spin is thus effectively used as a quantum bus in this simulation. Further work can be done where the coupling between the electron spin and flux qubit is employed to detect the hyperfine structure of the NV center.

Flux qubits (FQs) form superpositions of persistent currents of hundreds of nano-Amperes, flowing clockwise and anti-clockwise through micrometer-sized SC loops. The magnetic field associated with this current, of the order of a μT, enables a magnetic dipole coupling to the electron spins associated with crystalline impurities such as the NV center in diamond.

Of particular interest is the coincidence of energy splittings: the two states of the FQ are typically separated by a few GHz, while NV centers have a S = 1 ground state, with zerofield splitting Δ = 2π × 2.87 GHz between the mS = 0 and mS = ±1 states. By the application of a mT magnetic field, one of the spin transitions of the NV center can be tuned into resonance with the FQ. Consider a single NV center in a diamond crystal, located near a square FQ. The coupling constant g depends on the field perpendicular to the NV axis. The coupling depends on the size of the loop as given by the Biot-Savart law and the number of NV center ensembles, N. Even though the FQ coherence times are much shorter than the coupling to a single NV center, it is possible to coherently transfer the quantum-state from the FQ to an ensemble of many (N) NVs by benefiting from a √N enhancement in the coupling constant. In our case N=1 and this effect is not observable. The √N arises because in the regime of weak excitation the spin operators of an NV center with large N can be mapped into bosonic operators via Holstein-Primakoff (HP) transformation **[88]**.

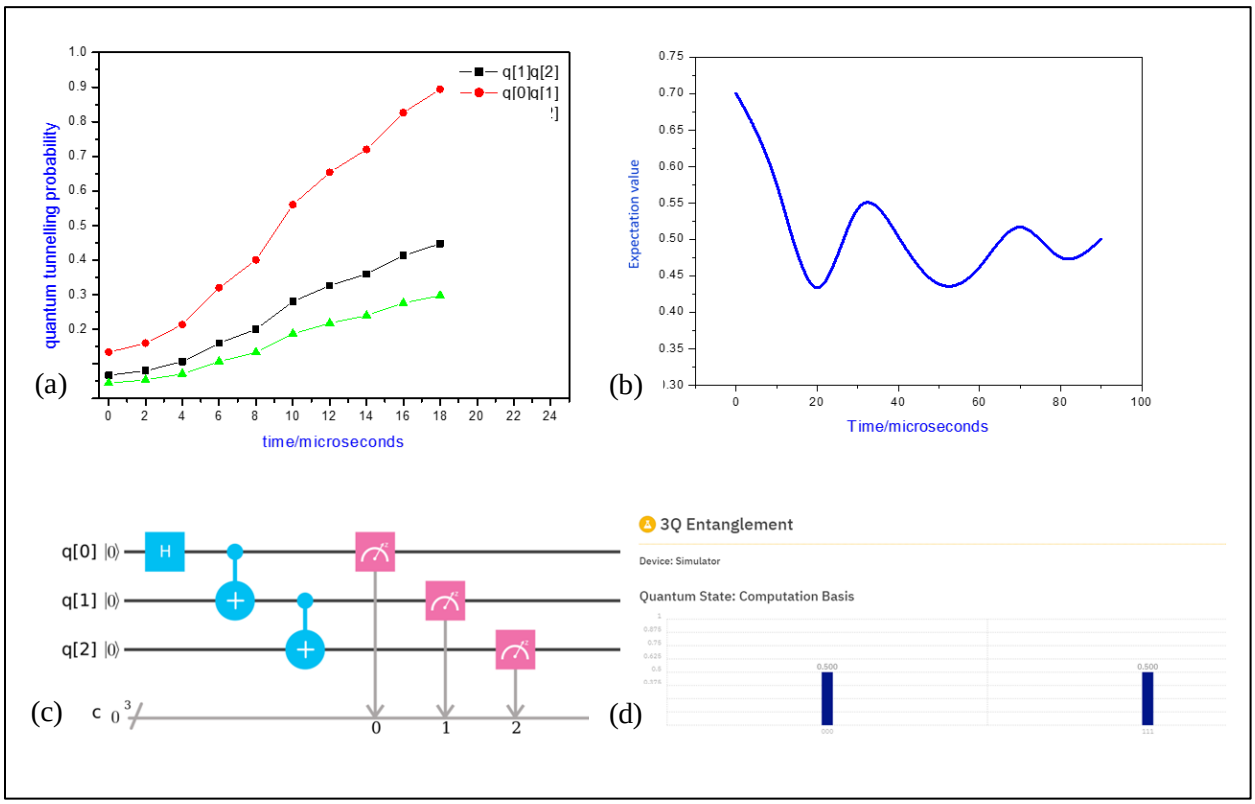


Figure 7.4: (a) Probability of quantum tunneling involving the different qubits at different frequencies. Successful quantum tunneling leads to entanglement. (b) Expectation values for

central spin within a 100μs pulse. (c) Quantum circuit used to simulate entanglement. (d) IBMqx4 simulator output to confirm entangled gates.

7.3 Decoherence

The electron spin of the NV center is always coupled to the nuclear spin of its own nitrogen atom (**Figure 7.5a**). The NV center is therefore an intrinsic, hybrid 2- qubit system. Effectively coupling this system to a flux qubit builds a hybrid quantum computer. The problem is thus mapped onto the Hamiltonian of three entangled qubits represented by the flux qubit, electron and nuclear spins. **Figure 7.5** demonstrates how the spin center decoheres as it is perturbed by the ^{13}C nuclear spins around it. Decoherence of the physical qubit also significantly contributes to the time scale of a single run of the algorithm. Variation in surroundings will influence when central spin has high fidelity. The electron spin is highly occupied in the excited state when disentangled to either the nuclear spin or flux qubit as theoretically expected.

In the realistic implementation of the scheme, decoherence due to the unwanted electron spin-environment coupling is the major limitation of the simulation accuracy. One needs to accomplish the simulation as fast as possible compared to the electron spin decoherence time. NV centers are among the most promising spin qubits in solids, having quite long coherence times even at room temperature.

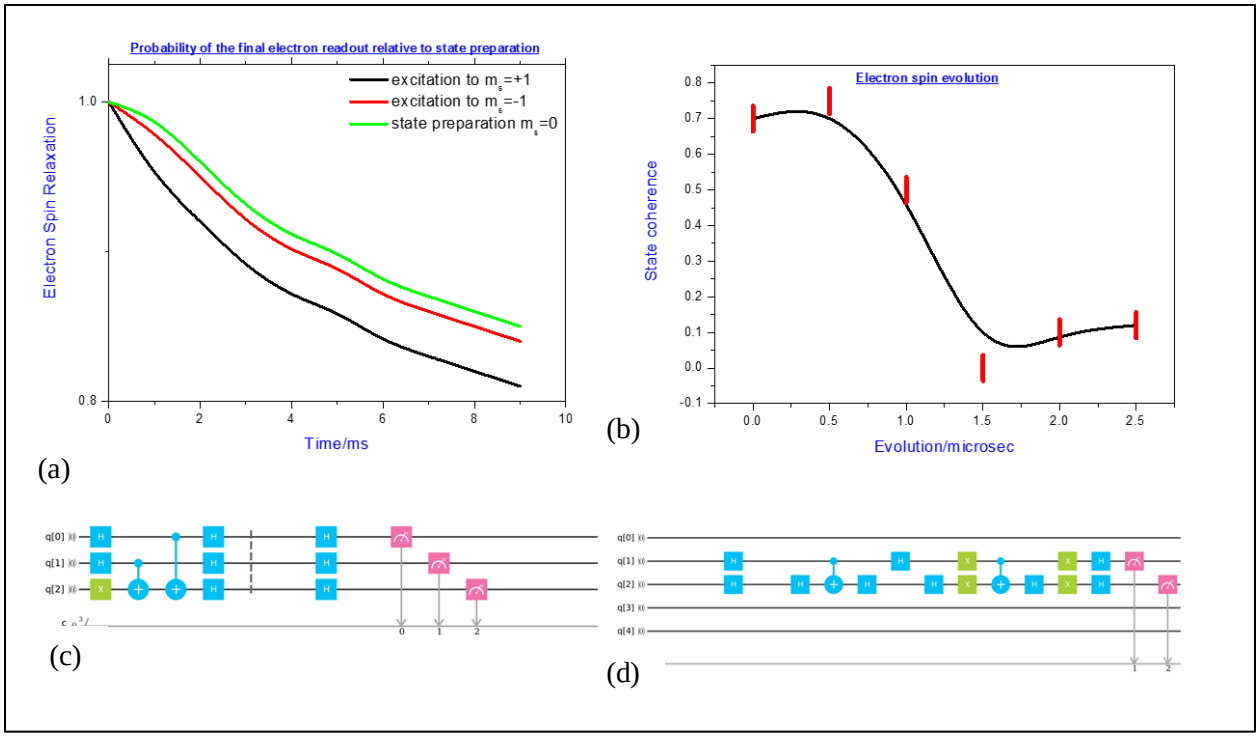


Figure 7.5: (a) Three-qubit entangled system relaxation profile as a function of pulse duration. (b) Decoherence variation with time for three-qubit entangled system. (c) Quantum circuit used to simulate central spin relaxation and (d) entangled spin evolution.

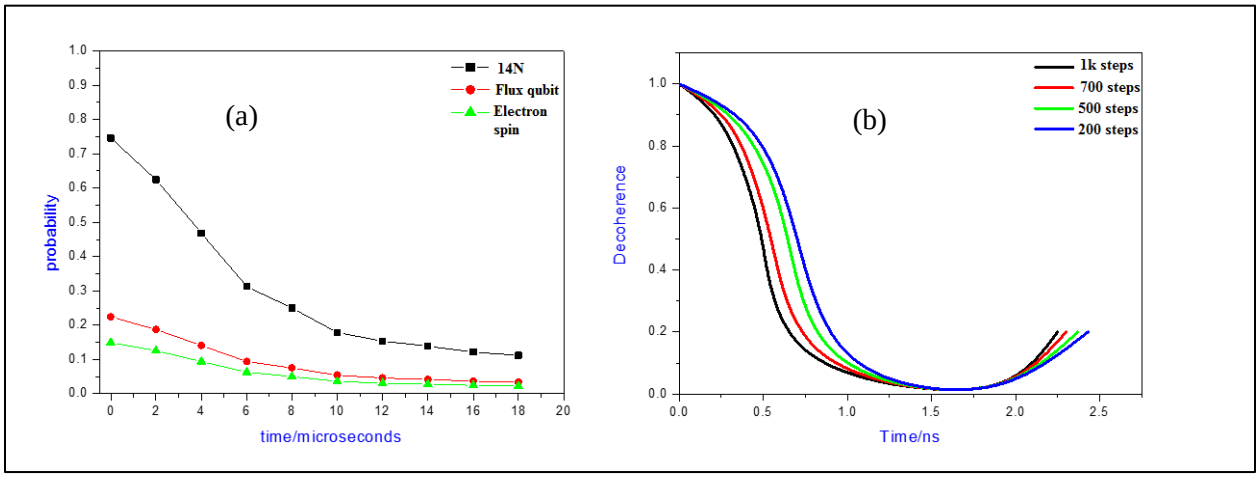


Figure 7.6: (a) Entangled electron spin decoherence. Pulses have to be faster than the time scale shown in order to be effective. (b) Flux qubit decoherence with number of executed steps.

Figure 7.6 shows the decoherence profile of the three qubit system. Current feasible values for the IBM Q platform that were considered in the measurement of decoherence are operation time order of 100μs and a frequency range between 4.8GHz and 5.5GHz.

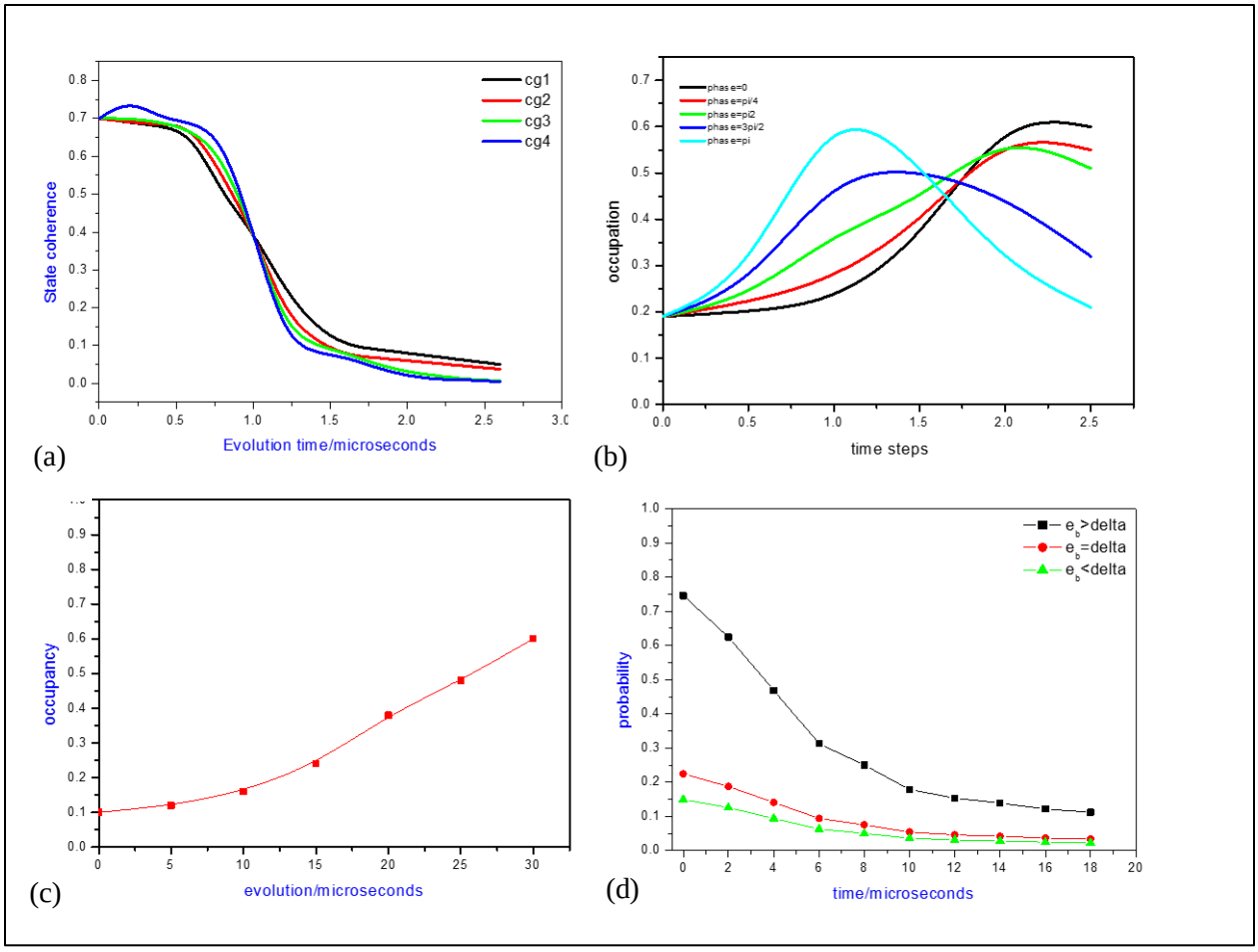


Figure 7.7: (a) State coherence of the flux qubit. (b) The mean population of the excited state of the electron spin as a function of time. Different curves show the different coupling constants between gates. (c) The occupancy of the electron spin after initialization. (d) Expectation values variation with time after excitation of the central spin.

The time evolution of the electron spin of the NV center through initialisation, computation and readout is shown in **Figure 7.7**.

7.4 Gate fidelity

The slow decay of the electron spin may be used to indicate high gate control fidelities (see **Figure 7.8**). Together with the electronic spin of the vacancy, hyperfine-coupled nitrogen and possibly carbon nuclear spins found in the vicinity can form a quantum register of several qubits. In such a register, the nuclear spins with their excellent coherence times would serve as quantum memories accessed via the more directly controllable electronic spin of the vacancy.

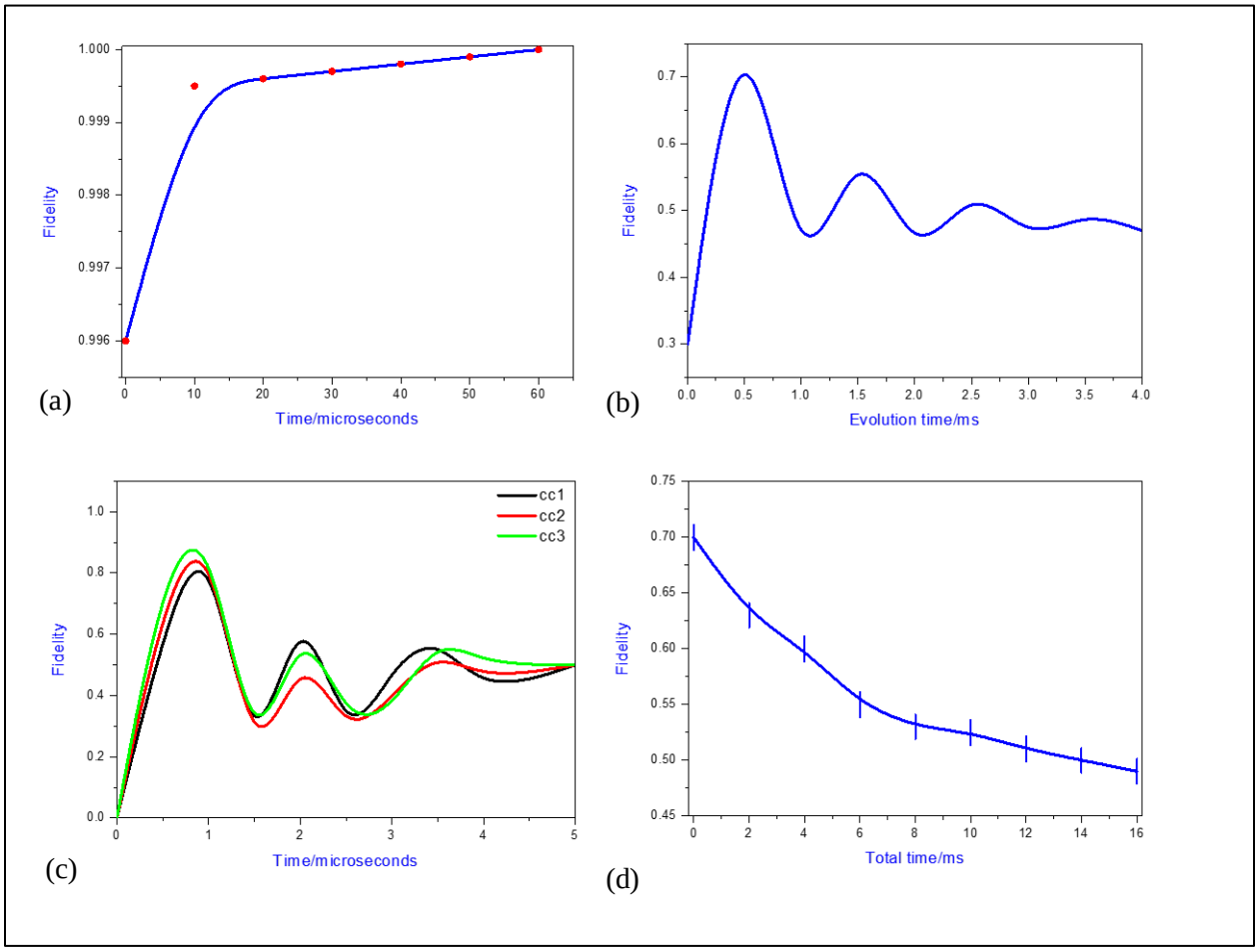


Figure 7.8: (a) Ground state gate fidelity of central spin. (b) Overview of fidelity evolution for a three qubit entangled hybrid system. (c) Fidelity evolution for different coupling constants between quantum gates. (d) Characterization of the conditional gate for electron spin in entangled state.

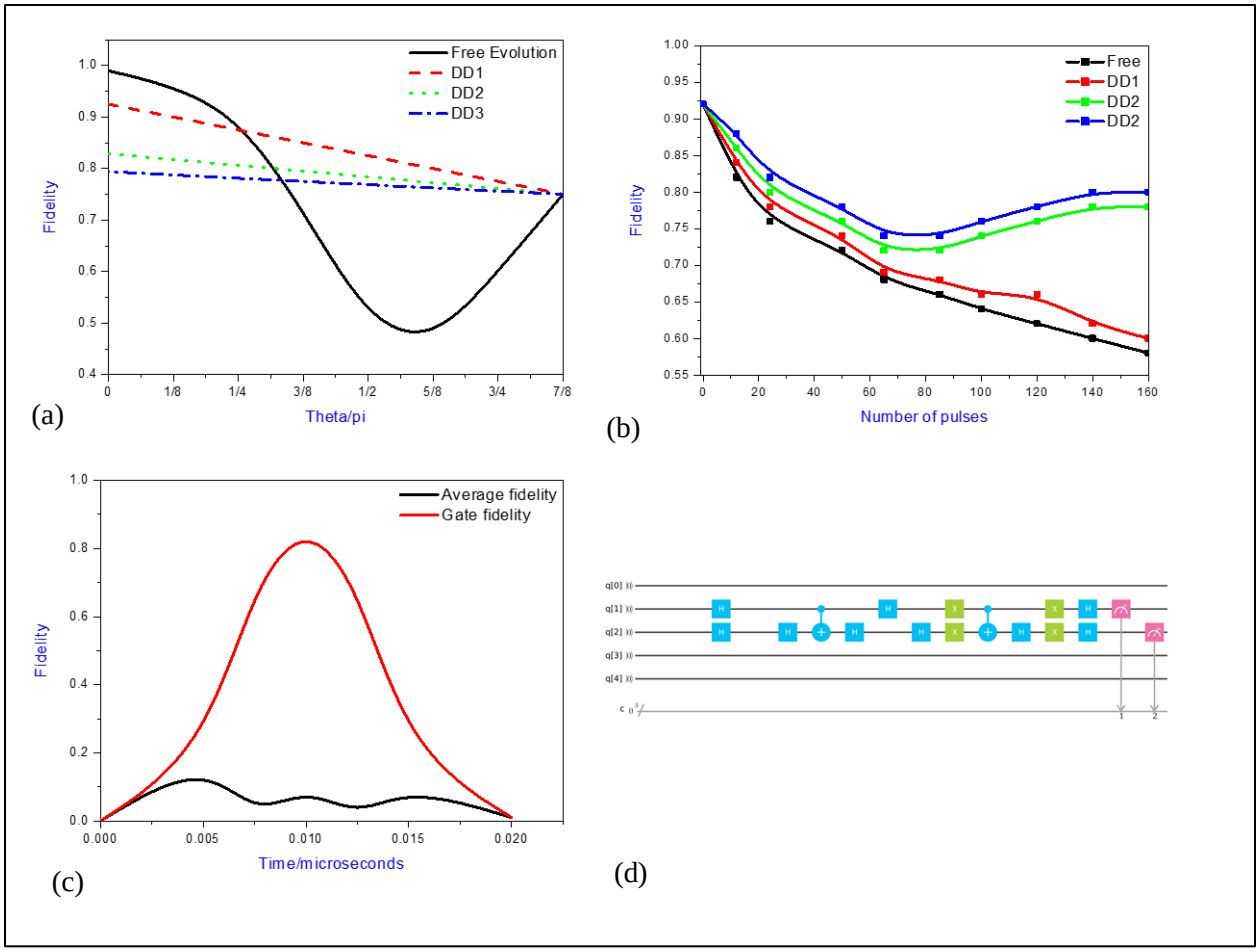


Figure 7.9: (a) Process fidelities for different schemes on applying dynamic decoupling. (b) Fidelity evolution as the number of gate pulses is increased to measure impact of errors. (c) A comparison of gate fidelities for different gate combinations. (d) Quantum circuit to simulate dynamic decoupling algorithm for the three qubit gates.

Figure 7.9 shows process fidelities for the three-qubit when dynamic decoupling is applied. Gate fidelity improves from free evolution to DD3 which is when the decoupling is optimized. However, as the number gates is increased the pulses last longer in the composer and the quantum scores get poorer, i.e. lose their fidelity.

Analysis

The goal of this work is to digitally demonstrate the coupling of the electron and nuclear spins given their excellent coherence times with superconducting flux qubits chosen for their excellent anharmonicity and ability to effectively combine with other systems. The defect electron spin in the NV center enables initialization and readout of the register and coupling to other (distant) electron spins whereas the nuclear spins provide well-isolated qubits and memories with long coherence times.

In our work the electron spin of a nitrogen-vacancy center in diamond is employed to initialize, control and readout a carbon-14 spin and perform computation on a flux qubit. Hybrid control is realised over a 1-qubit spin register by harnessing nitrogen-14 nuclear spin in an NV center. This approach can be used to construct high-fidelity multi-qubit gates. The coupling strength between two physical systems is the critical factor necessary for quantum memory operation in hybrid systems because the time taken to transfer information between the systems is inversely proportional to the coupling strength, so faster operation within its coherence time leads to high-fidelity operation.

Our work can be extended to NV ensembles in order to demonstrate multi-qubit resilience. The implementation of surface code algorithms to test the scalability of the system will go a long way in developing this approach of a hybrid quantum system. Quantum computers must be able to function in the presence of decoherence. A common strategy for decoherence reduction is dynamical decoupling (DD), which requires no encoding overhead and works by converting quantum gates into decoupling pulses. This approach can be considered to improve gate fidelities. This work demonstrates that quantum registers of nuclear spins coupled to electron spins of individual solid-state defects and superconducting qubits offer a promising mechanism for quantum information processing. To progress towards large-scale applications, larger and deterministically available nuclear registers are highly desirable.

Future work can explore the use of the 13C nuclei to do error correction thus turn them from a nemesis to a reliable partner in developing quantum communication protocols and algorithms. Challenges like gate errors and decoherence processes emanating from temperature fluctuations, vibrations and possible radio frequency interferences still remain. There are still limitations on how the qubits can interact.

Chapter 8

Conclusions

The objective of this work was to present and explore diamond as a quantum material. **Part 1** investigates quantum phase transitions in boron-doped diamond thin films with a view to building quantum hardware like resonators for circuit quantum electrodynamics. **Part 2** demonstrates how nitrogen doped diamond is useful as a spin qubit which is suitable for building a resilient hybrid quantum system. Results obtained during simulation in **Part 2** support the feasibility of a robust quantum computer based on a hybrid architecture made up of NV centers as qubits and boron-doped diamond resonators. Quantum registers of nuclear spins coupled to electron spins of individual solid-state defects and superconducting qubits offer a promising mechanism for quantum information processing. The 3-qubit system of the NV center and flux qubit shows excellent performance in entanglement, decoherence, and fidelity. There is effective coupling amongst the qubits that evolves from weak to strong.

Quantum simulation can now be done efficiently on the IBM Q platform despite limitations in actual device architecture. Some qubits cannot currently be linked through quantum gates like the CNOT-gate. This is because the IBM Q 5-qubit processor is wired in a way that limits the gate combination one can do.

Decoherence is another major issue in quantum computing. The results on coherence can be improved in the future by implementing a dynamical decoupling (DD) protocol. Further, this work paves the way for a future where it may be possible to consider using 13C nuclei to do error correction. Other considerations to be made are; extending work to NV ensembles in order to improve coupling from strong to ultrastrong, exploration of indirect coupling of transmon qubit and NV center, demonstration of other algorithms to simulate multipartite entanglement. The IBM Q platform is a good test bed for ideas in quantum information processing.

Our analysis in **Part 1** suggests that the mechanism of SIT in HBDD thin films can split into two: a superconducting phase where Cooper pairs are condensed and vortices are localized, and

an insulating phase, where Bose-condensed vortices are delocalized, and electron pairs are localized. This proves that HBDD thin films are a tunable platform that can be considered seriously for quantum technology. Future PhD work may be done to actually make a device out of boron-doped diamond and characterise it at high frequencies using a Vector Network Analyser (VNA).

Many ideas for future consideration arise from this work. We do not have adequate knowledge about the thin films at the temperatures required for quantum computation, i.e., 10-20mK. There is a need to characterize HBDD thin films at much lower temperatures only possible in a dilution refrigerator. It is also crucial to know whether our films are anisotropic or isotropic through rotating probe measurements for angle dependence. A current-biased four terminal measurement with an accuracy down to mΩ is required in order to identify the dominating mechanism of SIT between charge and vortex BKT. While no doubt is left about the very existence of a quantum superconductor-insulator transition, and how it is influenced by material characteristics (such as the film thickness, disorder, and charge-carrier concentration), a magnetic field has also been shown to play the role of a control parameter. The outstanding question is rather why the transitions in various materials occur in different scenarios and what factors determine which of the scenarios is realized.

This work is inspired by the need to contribute to the construction, characterization, validation, and verification of quantum processors and simulators. At best it is hoped that this work motivates other academics to make use of online resources being made available by IBM and others to explore and learn. Other experimental groups are also challenged to share their hardware to expedite testing and development of technology and ideas.

References

[1] Qiu, Y. et al., Four-junction superconducting circuit, Sci. Rep. vol. **6**, 28622, 2016.

[2] Bar-Gill, N. et al. Solid-state electronic spin coherence time approaching one second. Nat. Commun. 4:1743, 2013.

[3] Shor, P. W Scheme for reducing decoherence in quantum computer memory. Physical review A, 52(4):R2493, Oct 1995.

[4] Childress, L., & Hanson, R. Diamond NV centers for quantum computing and quantum networks. MRS Bulletin, vol. 38 no. 2, 2013, pp.134-138.

[5] Dowling, J. P & Milburn, G. J. Quantum technology: the second quantum revolution, Philosophical Transactions of the Royal Society of London. Series A: Mathematical, Physical and Engineering Sciences, 2003, pp. 361.

[6] Schleier-Smith, M., Editorial: Hybridizing Quantum Physics and Engineering, Phys. Rev. Lett. 117, 100001, 2016.

[7] Bardeen, J.; Cooper, L. N.; Schrieffer, J. R., Theory of Superconductivity, Physical Review, vol. 108, no. 5, 1957, pp. 1175–1204.

[8] Bulaevskii, L. N., Sadovskii, M. V., Anderson Localization and Superconductivity, Journal of Low Temperature Physics, vol. 59, no. I/2, 1985.

[9] Saito, Y. et al., Quantum phase transitions in highly crystalline two-dimensional superconductors, Nature, vol. 9, no. 778, 2018.

[5] Bhattacharyya, S. et al., Non-s wave superconductivity in boron-doped nanodiamond films with 0-π Josephson junction array, 2007.

[6] Bhattacharyya, S., Coleman, C., Observation of the Berezinskii-Kosterlitz-Thouless transition in Boron-doped diamond films, AIP Advances, vol. 7, no. 115119, 2017.

[7] Bouadim, K. et al., Single- and two-particle energy gaps across the disorder-driven superconductor-insulator transition, Nat Phys, vol. 7, 2011, pp. 884-889.

[8] Blatter, B.,et al., Vortices in high-temperature superconductors, *Rev. Mod. Phys.*, vol. 66, no. 1125, 1994, pp. 1388.

[9] Saito, Y. Nojima, T., & Iwasa, Y., Highly crystalline 2D superconductors, Nature Reviews Materials, vol. 2, no. 16094. 2016.

[10] Kosterlitz, J. M.; Thouless, D. J., Ordering, metastability and phase transitions in two-

dimensional systems, Journal of Physics C: Solid State Physics, vol. 6, no. 7, 1973, pp. 1181–1203.
[11] Sachdev, Subir, Quantum Phase Transitions, 2011. (Cambridge University Press).
[12] Baturina, T. I. Strunk, C. Baklanov, M. R. and Satta, A., Quantum Metallicity on the High-Field Side of the Superconductor-Insulator Transition, Phys. Rev. Lett, vol. 98, no. 127003, 2007.
[13] Schick, M., Two-dimensional system of hard-core bosons, Phys. Rev. A, vol. 3, no. 3, 1971, pp. 1067–1073.
[14] Rabatin, B., and Hlubina, R., Superconductivity in systems exhibiting the Altshuler-Aronov anomaly, Phys. Rev. B, vol. 98, no. 184519, 2018.
[15] Inui, M. et al., Pinning and thermal fluctuations of a flux line in high-temperature superconductors, Phys. Rev. Lett, vol. 63, no. 2421, 1989.
[16] Eley, S. et al., Universal lower limit on vortex creep in superconductors, Nature Materials, vol.16, 2017, pp. 409–413.
[17] W. J. Skocpol, M. R. Beasley, and M. Tinkham., Phase-slip centers and non-equilibrium processes in superconducting tin microbridges, Journal of Low Temperature Physics, vol. 16, no. 1, 1974, pp. 145–167.
[18] Ortu~no, M., et al., Electronic transport in two-dimensional high dielectric constant nanosystems, Scientific Reports, vol. 5, no. 9667, 2015.
[19] Altshuler B L, Aronov A. G., Electron – electron interaction in disordered conductors in Electron – Electron Interactions in Disordered Systems, 1985.
[20] Dahlem, F., et al., Spatially correlated microstructure and superconductivity in polycrystalline boron-doped diamond. Physical Review B, vol. 82, no. 3, 2010.
[21] Mtsuko, D., Nesladek, M. and Bhattacharyya, S., Finite bias dependent evolution of superconductor-insulator transition in nanodiamond films, 2016.
[22] Zhang, G., Zeleznik, M., Vanacken, J., May, P.W. and Moshchalkov, V.V., Metal–bosonic insulator–superconductor transition in boron-doped granular diamond. Physical Review Letters, vol. 110, no. 7, 2013.
[23] Sachdev, S., Quantum criticality: competing ground states in low dimensions. Science, vol. 288, no. 5465, 2000, pp. 475-480.
[24] Sato, M., and Ando, Y., Topological superconductors: a review. Reports on Progress in

Physics, vol. 80, no. 7, 2017.
[25] Hasan, M. Z., and Kane, C. L., Colloquium: topological insulators, Reviews of Modern Physics, vol. 82, no. 4, 2010, pp. 3045.
[26] Gladchenko, S., et al., Superconducting nanocircuits for topologically protected qubits, Nature Physics, vol. 5, no. 1, 2009, pp. 48.
[27] Rosario Fazio, R., and Herre van der Zant., Quantum Phase Transitions and Vortex Dynamics in Superconducting Networks, Physics Reports, vol. 355, 2001, pp. 235–334.
[28] Fogelström, M., Rainer, D. and Sauls, J.A., Tunneling into current-carrying surface states of high-T c superconductors, Physical Review Letters, vol. 79, no. 2, 1997, pp. 281.
[29] Ekin, J.W., Xu, Y., Mao, S., Venkatesan, T., Face, D.W., Eddy, M. and Wolf, S.A., Correlation between d-wave pairing behavior and magnetic-field-dependent zero-bias conductance peak, Physical Review B, vol. 56, no. 21, 1997, pp. 137-46.
[30] Blonder, G. E., Tinkham, M., and Klapwijk, T. M., Transition from metallic to tunneling regimes in superconducting microconstrictions: Excess current, charge imbalance, and supercurrent conversion, Physics Review B, vol. 25, no. 7, 1982.
[31] Dowling, J. P & Milburn, G. J. Quantum technology: the second quantum revolution, Philosophical Transactions of the Royal Society of London. Series A: Mathematical, Physical and Engineering Sciences, 2003, pp. 361.
[32] Schleier-Smith, M., Editorial: Hybridizing Quantum Physics and Engineering, Phys. Rev. Lett. 117, 100001, 2016.
[33] Clarke, J. The Josephson Effect and e/h, America Journal of Physics, vol. 38, no. 9, 1970.
[34] Tavernelli, I., Quantum Computing at IBM, IBM Research – Zurich, 2018.
[35] Preskill, J., Quantum Computing in the NISQ era and beyond, Open Journal for Quantum Science, Volume 2, 2018, pp. 79.
[36] Aguilar, S. E., Quantum theory of Superconductivity, 2016.
[37] DiVincenzo, D. P., The Physical Implementation of Quantum Computation, 2000.(Wiley)
[38] IBM Q experience. https://quantumexperience.ng.bluemix.net/qx/devices. Accessed 31 December 2018.
[39] Nielsen, M. A., A simple formula for the average gate fidelity of a quantum dynamical operation, Physics Letters A, vol. 303, no. 4, 2002.
[40] M. Nielsen and I. Chuang., Quantum Computation and Quantum Information,. Cambridge

University Press, (2000). pp. 28.
[41] IBM Q User Guide available on the link
https://www.quantumexpreience.ng.bluemix.net/proxy/tutorial/full-user-guide
[42] Wikipedia. https://en.wikipedia.org/wiki/Wheat_and_chessboard_problem
[43] Martinis, J. et al., Decoherence of a superconducting qubit due to bias noise, Physical Review. B, Condensed matter vol. 67, no. 9, 2003.
[44] Feynman, R. P., Int. J. Theor. Phys, vol. 21, no. 467, 1982.
[45] Shor, P. W., Polynomial-time algorithms for prime factorization and discrete logarithms on a quantum computer, 1995.
[46] Rivest, R.; Shamir, A.; Adleman, L. A., Method for Obtaining Digital Signatures and Public-Key Cryptosystems. Communications of the ACM. vol. 21, no. 2, 1978. pp. 120–126.
[47] Grover L.K., A fast quantum mechanical algorithm for database search, Proceedings, 28th Annual ACM Symposium on the Theory of Computing, 1996.
[48] Warren, W. S., The usefulness of NMR quantum computing, Science. vol. 27, no. 5332, 1997.
[49] Qiu, Y., A hybrid quantum system: Coupling spin ensembles via superconducting flux qubits, Phys. Rev. A, vol. 89, no. 042321, 2014.
[50] Taminiau, T. H. et al., Universal control and error correction in multi-qubit spin registers in diamond, Nature, 2014.
[51] Lahtinen, V., Pachos, J. K. A., Short Introduction to Topological Quantum Computation, SciPost Phys, vol. 3, no. 021, 2017.
[52] Quantum simulation: From basic principles to applications, Comptes Rendus Physique, 2018.
[53] Semba, K. et al., Coherent Coupling between a Superconducting Qubit and a Spin Ensemble, vol. 478, no. 7368, 2011, pp. 221-4.
[54] Kubo, Y., et al., Strong Coupling of a Spin Ensemble to a Superconducting Resonator, Phys. Rev. Lett. vol. 105, no. 140502. 2010.
[55] Marcos, D., et al., Coupling Nitrogen-Vacancy Centers in Diamond to Superconducting Flux Qubits, Phys. Rev. Lett, vol. 105, no. 210501, 2010.
[56] Twamley, J. & and Barrett S. D., Superconducting cavity bus for single nitrogen-vacancy defect centers in diamond, Phys. Rev. B, vol. 81, no. 241202(R), 2010.

[57] Walter, M. et al., Multi-partite entanglement, arXiv:1612.02437, 2017.
[58] Ghosal, A., Randeria, M., Trivedi, N., Inhomogeneous pairing in highly disordered s-wave superconductors, Phys. Rev. B, vol. 65, no. 1:014501, 2001.
[59] Lloyd, S., Capacity of the noisy quantum channel. Phys. Rev. A, vol. 55, no. 1613. 1997.
[60] Einstein, A., Can Quantum Mechanical Description of Physical Reality Be Considered Complete?, Physical Review., 1935.
[61] Terhal. B. M., Detecting quantum entanglement. Theoretical Computer Science 287, 2002.
[62] Habib, S. et al., Quantum Feedback Control: How can we control quantum systems without disturbing them?, Los Alamos Science. vol. 27. 2002.
[63] Tinkham, M., Introduction to Superconductivity, 1996. (Dover Publications).
[64] Josephson, B. D. The discovery of tunneling supercurrents. Rev. Mod. Phys. vol. 46, no. 2, 1974, pp. 251–254.
[65] Lana, G. A., Quantum Computation with Superconductors, 2016.
[66] Kouichi, S., Entanglement Control of Superconducting Qubit Single Photon System, NTT, vol. 6, no. 1, 2008.
[67] Roffe, J. et al., Quantum Science and Technology vol. 3, no. 035010, 2018.
[68] Qiu, Y. et al., Four-junction superconducting circuit, Sci. Rep. vol. **6**, 28622, 2016.
[69] Xiang, Z. L. et al., Hybrid quantum circuits: Superconducting circuits interacting with other quantum systems, 2013.
[70] Childress, L., & Hanson, R. Diamond NV centers for quantum computing and quantum networks. MRS Bulletin, vol. 38 no. 2, 2013, pp.134-138.
[71] Fronik, T. W. J., Homogeneous broadening of the zero-phonon line in the nitrogen-vacancy centre in diamond for all strain regimes, PhD Thesis. Delft University of Technology, 2018.
[72] T. van der Sar., Quantum control of single spins and single photons in diamond, Ph.D. thesis, Delft, The Netherlands, 2012.
[73] Greentree, A. D. et al., Diamond integrated quantum photonic, Materials Today, vol. 11, no.9, 2008.
[74] Maze, J. R. et al., Properties of nitrogen-vacancy centers in diamond: the group theoretic approach, New Journal of Physics vol. 13, 2011.
[75] Clevenson, H., Englund, D., Broadband magnetometry and temperature sensing with a light-trapping diamond waveguide, Nature Physics, vol. 11, no. 5, 2015, pp. 393–397.

[76] Qiu, Y. *et al.*, Coupling spin ensembles via superconducting flux qubits, Phys. Rev. A, vol. 89, no. 042321, 2014.
[77] Souza, A. M. et al., High-fidelity gate operations for quantum computing beyond dephasing time limits. Phys. Rev. A, vol. 92, no. 062332,2015.
[78] Shukla, A. et al., Complete characterization of the directly implementable quantum gates used in the IBM quantum processors, 2018.
[79] G. Balasubramanian et al., Nature (London) 455, 648 ,(2008)
[80] Steffen, M. et al., Quantum computing: An IBM perspective, IEEE/CSC & ESAS, vol. 19, 2012.
[81] Diego García-Martín, Germán Sierra., Five Experimental Tests on the 5-Qubit IBM Quantum Computer, Journal of Applied Mathematics and Physics, vol. 6, 2018, pp. 1460-1475.
[82] Souza, M. A. et al., Robust dynamic decoupling. Philosophical Transactions of The Royal Society A Mathematical Physical and Engineering Sciences, vol. 12, no. 1976, 2012.
[83] Zhukov, A. A. et al., Modelling dynamics of entangled physical systems with superconducting quantum computer, 2017.
[84] Matsuzaki, Y. et al., Improving the lifetime of the nitrogen-vacancy-center ensemble coupled with a superconducting flux qubit by applying magnetic fields, Physical Review A, vol. 91, no. 042329, 2015.
[85] Bar-Gill, N. et al. Solid-state electronic spin coherence time approaching one second. Nat. Commun. 4:1743, 2013.
[86] Gang-Qin Liu and Xin-Yu, Quantum information processing with nitrogen–vacancy centers in diamond, Chinese Phys. B (27) 020304, 2018.
[87] Chao Lei et al, Decoherence Control of Nitrogen-Vacancy Centers, Scientific Reports, vol 7, 11937, 2017.